Title
Inhibition of the Oncogenic KDM4 Family of Histone Lysine Demethylases

Author
Younger, Noah Spector

Publication Date
2015

Peer reviewed|Thesis/dissertation

Inhibition of the Oncogenic KDM4 Family of Histone Lysine Demethylases

by

Noah Younger

DISSERTATION

Submitted in partial satisfaction of the requirements for the degree of

DOCTOR OF PHILOSOPHY

in

Chemistry and Chemical Biology

in the

GRADUATE DIVISION

of the

UNIVERSITY OF CALIFORNIA, SAN FRANCISCO

Acknowledgments

I would like to acknowledge the many people who have helped and encouraged me throughout my graduate studies, including my labmates, friends, colleagues and classmates. I would also like to acknowledge the help and support of my advisor, Danica Fujimori, as well as my thesis committee, Kevin Shannon, Jack Taunton, and Kevan Shokat. Most especially, I would like to acknowledge the lifelong love and support of my family, Jon Younger, Kim Spector and David Younger, without whom none of my accomplishments would be possible.

Portions of this thesis are derived from collaborative work, with contributions from Magdalena Korczynska, Daniel Le, Elisabet Gregori-Puigjané, Eriko Akutsu, Benjamin Spangler, Samuel Pollock, Idelisse Torres, Brian Shoichet and Danica Fujimori of UCSF, as well as Anthony Tumber, Tobias Krojer, Radosław Nowak, and Udo Oppermann of the University of Oxford. Chapter 2 is derived from a manuscript in preparation: Korczynska M, Le D, Younger N, Gregori-Puigjané E, Tumber A, Krojer T, Akutsu E, Pollock S, Torres I, Nowak R, Oppermann U, Shoichet B and Fujimori D. (2015). *Docking and Linking Fragments to Discover Histone Demethylase Inhibitors*.

Abstract

The human body is made up of over 35 trillion cells,[1] each of which contains an identical copy or two copies of DNA. These cells, however, diverge functionally and morphologically from one another as they occupy specialized niches in various tissues and organs. For example, some cells produce antibodies to ward off invading microbes as part of the immune system, others contract in response to electrical stimuli as part of the cardiac ventricular walls, and yet others pump ions against a concentration gradient as part of the renal tubules. Such diversity in organization and function arising from a common genome requires differential regulation of gene expression in different cell types. This is achieved through epigenetic control of chromatin, which consists of chemical modifications that do not change the DNA code itself.

Each modification must be carefully placed at the right times and at the right locations in the genome in order to achieve a proper transcriptional outcome. Sets of proteins that enzymatically 'write' and 'erase' epigenetic modifications are tightly regulated to ensure the proper temporal and spatial distribution of each mark. When this system is perturbed, often by mutation in reader or writer proteins or by modulation of their expression, diseases such as cancer may occur.

We are particularly interested in a set of enzymes, the KDM4 family, which removes transcriptionally repressive methylation of histone H3 lysine 9. This family of demethylases is known to promote oncogenesis, likely through inappropriate activation of oncogenic transcription in the setting of KDM4 amplification and overexpression. In order to study the mechanism by which this family promotes oncogenesis and also to validate it as a therapeutic target in cancer we have developed a novel series of

demethylase inhibitors using a combination of computational docking, synthetic chemistry, *in vitro* biochemistry and structural biology. These inhibitors display favorable potency and selectivity towards a subset of histone lysine demethylases, and we believe they will serve as the starting point for the development of chemical probes of the KDM4 family.

Table of Contents

List of Tables and Schemes

Chapter 1:

Chapter 2:

Chapter 3:

Chapter 4:

List of Figures

Chapter 1:

Chapter 2:

Chapter 3:

Chapter 4:

Chapter 1: Introduction

I. Histone Post-Translational Modification

Although there are different types of epigenetic mechanisms that affect regulation of gene expression, an especially important although incompletely understood one is the chemical modification of histone proteins. The four core histone proteins, H2A, H2B, H3 and H4 are the building blocks of nucleosomes, the basic organizational unit of chromatin. A nucleosome consists of two copies each of the four core histone proteins which associate through interactions of their globular C-terminal domains to form a scaffold around which is wrapped 147 base pairs of DNA. [2] The disordered N-terminal tails of each histone extend out from the nucleosome and are subject to numerous post-translational modifications. These modifications include, but are not limited to, methylation of lysine and arginine, phosphorylation of threonine and serine, and acetylation of lysine. [3] Histone PTMs profoundly affect local transcriptional activity as well as other DNA-dependent processes. For example, methylation of H3K4, H3K36 and H3K79 is typically associated with transcriptionally active genes, while methylation of H3K9, H3K27, and H4K20 is typically associated with transcriptionally repressed genes. [4] Mechanistically, histone PTMs are thought to function by way of two general paradigms.

In the first, modifications to certain histone tail residues can alter nucleosome-nucleosome interactions that contribute to higher-order chromatin compaction. Simply by being more crowded and sterically hindered, compact chromatin is less accessible to various transcription factors, polymerases, and any other proteins that require association with DNA to function. Although still somewhat controversial as to whether or not such a structure exists in cells, polynucleosomes *in vitro* will spontaneously form the so-called

'30-nm fiber,' named because of its approximate diameter, which appears by cryo-EM to be a highly regular double-helix of associated nucleosomes.[5] This compaction of nucleosomes is antagonized by certain post-translational modifications.

Perhaps the best example of a post-translational modification altering higher-order chromatin organization is acetylation of lysine 16 on histone H4 (H4K16). Normally, in the unmodified state, the positively charged ε-amino group of H4K16 binds to a composite acidic patch formed at the boundary of associated H2A and H2B on an adjacent nucleosome. This interaction is disrupted by acetylation of H4K16, which neutralizes the charge of the ε-amino group, and the 30-nm fiber no longer forms when H4K16 is acetylated *in vitro*.[6] H4K16 acetylation is associated with increased transcription,[7] suggesting that modulation of nucleosome compaction plays a role in transcriptional regulation. Numerous other lysine residues on the various histone tails are also subject to acetylation, and neutralization of the positively charged lysine residues tends to weaken the interaction between nucleosomes and the associated negatively charged DNA, although whether or not specific interactions are involved as has been described for H4K16 and its binding site is unclear. However, in general, higher degrees of acetylation correlate with increased transcriptional activity, as would be expected for a class of modifications that antagonizes nucleosome compaction.

In the second paradigm by which post-translational modifications of histone tails affect transcription and other DNA-dependent processes, certain modifications or sets of modifications serve as recognition motifs for specialized binding domains found in effector proteins or protein complexes. Binding of a recognition domain to its cognate mark or marks may affect protein function by recruitment of the effector to a specific

location in the genome, by orientation or stabilization of an effector once recruited, or by allosteric modulation of effector function. This paradigm presumes the existence of domains that are able to specifically recognize histone modifications. Many such domains have been described, with often exquisite specificity for a single type of modification at a single residue. For example, the chromodomain of Eaf3 binds to methylated H3K36 and recruits the RpdS3 histone deacetylase complex to the bodies of actively transcribed genes to suppress cryptic transcription.[8] In another example, the PHD1 domain of the H3K4 demethylase KDM5A binds to unmethylated H3K4 to promote allosteric activation of demethylase activity on nearby methylated marks.[9] The effector proteins of many histone PTMs are unknown, and finding these associations is an active area of research. Furthermore, many protein complexes or even single proteins contain multiple putative histone PTM binding domains, implying that histone PTMs may combinatorially specify unique transcriptional outcomes. This potential for cross-talk and interaction between histone modifications forms the theoretical basis for the idea of a 'histone code,' in which the complete set of modifications found at a given genetic locus are postulated to be read and interpreted through the recruitment of a specific set of interacting proteins and complexes.[10]

II. Histone H3 Lysine 9 Methylation

As discussed above, histone post-translational modifications such as lysine methylation are able to modulate gene expression by recruiting specific effector proteins or complexes. One example of particular interest is transcriptional repression and heterochromatin formation associated with histone H3 lysine 9 (H3K9) methylation.

H3K9me3 is the defining epigenetic mark of heterochromatin, and serves primarily to stabilize the H3K9me2/3 binding proteins Heterochromatin Protein 1 α and β (HP1α and HP1β) at repressed heterochromatic regions and at repressed euchromatic promoters. [11,12] HP1, once recruited to target loci through mechanisms that aren't well understood, is able to oligomerize and span multiple methylated nucleosomes. [13] At the nucleosome, HP1 is thought to both physically compact and stabilize a heterochromatic state, preventing access by transcriptional machinery, and also to recruit other factors that result in gene silencing such as histone deacetylases and DNA methyltransferases. [14]

H3K9 methylation has been thought for quite some time to be required for heterochromatin maintenance/spreading, ever since early screens for suppressors of positional effect variegation in *D. melanogaster* identified the H3K9 methyltransferase Su(var)3-9. Catalytic activity of its mammalian homolog, SUV39h, is required for correct localization of HP1 (and SUV39h itself) to heterochromatic foci, [15] confirming that H3K9 methylation plays a causative role in establishing heterochromatin, and that enzymes responsible for regulating H3K9 methylation, such as methyltransferases and demethylases, may indirectly regulate gene expression through HP1-mediated gene silencing. A similar model, in which localization/stabilization of HP1 is mediated by

H3K9 methylation, seems to operate at the promoters of repressed genes in euchromatic regions.[12]

There are many mammalian H3K9 methyltransferases and demethylases, whose opposing roles in placing and removing the H3K9 methyl mark, respectively, ensure the proper and dynamic localization of this mark across the genome. It is likely that specialization and differential regulation of the methyltransferases and demethylases are responsible, at least in part, for proper temporal and spatial control of H3K9 methylation. In support of this hypothesis, H3K9 methyltransferases are known to be specialized for placing this mark in different contexts: the H3K9 methyltransferases G9a and GLP are primarily responsible for methylation at euchromatic gene promoters, [16] while SUV39h1 and SUV39h2 are primarily responsible for methylation in heterochromatic regions.

Figure 1: Phylogenetic Tree of JmjC Domain Containing Proteins

Phylogenetic diagram based on sequence alignment of the catalytic domains of selected JmjC proteins, colored by subfamily. Major substrate specificities are as follows: Red = H3K9/36; Green = H3K4; Light Blue = H3K27; Pink = H3K9; Orange = H3K36; Purple = H3K9; Dark Blue = hydroxylases

There are two families of mammalian histone demethylases: the flavin dependent demethylases and the JmjC domain-containing Fe^{II} and αKG dependent demethylases. The flavin dependent demethylases consist of two closely related enzymes, KDM1A and KDM1B, which catalyze the removal of di- and mono-methyl marks from H3K4 and H3K9 residues. The JmjC domain-containing demethylase family, because of its unique catalytic mechanism, is able to remove tri-methyl marks. It is also much larger than the flavin dependent demethylase family, consisting of 24 enzymes, although not all have demonstrated catalytic activity. These enzymes have distinct and overlapping substrate specificity for methylated histone lysine substrate residues, and also appear to be in some cases differentially expressed, found as part of different protein complexes, and involved in different biological and pathological processes.

The JmjC domain containing proteins can be organized into 7 subfamilies based on sequence similarity and substrate specificity (**Figure 1**). The KDM2 subfamily has specificity for H3K36me2/me1, and KDM2B can additionally demethylate H3K4me3. The KDM3 subfamily has specificity for H3K9me2/me1. The KDM4 subfamily has specificity for H3K9me3/me2, and KDM4A, B and C can additionally demethylate H3K36me3/me2. The KDM5 subfamily has specificity for H3K4me3/me2/me1. The KDM6 subfamily has specificity for H3K27me3/me2. The KDM7 subfamily has specificity for H3K9me2, but various other methylation states and substrates have also been identified. The hydroxylase subfamily includes a diverse array of JmjC proteins, many of which are able to demethylate histones and alternatively or additionally are able to hydroxylate one or more often non-histone substrates using an analogous mechanism. A full discussion of all JmjC domain containing proteins is beyond the scope of this

work, and the remaining discussion will focus on the KDM4 subfamily of JmjC domain containing demethylases.

Figure 2: KDM4 Family of Histone Lysine Demethylases

(A) Schematic representation of KDM4 demethylase domain architecture. JmjN and JmjC domains are required for catalysis. (B) Demethylation reaction catalyzed by KDM4 enzymes.

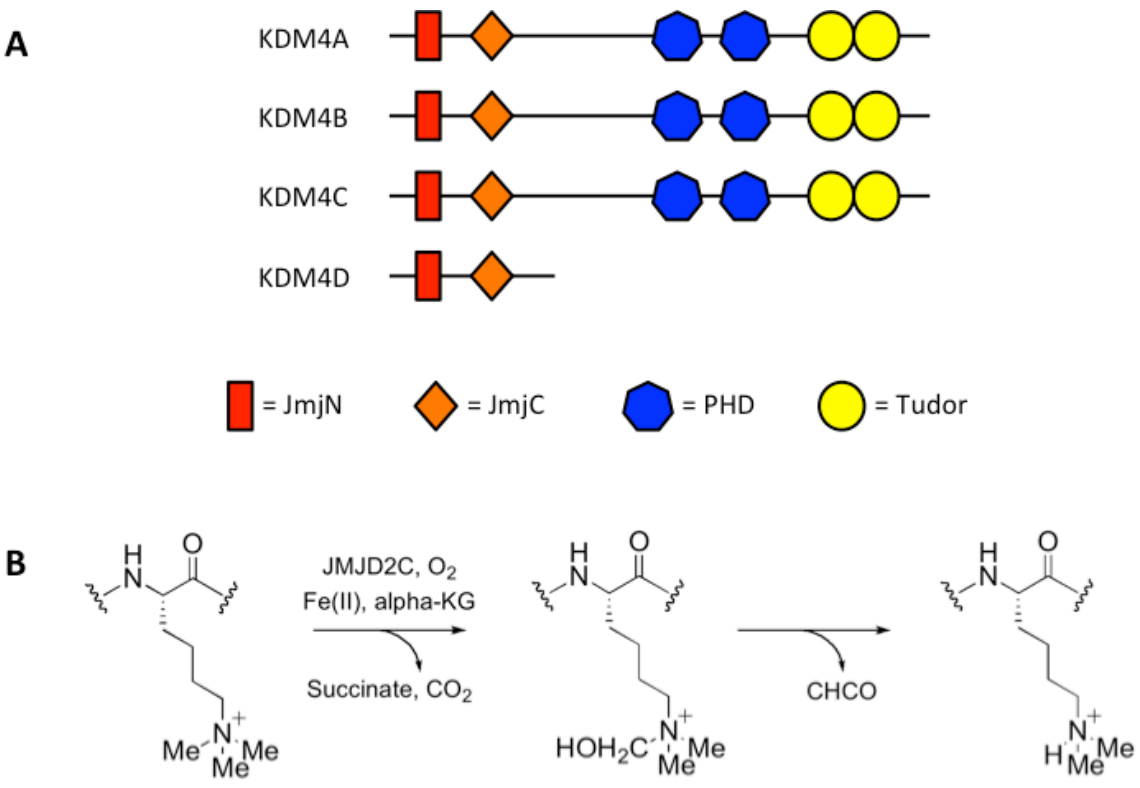

III. Biology of KDM4 Histone Lysine Demethylases

The KDM4 subfamily of JmjC domain-containing lysine demethylases consists of six members, A-F. Of these, KDM4F is thought to be a pseudogene, and expression of KDM4E is highly restricted, mostly to the testis. Biological roles have been explored only for KDMA-D, and the focus of this chapter will be on these four enzymes. Each contains N-terminal JmjN and JmjC domains, both of which are required for catalysis, and, with the exception of KDM4D, C-terminal PHD domains and double tudor domains which are thought to be important for recruitment of the demethylases to target loci through specific interactions with DNA or histone PTMs (**Figure 2A**). The removal of a methyl group from the ε-amine of tri- and di-methyllysine is accomplished by oxidation of the methyl group by molecular oxygen to form an unstable hemiaminal, which spontaneously decomposes with elimination of formaldehyde (**Figure 2B**). Catalysis requires an α-ketoglutarate (αKG) cosubstrate and an Fe^{II}. Thus far, four histone substrates have been identified for the KDM4 subfamily: trimethylated lysine 9 of histone H3 (H3K9me3), and, less efficiently, dimethylated H3K9 (H3K9me2) and trimethylated/dimethylated lysine 36 of histone H3 (H3K36me3/me2).[17] In addition, KDM4C demethylates Pc2, and this function is critical for activation of E2F1 target genes.[18]

Figure 3: Crystal Structure of Substrate-Bound KDM4A

Residues making important contacts with NOG, a cosubstrate analog (blue), and with metal ion (green), are shown in white. Substrate methylated H3K9 peptide backbone and methylated lysine residue are also shown (yellow). From PDB ID 2Q8C.

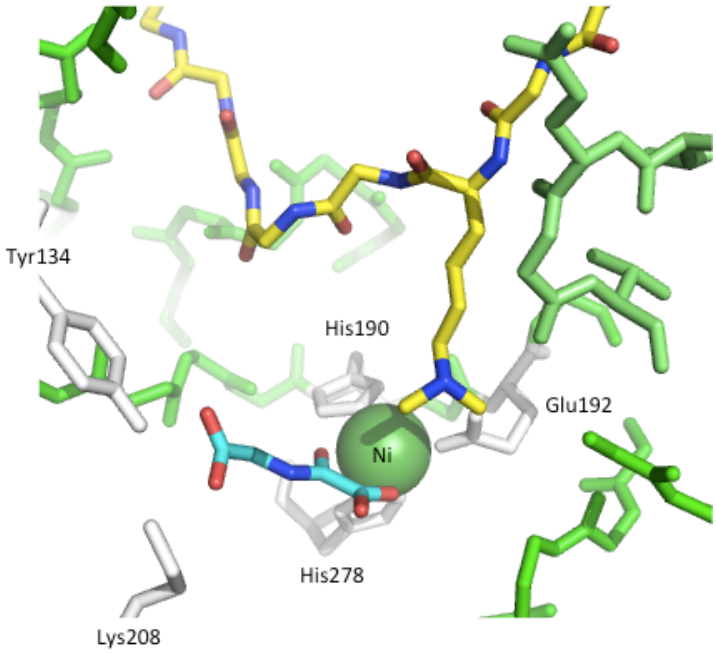

Crystal structures of the catalytic domains of the KDM4 subfamily members reveal a high degree of structural similarity, especially in the region interacting with methyllysine, Fe^{II}, and αKG. Fe^{II} is bound in the active site by two histidine residues and an aspartic/glutamic acid, and is further chelated by the α-ketone and adjacent carboxylic acid of αKG. Three conserved hydrogen bonds with asparagine, tyrosine and lysine side-chains further stabilize bound αKG (**Figure 3**). The trimethylammonium group of substrate peptide is bound in a pocket with slight, functionally insignificant variations among the orthologs. [19] The peptide substrate binding region of the active site is highly conserved between KDM4A-C, which are able to demethylate both H3K9 and H3K36, but differs at several positions with respect to KDM4D, which is able to demethylate H3K9 only. Interestingly, the peptide substrates seem to be held in the active site by interactions with only five residues besides those involved in methylammonium binding. It appears that the ability of the peptide substrate to adopt a highly bent conformation is required for binding to the KDM4 enzymes and may contribute to binding specificity.[20]

Although only recently discovered, early work has revealed numerous roles for the KDM4 subfamily members in normal biology and in disease. Several important properties of KDM4 function are beginning to be understood and explored. First, it seems clear that the KDM4 subfamily members have both distinct and overlapping functions, particularly in tissue-specific differentiation, DNA repair, and hormone-mediated gene expression. It is also becoming apparent that KDM4 subfamily members often function as members of protein complexes, and that they have important scaffolding as well as catalytic roles. Specialization within the KDM4 subfamily, when applicable, is

accomplished both through regulation of KDM4 expression and by differential inclusion in protein complexes. Specific examples will be discussed below.

KDM4A, B, and D appear to all be involved in the response to DNA damage, although in distinct and even opposing ways. While KDM4B and D are both recruited to sites of DNA damage in a PPARγ dependent manner and promote tolerance to DNA damage, recruitment of KDM4B requires demethylase activity while recruitment of KDM4D does not.[21,22] KDM4A, on the other hand, appears to be ubiquitinated and degraded in response to DNA damage and overexpression sensitizes cells to DNA damaging agents.[23] Intriguingly, KDM4D promotes 53BP1 foci formation at the sites of DNA damage, while KDM4A antagonizes 53BP1 foci formation. As 53BP1 and KDM4A have Tudor domains that recognize methylated H3K4 while KDM4D does not, it is possible that the ability to compete for binding methylated H3K4 accounts for the opposing effects of KDM4A/D on 53BP1 recruitment.

It is becoming clear that the KDM4 demethylases play important roles in development. One large study identified several demethylases that play a role in maintaining pluripotency, including KDM4B and KDM4C. These demethylases were found to be present individually or together at the promoter regions of many genes in mouse embryonic stem cells, where KDM4B interacts directly with Myc as well as the 'core module' which includes Oct4 and Nanog and participates in the regulation of genes controlled by these factors, while KDM4C interacts with the PRC2 complex and participates in regulation of PRC2 controlled genes.[24] The two demethylases seem to only exert transcriptional effects at genes where they are found as part of their respective complexes, and not at genes where they are found alone. This result provides an enticing

explanation as to how the highly conserved KDM4 subfamily members may depend on differential inclusion in protein complexes to regulate their varying and sometimes even opposing effects in different contexts. It is important to note also that the individual roles of KDM4 subfamily members in maintenance of pluripotency remains controversial. While another study also demonstrated a role for KDM4C in maintaining pluripotency, [25] a third study has challenged both findings, showing that KDM4C knockout mice develop normally, and that KDM4C knockout does not effect maintenance of ESC pluripotency. [26] A possible explanation for this discrepancy is that KDM4C was found to maintain pluripotency based on gene knockdown experiments, which are subject to undesired off-target effects, while the opposite result was obtained using a knockout cell line.

Although KDM4 subfamily members may sometimes be differentially regulated as in the case just described, it also seems that in some contexts they may perform overlapping/redundant functions. One example is the role of KDM4s in neuronal cell fate determination, where KDM4A and KDM4C promote differentiation of neural stem cells by upregulating *BDNF* expression, a key factor involved in neuronal lineage specification. They do this by demethylating H3K9 at the promoter and recruiting PolII. At the same time, KDM4A/C inhibit *GFAP* expression, a marker of the astrocyte lineage, and are associated with decreased H3K36 methylation in the *GFAP* gene body and decreased PolII recruitment. Opposing regulation of these two cell fate determination genes promotes the differentiation of neural stem cells into neurons rather than astrocytes. [27] Although not explored in this study, it will be interesting to investigate how context-dependent specificity for different substrate marks is achieved.

This example represents, to my knowledge, the only known case of KDM4 mediated regulation of gene expression by demethylation of H3K36 in cells, and suggests that demethylation of this mark may play a general role in KDM4 mediated gene repression. In general, extensive transcriptional repression is identified alongside gene activation in genome-wide studies of KDM4 transcriptional regulation, although with the exception of *GFAP*, no downregulated genes have been shown to be direct targets of the KDM4 demethylases.

Further studies suggest additional roles for the KDM4 subfamily members in regulating differentiation. In one example, KDM4A is specifically required for neural crest differentiation. It binds to the promoters of neural crest specifier genes during differentiation, removes the H3K9me3 mark, and is required for correct expression patterns of these genes. [28] In another example, KDM4B is shown to be important for fate determination in mesenchymal stem cells, in which it promotes osteogenesis rather than the alternative fate of adipogenesis. This is at least in part due to control of the expression of *DLX5*, a transcription factor that is important for promoting osteogenesis, through demethylation of H3K9me3 at its promoter and promotion of PolII recruitment. [29]

One of the most well established roles of the KDM4 demethylases is as co-activators of steroid hormone receptors such as the androgen receptor (AR) and the estrogen receptor (ER). Multiple reports have implicated KDM4A and/or B as cofactors of the ER. They have both been found to be physically associated with the ER, to be recruited to ER target genes, and to mediate demethylation of H3K9me3 once recruited. [30-32] KDM4B has further been shown to be required for normal mammary development. [31] Interestingly, both KDM4A and B are found in a complex with both ER and with the

H3K4 methyltransferase MLL2, and ER dependent transcription of ER target genes seems to depend on coordinated removal of repressive H3K9 methylation followed by deposition of activating H3K4 methylation. [30] KDM4B is transcriptionally regulated by ER, [33] and ER is transcriptionally regulated by KDM4B, [34] suggesting the presence of a feed-forward mechanism for KDM4B mediated ER coactivation.

All four KDM4 subfamily members are coactivators of AR. Each physically associate with AR, and all are important for androgen-induced AR target gene expression. [35-37] In the case of KDM4C, activation of a model AR target gene was found to depend on recruitment of a catalytically active demethylase, and is associated with reduced H3K9me3 at the target gene promoter. [36] Interestingly, catalytically dead mutants of KDM4C and D had reduced but not completely abrogated abilities to coactivate AR dependent transcription, suggesting that these demethylases serve both catalytic and scaffolding/recruitment roles in AR dependent transcription. [35,36] Furthermore, KDM4B is able to stabilize AR by preventing its ubiquitination and degradation independently of its catalytic activity. [37]

KDM4A is the most-studied member of the KDM4 subfamily, and besides its roles as a coactivator of steroid mediated transcription and in the regulation of differentiation, it is important for other diverse biological processes. One example is cardiac remodeling in response to increased afterload, where KDM4A promotes hypertrophy. In the setting of increased afterload, KDM4A was found to bind to the promoter of the biomechanical stress sensor gene *FHL1*, and promotes demethylation of H3K9me3 and increased gene expression. [38]

Besides its canonical role in activating transcription by demethylation of repressive H3K9me3, it seems that KDM4A is able to repress transcription in certain contexts. For example, it is required for specific repression of the trophoblast lineage gene ASCL2 in non-trophoblast embryonic cells, and that this repressive function requires association with the corepressor N-CoR and is Tudor domain, but not catalytic domain, dependent. [39] As the Tudor domain of KDM4A specifically recognizes methylated H3K4 and H4K20, [40] this result suggests that KDM4A might be targeting the N-CoR complex to these marks. A fascinating line of investigation has implicated KDM4A in regulation of DNA replication, showing that KDM4A promotes replication by antagonizing HP1γ localization, [41] and when overexpressed can cause re-replication of specific regions of DNA, [42] presumably by making these regions excessively open and accessible to replication machinery. These studies highlight the careful balance that is necessary to maintain correct levels of histone methylation, and the consequences of tipping too far in one direction. Finally, recent work has shown that KDM4A plays an unexpected role in promoting protein translation initiation in a catalytic activity dependent manner. [43] The details of how KDM4A functions in protein synthesis remain to be explored.

IV: KDM4 Histone Lysine Demethylases in Oncogenesis

The KDM4 subfamily members A-D have each been shown to promote oncogenesis in several contexts, and these findings have been extensively reviewed. [44-47] Notably, analysis of gene expression data suggests that high levels of KDM4 protein expression promotes oncogenesis in human tumors, especially in prostate cancer. For example, KDM4A-C are overexpressed in prostate cancer samples relative to normal prostate tissue, [47,48] and higher levels of KDM4C are associated with increased metastasis and higher grade tumors. Although not generally found to be overexpressed in prostate cancer, higher levels of KDM4D are associated with increased metastasis, higher grade tumors, as well as shorter progression-free survival. [47] Besides prostate cancer, KDM4B is overexpressed in colon cancer, where its overexpression is associated with increased invasion and lymph node metastasis, [49] and in a subset of breast cancers marked by increased hypoxia, where its overexpression is associated with shorter overall survival. [33] Other examples of KDM4 overexpression in cancer include KDM4C amplification and overexpression in lung cancer, [50] esophageal squamous carcinoma, [51] and lymphomas, [52] KDM4A overexpression in breast cancer, [44] and lung cancer, [23] and KDM4B overexpression in breast, colon, gastric, lung, and skin cancer.[44]

Similar to the observations in patient-derived biopsies described above, overexpression of KDM4 demethylases *in vitro* has been shown to promote cancer cell proliferation and metastasis. For example, overexpression of KDM4C in breast epithelial cells caused an increased rate of proliferation, growth-factor independent proliferation, anchorage-independent growth, and formation of mammospheres *in vitro*. [53] Overexpression of wild-type KDM4A, but not a catalytically dead mutant, caused

increased tumor development in a mouse model of mutant Ras driven cancer. [23] Knockdown of KDM4B in gastric cancer cells impairs clonogenesis, and reduces growth of xenografts in mice. [54] And mouse breast cancer xenografts showed reduced growth and metastasis to the lungs upon knockdown of KDM4C. [55]

Evidence suggests that KDM4 subfamily members promote oncogenesis at least in part by removing H3K9 methyl marks at one or more oncogenic loci, which antagonizes Heterochromatin Protein 1 (HP1) mediated transcriptional silencing, thereby promoting oncogenic transcription. [56] In several cases this increase in H3K9 methylation at target loci has been demonstrated directly. In primary mediastinal B-cell lymphoma and Hodgkin lymphoma cells, KDM4C is amplified and overexpressed, and knockdown of KDM4C results in increased global H3K9me3, as well as an increased number and intensity of HP1 α foci. Knockdown of KDM4C also results in increased promoter H3K9 methylation at the *MYC* locus, and a concomitant decrease in *MYC* expression. [52] In LNCaP prostate cancer cells, KDM4C coactivates androgen receptor mediated transcription at the *KLK2* and *PSA* loci by removing H3K9 methyl marks, and is critical for androgen-induced proliferation. [36] In MCF7 breast cancer cells, KDM4B coactivates HIF-1 α mediated transcription under hypoxic conditions by demethylating H3K9 at several target genes, which are downregulated upon KDM4B knockdown. [57] While this model provides a rationale for KDM4-mediated transcriptional activation of oncogenes, there is evidence that in some contexts, KDM4 proteins may negatively regulate tumor-suppressor transcription. For example, KDM4A antagonizes the p53 pathway by repressing the expression of *CHD5,* a gene required for oncogene-induced senescence. [23]

V: Inhibition of KDM4 Histone Lysine Demethylases

Since it has become clear that at least several of the JmjC domain-containing demethylases play a role in promoting oncogenesis there have been significant efforts to develop potent and selective small molecule inhibitors of various JmjC demethylase sub-families. As there are currently no inhibitors that are selective for the KDM4 subfamily, the following discussion will encompass inhibitors of all JmjC demethylases.

Most efforts to target the JmjC demethylases have focused on the substrate binding pocket, which normally binds an iron cofactor as well as an αKG cosubstrate and peptide substrate. Apparent affinities for peptide substrate and αKG cosubstrate have been characterized for several KDM4 subfamily members, and are in the low-mid micromolar range *in vitro*.[58] High-resolution crystal structures are available for several proteins representing diverse sub-families within the JmjC family. In particular, several members of the KDM4 subfamily have been crystalized both apo- and bound to H3K9me3 and (when applicable) H3K36me peptides, as well as with αKG analogs and several classes of inhibitors. Altogether the JmjC family seems to represent an ideal target for drug discovery, with interesting and unexplored biology, a strong link to oncogenesis, well-behaved *in vitro* activity, a druggable active site, and extensive structural support for rational drug discovery.

However, two main challenges have frustrated significant progress in this field. The first is a high degree of homology in the active sites across all αKG and iron dependent oxygenases. Therefore, although it is possible to achieve relatively potent inhibition of the JmjC family with αKG cosubstrate mimics or closely related compounds, it is difficult to achieve selective inhibition of a single JmjC enzyme or even

a JmjC subfamily in this way. A possible solution to this problem is to target the less conserved peptide binding region of the substrate binding pocket, either by elaboration of an αKG mimic or by identifying new scaffolds that bind in this region. Another is to find entirely new druggable pockets. Both possibilities are beginning to be explored and will be discussed below.

The second significant challenge is that the αKG binding interactions in particular are highly hydrophilic. This is not surprising, as αKG contains two carboxylic acid moieties. Unfortunately, in order to exploit critical interactions mediated by these highly polar functional groups, any αKG analog used as an inhibitor seemingly must incorporate analogous hydrophilic/charged chemical groups. This requirement for significant hydrophilicity impacts the cell permeability and therefore cell activity of most if not all small molecule inhibitors of the JmjC family described to date. Possible solutions include using a pro-drug strategy to mask any charged chemical groups, as well as attempting to replace any charged chemical groups with isosteres. Another possible solution, as for the problem discussed above, is to target a different part of the substrate binding pocket or a different pocket entirely. These possibilities are also beginning to be explored and will be discussed further.

Table 1: JmjC Demethylase Inhibitors

A table of selected published and patented inhibitors, including relevant potency, selectivity, and cell activity data.

	Structure	JMJDs	IC_{50}, μM	Assay	Other Enzymes	IC_{50}, μM	Assay	Cell Assay	EC_{50}, μM	CC_{50}, μM	References
1	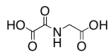				C-P4H (Ki)	0.5	$^{14}CO_2$ release				Hirsila M et. al. *JBC* **2003**, *278*, 30772.
					PHD1	50	$^{14}CO_2$ release				
					PHD2	8	$^{14}CO_2$ release				
					FIH (Ki)	2	$^{14}CO_2$ release				Koivunen P et. al. *JBC* **2004**, *279*, 9899.
		KDM4E	24	FDH coupled							Rose N et. al. *J Med Chem* **2010**, *53*, 1810.
		KDM4A	17	FDH coupled	AlkB	2.7	FDH coupled				Hopkinson R et. al. *Chem Sci* **2013**, *4*, 3110.
		KDM4C	14	FDH coupled	FIH	20.5	MALDI				
		KDM3A	2	AlphaScreen							
		KDM6B	0.3	AlphaScreen							
		KDM2A	45	AlphaScreen							
		KDM4C	500	FDH coupled	PHD1	2.1	DELFIA				Hamada S et. al. *J Med Chem* **2010**, *53*, 5629.
		KDM4A	250	FDH coupled	PHD2	5.6	DELFIA				
2	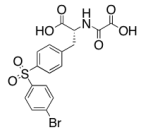	KDM4E	5.4	FDH coupled	PHD2	NI	MALDI				Rose N et. al. *J Med Chem* **2010**, *53*, 1810.
		KDM4E	21	MALDI	FIH	60.2	MALDI				
		KDM4A	12	MALDI							
3		KDM4C	9.4	FDH coupled	PHD1	1.5	DELFIA	Using methyl ester with KDM1A inhibitor in LNCaP		~30	Hamada S et. al. *J Med Chem* **2010**, *53*, 5629.
		KDM4A	4.2	FDH coupled	PHD2	6.1	DELFIA				
		KDM4C (Ki)	13	FDH coupled							Leurs U et al. *Bioorg Med Chem Lett* **2012**, *22*, 5811.
		KDM4E	1.8	FDH coupled							Rose N et. al. *J Med Chem* **2008**, *51*, 7053.
								Using methyl ester in 293T cells transfected with KDM4: 4 fold		3900	Mackeen M et. al. *J Proteome Res* **2010**, *9*, 4082.
		KDM4E	0.44	FDH coupled							Thalhammer A et. al. *Org Biomol Chem* **2011**, *9*, 127.
		KDM6B	33	AlphaScreen	AlkB	1.4	FDH coupled				Hopkinson R et. al. *Chem Sci* **2013**, *4*, 3110.
		KDM2A	4.1	AlphaScreen	FIH	1.1	FDH coupled				
		KDM5C	0.45	AlphaScreen							
4		KDM4E	0.11	FDH coupled	PHD2	23% activity	TR-FRET				Thalhammer A et. al. *Org Biomol Chem* **2011**, *9*, 127.
5	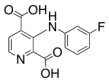	KDM4E	2.5	FDH coupled	PHD2	>400	TR-FRET				Thalhammer A et. al. *Org Biomol Chem* **2011**, *9*, 127.

	Structure	JMJDs	IC_{50}, μM	Assay	Other Enzymes	IC_{50}, μM	Assay	Cell Assay	EC_{50}, μM	CC_{50}, μM	References
6		KDM2A	15	AlphaScreen				HeLa (H3K4me2)	~100	~75	Rotili D et. al. *J Med Chem* **2014**, *57*, 42.
		KDM3A	0.17	AlphaScreen				HeLa (H3K9me3)	~100	~75	
		KDM4C	0.6	AlphaScreen				HeLa (H3K4me3)	~200	~75	
		KDM4E	0.3	AlphaScreen				HeLa (H3K9me2)	~100	~75	
		KDM5C	25	AlphaScreen				No cell cycle arrest in LNCaP and			
		KDM6B	0.14	AlphaScreen				HCT116 cells			
		KDM4E	2.4	MALDI	FIH	20.5	MALDI	HeLa (transfection)	87	292	King O et. al. *PLoS One* **2010**, *5*, e15535.
		KDM4A	1.7	MALDI	PHD2	14.3	MALDI				
		KDM6A	1.1	AlphaScreen	AlkB (Ki)	10.2	FDH coupled				Hopkinson R et. al. *Chem Sci* **2013**, *4*, 3110.
7		KDM4E	6	MALDI	FIH	19.6	MALDI				King O et. al. *PLoS One* **2010**, *5*, e15535.
		KDM4A	8.2	MALDI	PHD2	14.4	MALDI				
8	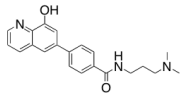	KDM4E	0.92	FDH coupled	KDM1A	>100	HRP coupled	Viral IE expression in HSV infected HFF cells	10		Rai G et al. *Probe Reports from the NIH Molecular Libraries Program* **2013**
9	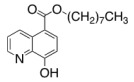	KDM4C	3.9	AlphaScreen	PHD2	>100	AlphaScreen	KDM4A (transfection)	3.8	>300	Schiller R et. al. *ChemMedChem* **2014**, *9,* 566.
		KDM4E	45	AlphaScreen				HIF stabilization (western)	<50		
		KDM2A	>100	AlphaScreen							
		KDM3A	>100	AlphaScreen							
		KDM5C	>100	AlphaScreen							
10	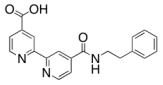	KDM4E	0.11	FDH coupled							Chang K et. al *ChemMedChem* **2011**, *6*, 759.
11	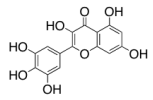	KDM4E	3.6	FDH Coupled							Sakurai M et. al. *Mol BioSyst* **2010**, *6,* 357.
		KDM4E	3.2	MALDI							
12	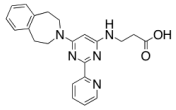	KDM6B	5	RapidFire MS				Using ethyl ester:			Kruidenier L et al. *Nature* **2012**, *488*, 404.
		KDM4A	>100	RapidFire MS				TNF-α production in macrophages	9		
		KDM4C	>100	RapidFire MS				H3K27me3 at TNFA TSS	<30		
		KDM4D	79	RapidFire MS							
		KDM4E	63	RapidFire MS							

	Structure	JMJDs	IC_{50}, μM	Assay	Other Enzymes	IC_{50}, μM	Assay	Cell Assay	EC_{50}, μM	CC_{50}, μM	References
13	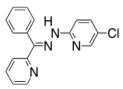	KDM5A	0.23	ELISA	TET1	>10	ELISA	H358 cell lysate H3K9me3	0.5		Wang L et. al. *Nat Comm* **2013**, *4*, 2035.
		KDM4A	0.445	ELISA	PHD2	>6	ELISA	demethylase activity			
		KDM4C	1.1	ELISA	KDM1A	>5	H_2O_2 coupled	Many cancer cell lines	0.01-1		
		KDM6B	0.855	ELISA							
14	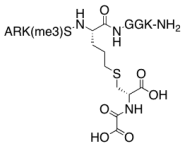	KDM3A	>100	AlphaScreen							Woon E et. al. *Angew Chem Int Ed Engl* **2012**, *13*, 1631.
		KDM4A	0.27	AlphaScreen							
		KDM4E	0.09	AlphaScreen							
		KDM6B	>100	AlphaScreen							
		KDM2A	>100	AlphaScreen							
		PHF8	1000	MALDI							
		PHD2	>500	MALDI							
		FIH	>1000	MALDI							
15	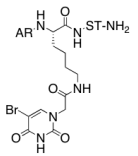	PHF8 (Ki)	NI	FDH coupled							Lohse B et. al. *Angew Chem Int Ed* **2011**, *50*, 9100.
		KDM4A (Ki)	118	FDH coupled							
		KDM4C (Ki)	27	FDH coupled							
16	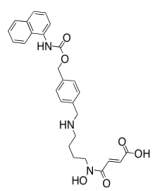	KDM4A	4.3	DELFIA	PHD1	54	$^{14}CO_2$ release	Using methyl ester:			Luo X et. al. *JACS* **2011**, *133*, 9451.
		KDM4C	3.4	DELFIA	PHD2	83	$^{14}CO_2$ release	KDM4C (transfection)		<10	
		KDM4E	5.9	AlphaScreen	PHD3	31	$^{14}CO_2$ release	HIF stabilization (western)	>15		
		PHF8	43	MALDI	FIH	22	$^{14}CO_2$ release	C2C12 myogenesis	~2		
		KDM6B	10	?	KDM1A	620	HRP Coupled	KYSE150 (H3K4me3)	10.3	5.1	
								KDYS150 (H3K9me3)	8.6	5.1	
								MCF7 (H3K4me3)	6.7		
								MCF7 (H3K9me3)	6.3		
17	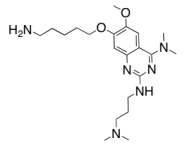	KDM7A	3.4	MALDI	GLP	75	?	MEF cells		46	Upadhyay A et. al. *J Mol Biol* **2012**, *416*, 319.
		PHF8	<10	?				HEF cells		52	
		KDM5C	>10	FDH coupled							

	Structure	JMJDs	IC_{50}, μM	Assay	Other Enzymes	IC_{50}, μM	Assay	Cell Assay	EC_{50}, μM	CC_{50}, μM	References
18	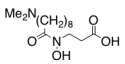	KDM4C	1	FDH coupled	PHD1	>100	DELFIA	Using methyl ester, cooperative cytotoxicity with LSD1 inhibitor in LNCaP, PC-3, HCT116			Hamada S et. al. *J Med Chem* **2010**, *53*, 5629.
		KDM4A	3	FDH coupled	PHD2	>100	DELFIA				
		KDM7B	19	MALDI							Suzuki T et. al. *J Med Chem* **2013**, *56*, 7222.
		KDM5A	13	FDH coupled							
19	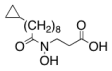	KDM4A	>120	FDH coupled				H3K27me2 (western) in KYSE150 cells	~20	16	Suzuki T et. al. *J Med Chem* **2013**, *56*, 7222.
		KDM4C	83	FDH coupled				HeLa		40	
		KDM5A	55	FDH coupled				H3K27me2 (western) in N2a cells	<100	86	
		KDM6A	>100	ELISA				Cell cycle arrest in HeLa and KYSE150			
		KDM7B	1.2	MALDI				Decreased E2F1 expression in HeLa			
		KDM2A	6.8	AlphaScreen							
		KDM7A	0.2	MALDI							
20	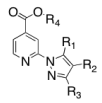	KDM5A	<0.1	TR-FRET				western blot for H3K4(me3) in ZR-75-1	<0.1		Zhe, N et. al. *US Patent* **2015**, 8987461.
		KDM5B	<0.1	TR-FRET							
		KDM4C	<0.1	TR-FRET							
		KDM4A	<0.1	TR-FRET							
		FBXL10	<0.1	AlphaScreen							
21	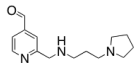	KDM4C	>2.5	AlphaScreen				western blot for H3K4me3 in U2OS cells	<0.25		Labelle M et. al. *US Patent* **2014**, 0371214
		KDM2B	>2.5	AlphaScreen							
		KDM5C	<0.25	AlphaScreen				KDM4C (transfection)	>2.5		
		KDM3A	>2.5	AlphaScreen				KDM4A (transfection)	>2.5		
		KDM3B	>2.5	AlphaScreen				KDM5B (transfection)	<0.25		
		KDM4A	>2.5	AlphaScreen				inhibition of MCF7 proliferation	<0.25		
		KDM4B	0.25-2.5	AlphaScreen							
		KDM6B	>2.5	AlphaScreen							
		PHF8	>2.5	AlphaScreen							
		KDM6A	>2.5	AlphaScreen							
		KDM5B	<0.25	AlphaScreen							

Initial efforts to identify JmjC demethylase inhibitors borrowed heavily from earlier efforts to target the αKG dependent prolyl hydroxylases involved in fibrotic diseases using αKG mimicking compounds. Three examples which exemplify this strategy are N-oxalylglycine (NOG) (**1**) (**Figure 4A**), 2,4-pyridinedicarboxylic acid (2,4 PDCA) (**3**), and 5-carboxy-2,2'-bipyridine (bipyridyl). All were identified originally as prolyl hydroxylase inhibitors, and subsequently found to broadly inhibit the αKG dependent oxygenases, including the JmjC demethylases. Although not active in cells by themselves, the dimethyl ester versions of NOG and 2,4 PDCA are. In all three cases, efforts have been made to elaborate these scaffolds to increase potency and selectivity for demethylases. In general, these efforts focused on extending these compounds towards the less conserved peptide substrate binding pocket, and were assisted by crystal structures showing the position of each scaffold most amenable to such derivatization.

In the case of NOG, a methane thiol was substituted for a hydrogen at the C-α position and this compound was used along with a thiol library in a dynamic combinatorial MS approach to identify resulting mixed disulfides with high affinity for the target (in this case, KDM4E). This experiment identified a benzyl derivative as the most potent of those tested. Further optimization and elaboration resulted in the derivative (**2**) (**Figure 4B**), which has an IC_{50} of 5.4 μM against KDM4E, a five-fold improvement over NOG. Importantly, no inhibition of the prolyl hydroxylase PHD2 was observed, in contrast with NOG which is an approximately equipotent inhibitor of the two enzymes. Compound (**2**) also showed some selectivity for KDM4E over FIH (60.2 μM IC_{50}, 11-fold selectivity). [59]

Elaboration of 2,4 PDCA was approached in a similar manner. Crystal structures were used to predict the best position from which to derivatize in order to extend towards the peptide binding pocket (**Figure 4C**), leading to the synthesis of a diverse series of 3' substituted derivatives. Only one compound, a simple amino derivative (**4**), achieved increased potency against KDM4E relative to 2,4 PDCA (0.11 μM vs. 0.44 μM). Notably, this compound showed equivalent inhibition against PHD2 as the parent scaffold (~80 % inhibition at 400 μM), and therefore increased selectivity. Another compound, an ortho-fluoro substituted benzylamine (**5**), showed a small decrease in potency against KDM4E relative to 2,4 PDCA (IC_{50} of 2.5 μM), but showed no inhibition of PHD2 up to 400 μM. Neither was tested in cells.[60]

Although there was no pre-existing structural information for the bipyridyl inhibitor, it was predicted to bind in analogy to 2,4 PDCA, with the pyridyl nitrogens chelating the active site iron and the carboxylate coordinating the side chains of tyrosine and lysine. Therefore, derivatization was performed at the 5' position, which is predicted to face the peptide binding pocket. A small panel of derivatives resulted in identification of the phenylethylamide (**10**), which has an IC_{50} of 0.11 μM against KDM4E, a 66-fold improvement over the initial bipyridyl. A related compound, an *N*-(2-aminoethyl)amide derivative, was crystallized with KDM4A (**Figure 4E**), confirming the predicted binding pose. No selectivity data or cell assays are reported. Together, these derivitization efforts from the known αKG mimics NOG, 2,4 PDCA, and bipyridyl demonstrate the feasibility of targeting the JmjC demethylases with small molecules, and hint at the possibility of elaborating from an αKG mimic to achieve potent and selective inhibition.[61]

Another effort began with αKG itself, and attempted to increase potency, selectivity, and cell activity by changing the metal chelation properties of the scaffold as well as derivatizing towards the peptide binding pocket. First, the oxalic acid metal chelating moiety of αKG was exchanged for the more powerful and less hydrophilic hydroxamic acid group. The resulting scaffold was 15-fold more potent against KDM4C as compared to NOG. Interestingly, while NOG inhibits PHD2 almost 100-fold more potently than KDM4C (although the assays used are very different, making this comparison suspect), the hydroxamic acid derivative of αKG does not inhibit PHD2 up to 100 μM, the highest concentration tested. Next, a dimethylamino group with a variable length alkyl linker was appended to the carbonyl of the hydroxamic acid moiety in an effort to increase potency by engaging the methyllysine binding pocket. This investigation revealed an optimum linker length of 8 carbons, an IC_{50} for this compound (**18**) of 1.0 μM against KDM4C, and approximately equipotent inhibition of KDM4A. Selectivity against PHD1 and PHD2 was over 100-fold, selectivity for the KDM4 subfamily against KDM5A was approximately 4-fold, and selectivity against KDM7B was approximately 6-fold. A methyl ester prodrug of this compound was effective in inhibiting growth of the prostate carcinoma cell line LNCaP when given in combination with an LSD1 inhibitor, showing an EC_{50} of approximately 20 μM.[62] A follow-up study found that the tertiary nitrogen was dispensable for inhibition of KDM7B, but not for KDM4A, KDM4C, and KDM5A. Further optimization resulted in the KDM2/7 selective inhibitor (**19**), which is approximately 10-fold selective over KDM5A and KDM4C, and does not inhibit KDM6A up to 100 μM. Interestingly, (**19**) is cell active without esterification, and causes a dose-dependent increase in H3K27me2 levels in treated N2a,

HeLa, and KYSE150 cells, along with inhibition of proliferation at mid-micromolar concentrations.[63]

Besides the re-purposed scaffolds, others have been identified through the use of various screens. Interestingly, many of these scaffolds are similar to ones previously described as αKG dependent oxygenase inhibitors, perhaps due to limited ways to satisfy key αKG mimicking interactions found in nearly all such inhibitors.

One screen of over 200,000 diverse small molecules identified several 8-hydroxyquinolines as low micromolar inhibitors of KDM4E. Notably, 8-hydroxyquinolines have previously been investigated as HIF-1α inhibitors. Following the screen, a small panel of derivatives was tested, and the most potent was IOX1 (**6**), with an IC_{50} against KDM4E of 0.2 μM, and some selectivity versus FIH and PHD2 (9 and 6 fold, respectively). A crystal structure shows that the compound mimics the binding interactions of αKG (**Figure 4D**). In cells, IOX1 was found to inhibit transfected/overexpressed KDM4A with an EC_{50} of approximately 87 μM while cytotoxicity testing revealed a CC_{50} of approximately 292 μM. Despite the presence of a carboxylic acid, IOX1 is active in cells without the use of a prodrug strategy. [64]

Figure 4: Crystal Structures of KDM4 Inhibitors

(A) Crystal structure of NOG and methylated H3K9 peptide bound to KDM4A. PDB ID 2Q8C. (B) Crystal structure of NOG derivative bound to KDM4A. PDB ID 2WWJ. (C) 2,4 PDCA bound to KDM4A. PDB ID 2VD7. (D) 2-carboxy-8-hydroxyquinoline (IOX1) bound to KDM4A. PDB ID 3NJY. (E) Bipyridyl inhibitor bound to KDM4A. PDB ID 3PDQ. Superposition of substrate peptide has been included in all structures for clarity but is not generally co-crystalized with bound inhibitor.

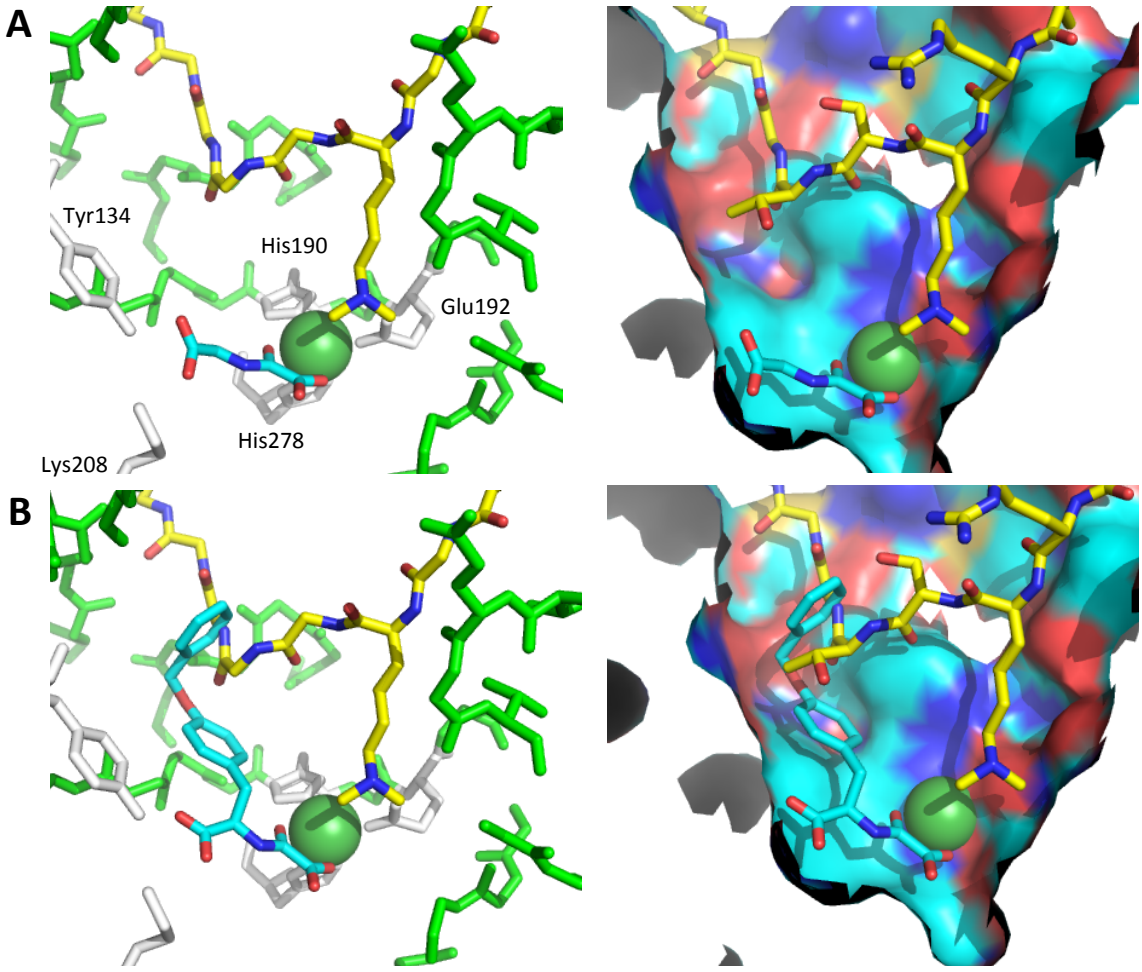

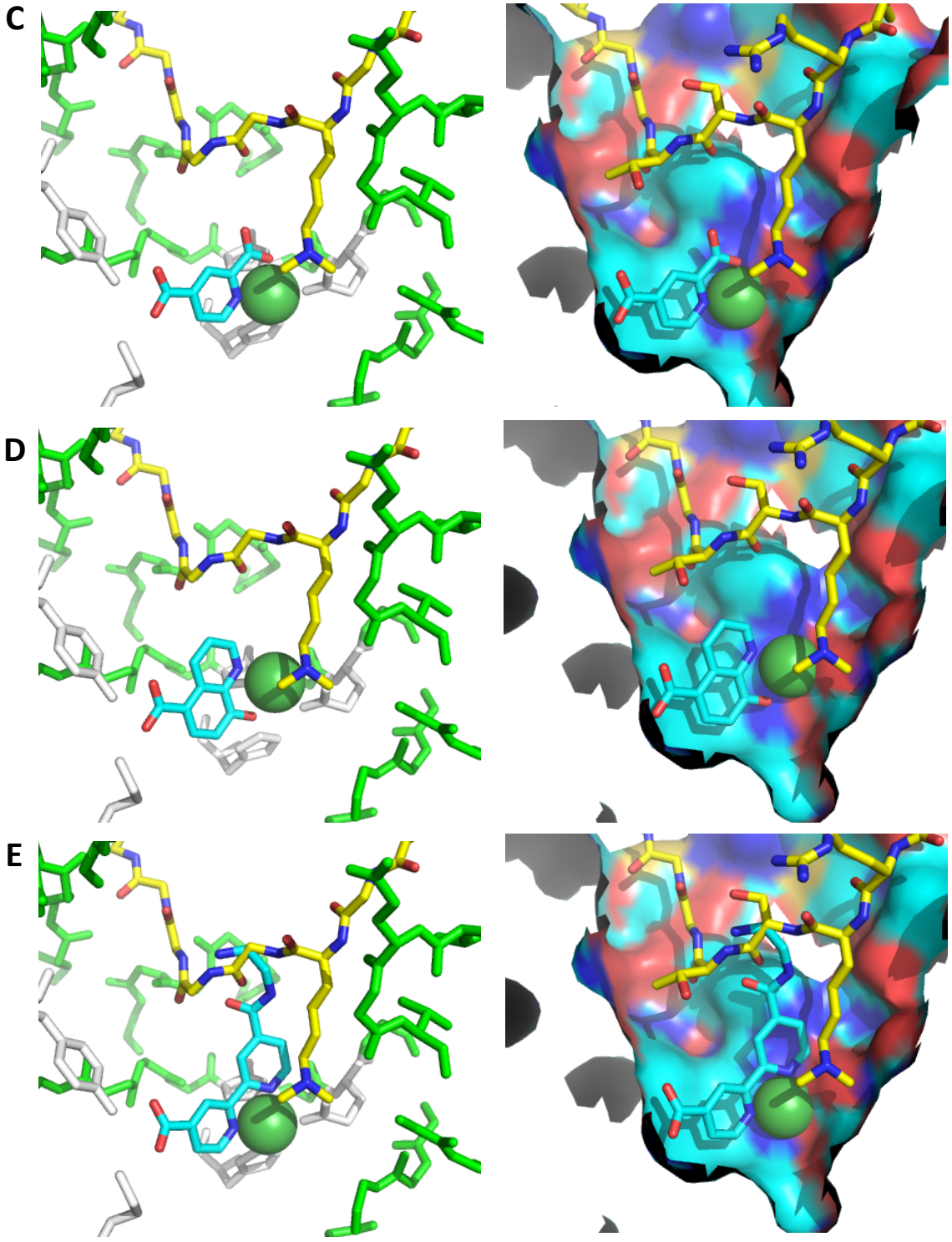
C
D
E

Several derivatives of 8-hydroxyquinoline tested in the original report lacked a carboxylic acid moiety, usually leading to a significant loss in potency. Some derivatives without a carboxylic acid, most notably (**7**), which has an ortho-fluoro aniline in its place, suffer only modest decreases in potency, in this case to 1.1 μM against KDM4E (5-fold decrease relative to IOX1).[64] Subsequent efforts have focused on replacing the carboxylic acid in order to increase cell activity, with two notable results.

In the first study, a panel of derivatives was synthesized, both with and without carboxylic acids. The most potent of these (**8**) lacked a carboxylic acid, and was approximately equipotent to IOX1. Only one selectivity assay was performed, showing >100 fold selectivity over the flavin-dependent demethylase KDM1A. Although this compound showed favorable ADME properties and stability in buffer, direct testing of the cellular activity of this compound was not performed. However, in a cellular model of KDM4 activation of Herpes Simplex Virus immediate-early (IE) genes, compound (**8**) reduced IE expression with an IC_{50} of 10 μM.[65] Overall, compound (**8**) is the most advanced KDM4 inhibitor described thus far, but further characterization especially with respect to selectivity is required.

In another effort to improve IOX1, a variety of ester prodrugs were synthesized. Surprisingly, while a methyl ester resulted in decreased *in vitro* potency against a panel of JmjC proteins, longer alky esters resulted in a partial recovery of potency against the KDM4 family, and KDM4C in particular. An n-octyl ester (**9**) showed 12-fold selectivity for KDM4C versus KDM4E, and greater than 26 fold selectivity against KDM2A, KDM3A, KDM5C, KDM6B, and PHD2, making this easily the most selective KDM4 inhibitor thus far described. In cells, this compound shows an EC_{50} against

transfected/overexpressed KDM4A of 3.8 μM. Strangely, however, compound (**9**) potently stabilizes HIF-1α in cells, which likely results from inhibition of HIF hydroxylases such as PHD2. Although inhibition of PHD2 by (**9**) was tested *in vitro* and found to be negligible, it is possible that (**9**) inhibits another HIF hydroxylase, or that (**9**) is hydrolyzed in cells to IOX1, which is known to inhibit PHD2 among other hydroxylases. [66] Further investigation of the cellular selectivity of (**9**) is necessary to understand the apparent discrepancy between the *in vitro* and cellular activity. Overall, however, this compound demonstrates the possibility of selective inhibition by a small molecule even within the highly conserved KDM4 subfamily.

In the largest reported JmjC inhibitor screening effort to date, a test of the approximately 2 million compounds in the GlaxoSmithKline compound library against the H3K27 demethylase KDM6B identified a bipyridyl scaffold that was subsequently elaborated resulting in (**12**). *In vitro*, this compound has an IC_{50} against KDM6B of 60 nM, and is selective for the KDM6 subfamily over the KDM3 and KDM4 subfamilies. Only minimal selectivity is seen against the KDM5 subfamily. In cells, the ethyl ester prodrug of (**12**) was found to inhibit transfected/overexpressed KDM6B at a concentration of 25 μM. [67] However, the esterified prodrug itself was found to inhibit a wide range of αKG dependent oxygenases with low micromolar potency *in vitro*, and in cells it was found to inhibit KDM6B, KDM5B and KDM4C with similar potencies. [68] This result encourages caution in extrapolating from *in vitro* activity to cellular activity, as well as demonstrating a potential drawback to the prodrug strategy, namely, that the prodrug may be active on its own.

In an attempt to bypass the problem of poor cell activity without resorting to late-stage modifications of a successful *in vitro* inhibitor, a screen was conducted using a cellular reporter of locus derepression which found the compound (**13**), followed by *in vitro* assays to show that (**13**) inhibits the JmjC demethylases with some selectivity over the hydroxylase PHD2. Notably, this compound is highly active in cells, and is selectively toxic to prostate and lung cancer cell lines as compared to non-cancerous primary or immortalized prostate and lung cell lines. Furthermore, this compound prolonged survival in a mouse xenograft model of breast cancer. [69] Overall, this example demonstrates the promise of using cell-based screening to find cell active small molecules, as well as the exciting potential utility of JmjC demethylase inhibitors in treating cancer.

A very different screening attempt used phage display followed by semi-rational optimization to identify peptidic inhibitors of several demethylases. Notably, the resulting inhibitors do not bind competitively with either peptide substrate or αKG cosusbtrate. Hydrogen-deuterium exchange experiments indicate that several inhibitors targeted to KDM4C share a similar binding surface that is large, distinct from the substrate binding region, and non-contiguous. The last point may indicate multiple binding sites for each inhibitor, a possibility that is supported by IC_{50} curves with low (<1) Hill coefficients. Although these compounds are not selective within the KDM4 subfamily, full selectivity screening has not been performed. As expected due to their peptidic structures, these compounds are not cell active. [70]

Another general strategy has been to design peptide substrates fused to αKG analogs. By careful choice of a peptide substrate this strategy exploits the high degree of

substrate specificity that is a property of many JmjC demethylases to provide highly selective inhibition of a JmjC subfamily or even selectivity within JmjC subfamilies. Fusion to an αKG analog substantially increases potency through an avidity effect as well as preventing turnover of the substrate. In one example, an H3K9(me3) 8-mer peptide fused to NOG (**14**) achieved a 90 nM IC_{50} against KDM4E and a similar potency against KDM4A, but no detectable inhibition of any of several other JmjC demethylases and hydroxylases tested. In another example, an H3K36(me3) 11-mer fused to NOG was able to inhibit KDM4A with an IC_{50} of 1.5 μM, and 60-fold selectivity over KDM4E. [71] Although this result demonstrates the promise of targeting both the peptide and αKG binding sites simultaneously, the peptidic nature and resulting lack of cell activity of these inhibitors limits their utility as cellular probes of demethylase function.

However, if key binding interactions between the enzyme and substrate peptide could be mapped, it may be possible to incorporate these interactions into a more drug-like small molecule. In a first step towards this goal, several different lengths of methylated H3K9 substrate peptides were tested for activity using three H3K9 demethylases: KDM4A, KDM4C, and KDM7B. Interestingly, KDM4C was uniquely tolerant of shorter substrates, showing only slightly reduced activity against a 5-mer as compared to a 14-mer. KDM4A and KDM7B, on the other hand, were unable to demethylate 5-mer substrates. Synthesis of a 5-mer peptide attached to 5-bromouracil (**15**), a metal-chelating small molecule that in this case likely functions as an αKG mimic, resulted in inhibition of KDM4C with a K_i of 27 μM, similar potency against KDM4A, and no detectable inhibiton of KDM7B. [72] This result suggests that potent and selective inhibition of the KDM4 subfamily may be possible by exploiting a relatively limited set

of interactions. Of note, this inhibitor lacks a trimethyllysine moiety, which is responsible for a majority of the binding affinity between the demethylase and its peptide substrate (Noah Younger, unpublished data). It is likely that potency could be greatly increased by exploiting this key interaction. Although a more thorough investigation of the selectivity of these inhibitors is necessary, studies such as these promise to greatly increase our understanding of binding interactions in the active sites of the JmjC demethylases.

As mentioned above, the peptide-like compounds are not generally good inhibitors, as they typically have poor cell activity, as well as poor PK/PD properties. Therefore, the strategy of designing a bivalent inhibitor targeting both the αKG binding pocket as well as the peptide substrate binding pocket will ultimately require developing more drug-like compounds rather than the peptidic compounds that have been discussed so far. One notable attempt has already been made in this direction, with the linking of an αKG analog to a methyllysine mimicking small-molecule fragment derived from the HDAC inhibitor MS-275 to make compound (**16**). Overall this compound shows modest potency and selectivity, but is able to inhibit demethylation in cells when administered as a methyl-ester pro-drug. [73] Future work will be necessary to enhance selectivity, perhaps by exploiting the interactions found using the above peptide truncation approach.

Another effort to target the JmjC demethylase peptide binding pocket used the H3K9 methyltransferase G9a inhibitor BIX-01294 as a starting point. This small molecule mimics residues 4-8 of the histone H3 tail and has favorable drug-like properties. Structure-based optimization of this compound resulted in a derivative (**17**) with an IC_{50} for the H3K9(me2) demethylase KDM7A of approximately 3 μM, similar

potency against the H3K9(me2) demethylase KDM7B, approximately 36-fold selectivity over the methyltransferase G9a, and an IC_{50} greater than 10 μM against the H3K4 demthylase KDM5C. Detailed cellular activity studies were not performed, although this compound was found to be cytotoxic to fibroblasts at mid-micromolar concentrations. A crystal structure of inhibitor bound to KDM7A shows that the compound binds as expected, is not competitive with αKG, and seems to make several interactions with its target that are similar to those made by the peptide substrate. [74] There are also several key interactions such as those in the methyllysine binding pocket that are not exploited by the inhibitor, suggesting clear avenues for future derivatization.

Two classes of inhibitors are unpublished, but are described in patents. Compounds of type (**20**) were profiled *in vitro* against KDM5A, KDM5B, KDM4C, KDM4A, and FBXL10. Although only ranges of IC_{50} values are reported instead of exact values, some compounds seem to show greater than 10-fold selectivity for either the KDM5 family or for FBXL10, with IC_{50}'s under 100 nM. In cells, a single tested compound showed an EC_{50} under 100 nM, with a number of others in the 0.1-1 μM range. [75] Unfortunately it is difficult to compare *in vitro* activity with cell activity based on the information presented in the patent. Interestingly, many of the highly cell active compounds have carboxylic acid moieties.

Another class of patented compounds is built on a pyridine core with an N-alkyl 2-methylamino group with a variable length alkyl linker terminated by a secondary amine, and either an aldehyde or a methyleneamino ethanol group at the 4-position. One example is compound (**21**), which has an IC_{50} of less than 250 nM against KDM5B and KDM5C, and an IC_{50} of between 250 nM and 2.5 μM against KDM4B. Its IC_{50} is over

2.5 μM for all other demethylases tested (KDM4C, KDM2B, KDM3A, KDM3B, KDM4A, KDM6B, PHF8, KDM6A). This compound is also highly active in cells using a number of assays: it causes an increase in H3K4me3 levels in U2OS cells with an IC_{50} of less than 250 nM, it inhibits transfected KDM5B with an IC_{50} of less than 250 nM while its IC_{50} for transfected KDM4C and KDM4A is greater than 2.5 μM, and it inhibits MCF7 proliferation with an IC_{50} under 250 nM. A related compound, though not quite as selective *in vitro*, was used in an OPM-2 tumor xenograft study to show dose-dependent inhibition of tumor growth. [76] Overall, these patented inhibitors, although not targeted to the KDM4 subfamily and without complete characterization, demonstrate the possibility of selectively targeting a subfamily of JmjC demethylases.

Chapter 2: Docking and Linking Fragments to Discover Histone Demethylase Inhibitors

I. Introduction

Methylation of lysine residues in histone proteins profoundly impacts the regulation of cellular processes such as transcription, formation of heterochromatin, genomic imprinting, and X-chromosome inactivation. The discovery of a lysine-specific demethylase 1 (LSD1) and Jumonji C (JmjC) domain-containing histone demethylases uncovered the dynamic character of lysine methylation, illuminating the regulatory role of this modification in gene expression. The Jumonji demethylases, the larger of the two demethylase families, is comprised of 33 JmjC domain-containing genes in humans[46]References out of which 24 are classified as histone lysine demethylases. [77] In the context of lysine demethylation, these enzymes use iron(II), α-ketoglutarate (αKG), and molecular oxygen to hydroxylate methyl groups attached to the ε-amino moiety of lysines, subsequently leading to the release of formaldehyde from a hemiaminal intermediate. Accordingly, they are considered "erasers" of the epigenetic code, complementing "readers" such as Bromo, PHD and Tudor domain proteins and "writers" such as acetyltransferases and methyltransferases, among others.

Aberrant lysine methylation, caused by mutation or misregulation of histone demethylases and histone methyltransferases, profoundly impacts cell physiology. Of particular interest is the hyperactivity of the KDM4 (also known as JMJD2) subfamily of the jumonji histone demethylases. The KDM4 subfamily members A-D have each been shown to promote oncogenesis in several contexts. [45-47,78] High levels of KDM4 protein expression is thought to promote oncogenesis in human tumors, especially in prostate cancer[48,79], but also in colon[49] and some breast[33] cancers.

The availibility of chemical probes for the KDM4 demethylases is critical for exploring their physiological and pathological roles. Since the discovery of Jumonji demethylases in 2006, several inhibitor classes have been identified (reviews[77,80-83]). While important, these molecules are largely pan-jumonji inhibitors often with only modest selectivity among isoforms, or between the demethylases and related oxygen-sensing enzymes, [60,69,73,84] such as FIH[82] and prolyl hydroxylases. [85] As important as these molecules are, especially given their cellular and in some cases *in vivo* activity, it is difficult to interpret their effects in complex systems due to inhibition of multiple targets.

Selective small molecule inhibitors for the KDM4 family would enable interrogation of the cellular functions of these histone demethylases, deconvoluting isoform specific from pan-demethylase effects, and from effects on the related oxygen sensing proteins such as FIH, as well as scaffolding from catalytic roles. To find such molecules, we turned to structure-based discovery and optimization of fragment inhibitors. Structure-based approaches have the advantage of finding new chemotypes that complement the structure of the target without resembling known scaffolds, [86] such as co-factor mimics. [87] In addition, fragment-based design can cover a much larger chemical space than that covered by larger molecules, also leading to new chemotypes. [88-92] We began with molecular docking screens of a library of 600,000 commercially-available fragments, [93] and found lead fragments that differed from known compounds but inhibited the enzyme with good ligand efficiency (LE) values. In a departure from common practice, we were able to leverage the docking poses to predict fusions of two different fragments into a single structure, leading to hybrid inhibitors with affinities improved by two log orders relative to the original fragments. Chemical synthesis,

isozyme profiling, and X-ray crystallography led to optimized molecules with a further two log order improvement in potency, with no detectable inhibition of FIH, and substantial selectivity over several other JmjC sub-families. Whereas molecular docking has been used previously to discover novel fragments for enzymes, the ability to optimize these by linking, based on docking orientations, is new to this study. The resulting molecules and X-ray structures provide templates for optimization of these molecules towards selective and cell-active probes of these critical demethylases.

II. Fragment Docking

Over 600,000 molecules from the ZINC fragment[93] (http://zinc.docking.org/browse/subsets/) were docked against the structure of the KDM4A demethylase. These molecules were commercially available, had a predicted octanol-water partitioning coefficient (XlogP) of less than 2.5, a molecular weight ≤ 250 Da, and fewer than five rotatable bonds. Docking was performed against the crystal structure of KDM4A (3PDQ, Chain B), due to the high resolution of the structure, a well defined loop (Ile 168-Val 171) near the rim of the active site, and five inhibitor structures that were available to use as controls for pose recapitulation (**Figure 1**). The high similarity within the KDM4 sub-family and especially the high conservation of active sites between KDM4A and KDM4C (100% identity of side chains facing into the active site), led us to expect that new compounds found would have similar inhibitory potencies towards both KDM4 family members. Fragments were docked in an average of 21,857 orientations and 42 conformations each; overall 1,571,034 complexes were calculated for the entire fragment library. Compounds were scored for fit to the active site based on van der Waals interactions, using the AMBER potential function,[94] point charge probes in pre-calculated electrostatic maps from Poisson-Boltzmann calculations,[94,95] and a correction for ligand desolvation.[96] From among the top 0.1% docking ranked fragments, 14 were chosen for testing, with ranks ranging from 59 to 426 out of 600,000 unique molecules docked (**Table 1**). Criteria for selection included the formation of favorable interactions with the iron center, for which the scoring function is only approximately developed,[97] the selection of novel and non-redundant chemotypes, and the elimination of poses with high internal energies, which are not always captured by the relatively

simple internal energy scoring of the Omega program used to calculate the docking conformations.[96] These post-docking criteria are widely used for "hit-picking", both in docking[98,99] and in high-throughput screening;[100] we emphasize that all of the compounds tested were among the very top-ranking 0.1% of the docking-ranked library. Of the 14 fragments tested, four inhibited KDM4C with an IC_{50} below 100 μM (LE values 0.32-0.45), as determined by TR-FRET using 2 μM α-KG (**Table 1**, entries 2-6), and three others had IC_{50} values in 100-200 μM range with LE values in the 0.21-0.41 range (**Table 1**, entries 7-9). Another nine molecules had affinities above 200 μM with LE values below 0.31 (**Table 1**, entries 10-16). All fragments originating from docking can be considered "hits," if a hit is defined as a compound that measurably inhibits the enzyme. If a more stringent criteria of IC_{50} value better than 200 μM and an LE of 0.3 or better is set, then the hit rate of identified compounds is 50 % (hit rate = number of actives/number tested).

Figure 1: Crystal Structures of KDM4A/B/C

These are examples of crystal structures of KDM4A/B/C deposited in the PDB. 3PDQ has the highest resolution and was used for docking.

PDB ID	**KDM4**A complexed with	Resolution
2GP5	2OG (alpha-Ketoglutarate) and Fe	2.28
2GP3	Apo structure with Ni	2.35
2OQ7	Ni and NOG (N-oxalylglycine)	2.15
2OQ6	Substrate structure, Histone H3 trimethylated peptide at Lys9, Ni and NOG (N-oxalylglycine)	2.0
2Q8C	Substrate structure, Histone H3 trimethylated peptide at Lys9, Ni and 2OG (alpha-Ketoglutarate)	2.05
2VD7	Inhibitor, Pyridine-2,4-dicarboxylic acid	2.25
2YBK	Inhibitor: (R)-2-Hydroxyglutarate	
2WWJ	inhibitor 10A	2.6
3NJY	Inhibitor: 5-carboxy-8-hydroxyquinoline	2.6
3PDQ	Inhibitor: Bipyridyl inhibitor KC6	1.99
	KDM4C complexed with	
2XML	N-Oxalylglycine and Ni	2.55

Table 1: Docking Results

Compounds selected from the docking screen were tested for *in vitro* inhibition of KDM4C. DR = Docking Rank; LE = Ligand Efficiency.

Compound	Docking Rank	IC_{50} (μM), 2 μM αKG	LE
1. 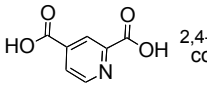 **1**	2,4-PDCA control	0.188	0.76
2. 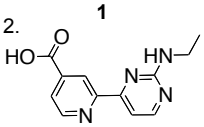 **2**	241	1.18	0.45
3. 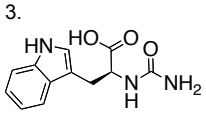 **3a**	339	18.6	0.36
4. 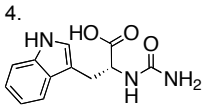 **3b**	339	54.7	0.32
5. 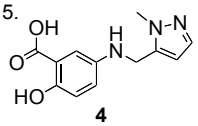 **4**	252	58.0	0.32
6. 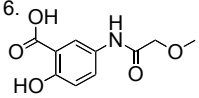 **5**	128	98.2	0.34
7. 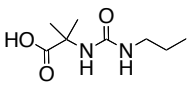 **6**	387	126	0.41
8. 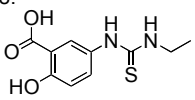 **7**	187	165	0.32
9. 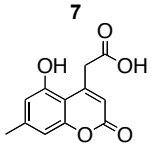 **8**	106	176	0.30
10. 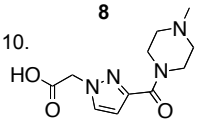 **9**	138	387	0.26
11. 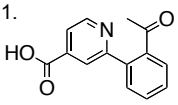 **10**	109	507	0.25
12. 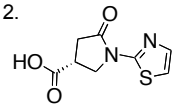 **11**	377	676	0.31
13. 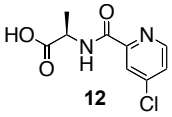 **12**	360	1210	0.27
14. 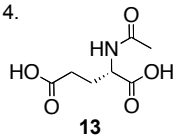 **13**	337	2070	0.28
15. 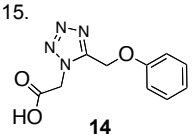 **14**	361	2320	0.21
16. 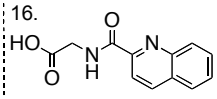 **15**	426	2810	0.20

III. Preliminary Characterization of 5-aminosalicylate Scaffold

Among the eight ligand-efficient fragments, three shared a common 5-aminosalicylate scaffold – **4**, **5**, **7** - with IC_{50} values ranging from 58 to 165 μM (**Table 1**). For all three compounds, the core aminosalicylate moiety had a shared docking pose in which the catalytic Fe(II) was coordinated by both carboxylate and hydroxyl moieties, while the 5-amino group hydrogen-bonds with Asp135 (**Figure 2**). Consistent with specific inhibition, neither **4** nor **5** formed colloidal aggregates by dynamic light scattering up to a concentration of 10 μM, neither inhibited an enzyme widely used for counter-screening colloidal aggregates at 0.2nM AmpC β-lactamase, nor was their inhibition of KDM4 perturbed by the addition of 0.01% Triton X-100 (**Table 2)**.

Figure 2: Salicylates series molecules identified from docking.

Docking pose for each salicylate molecule tested from initial docking screens. **4**, **5**, and **7** are predicted to bind the metal in a bivalent fashion through the carboxylate and hydroxyl, while the amide proton is predicted to form a hydrogen bond with Asp135 of KDM4A.

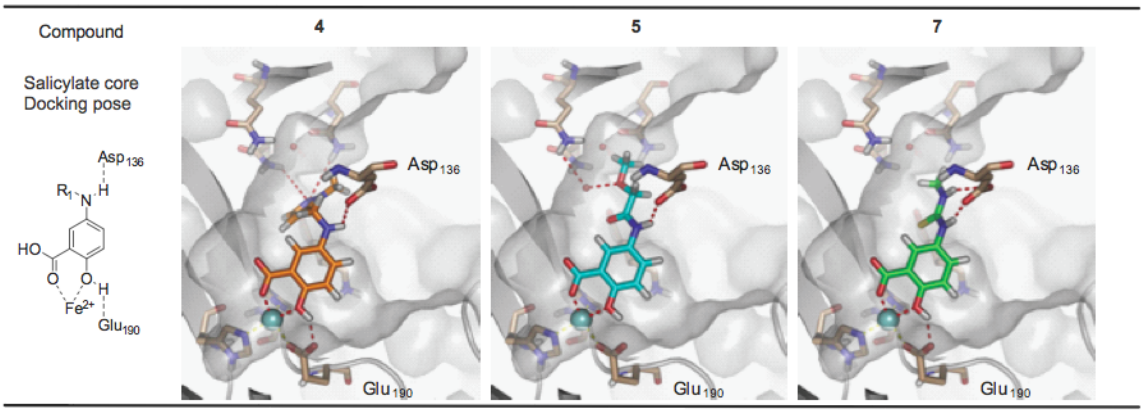

Table 2: Testing for Non-Specific Inhibition

Top: Two docking hits sharing a common 5-aminosalicylate core were tested for inhibition of AmpC. Neither shows significant inhibitory activity. Bottom: Two docking hits sharing a common 5-aminosalicylate core were tested for aggregate formation in solution. Neither shows significant aggregate formation.

	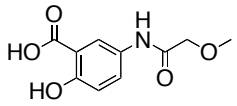 **5**	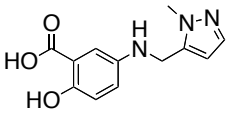 **4**
	% AmpC Activity	% AmpC Activity
Sample 1	105.9	103.7
Sample 2	99.8	122.9
Sample 3	97.6	100.8
AVE	101.1	109.1
ST DEV	4.3	12.0

	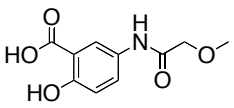 **5**				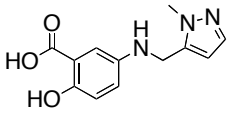 **4**			
Incubation Time	0 hrs		1 hr		0 hrs		1 hr	
	Intensity (Cnt/s)	R (nM)	Intensity (Cnt/s)	R (nM)	Intensity (Cnt/s)	R (nM)	Intensity (Cnt/s)	R (nM)
Sample 1	9269	0.4	8700	0.2	9580	0.2	8359	0.3
Sample 2	10137	0.3	8948	0.4	10112	0.4	8515	0.1
Sample 3	8605	0.2	9910	0.8	8833	0.5	11793	6.2
AVE Radius		0.3		0.47		0.37		2.2

IV. SAR of 5-aminosalicylate Scaffold

Initial efforts to optimize the 5-aminosalicylate derivatives were centered on analog-by-catalog from commercial vendors, and by synthesis of a small library of N-acyl and N-alkyl derivatives (**Table 3**). This resulted in only a modest improvement of potency. The most potent molecule obtained in this series was compound **21** with an IC_{50} of 5.1 μM, a 10-fold increase in activity over **4**. Overall, however, the analogs showed flat SAR, and no derivative emerged with affinity better than low μM.

Table 3: SAR of 5-aminosalicylate Scaffold

Synthesis of 5-aminosalicylate derivatives and their inhibitory potencies. Top: Synthetic routes to aminomethyl- and N-acyl salicylate derivatives. a) Typically, i. 5-aminosalicylate, R-CHO, EtOH, 100 °C, 1 hr; ii. $NaBH_4$, 100 °C, 1 hr; b) Typically, 5-aminosalicylate, R-COCl, MeCN, 20 °C, 3 hr. Bottom: IC_{50} values for selected 5-aminosalicylate derivatives tested for inhibition of KDM4C using TR-FRET assay with 2 μM α-KG.

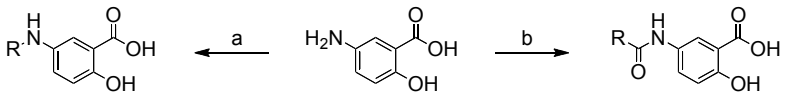

	Compound	IC50, μM 2 μM αKG		Compound	IC50, μM 2 μM αKG		Compound	IC50, μM 2 μM αKG
1.	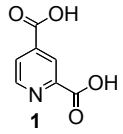 **1**	<0.050	6.	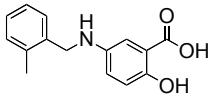 **20**	42	11.	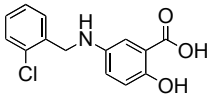 **25**	22
2.	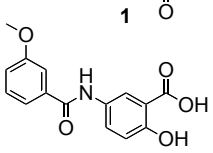 **16**	180	7.	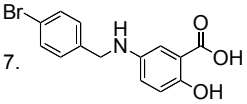 **21**	5.2	12.	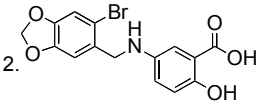 **26**	32
3.	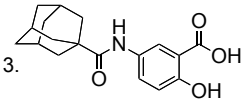 **17**	72	8.	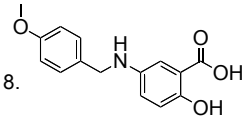 **22**	57	13.	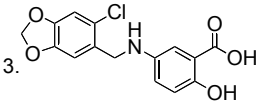 **27**	22
4.	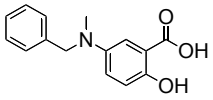 **18**	61	9.	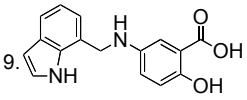 **23**	72	14.	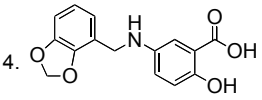 **28**	15
5.	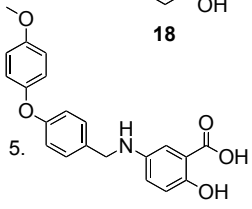 **19**	87	10.	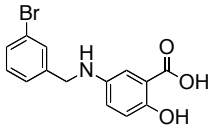 **24**	134			

V. Optimization by Fragment Linking

As derivatization of the amino moiety in 5-aminosalicylates did not yield major improvements in potency, we returned to our observation that the salicylates could adopt two high-scoring poses in the active site. While most highly-ranked salicylates docked in the pose dominated by iron chelation through carboxylate and alcohol moieties (**Figure 2**) a subset of salicylates paired the carboxylate with Lys206 and Tyr132 in the active site of the enzyme (e.g., **29, Figure 3**). Intriguingly, Lys206 and Tyr132 form a similar interaction with the γ-carboxylate of the cosubstrate α-ketoglutarate (αKG), raising the possibility that fusion of fragments, if geometrically feasible, may result in molecules that would not only coordinate iron but also engage the region of the active site responsible for the coordination of the terminal carboxylate of αKG. The observation that the docking pose of compound **29** superposes well with 2,4-PDCA in the crystal structure of 2,4-PDCA bound to KDM4A (pdb ID 2VD7)[85] provided further support for our fragment fusion strategy. Three hybrid scaffolds (A-C, **Figure 3C**) were compoutationally constructed and had favorable scores and poses. Whereas fragment linking and fusing even when based on experimental structures of the fragments is often considered risky,[101] the docked geometry of these linked compounds seemed attractive, complementing all polar groups without obvious strain. We therefore decided to pursue compounds containing hybrid scafold B (**Figure 3C**).

Figure 3: Docking-based fragment linking.

A) Superposition of two docking poses of the salicylates. B) Structures of salicylate fragments, indicating key interactions. C) Twelve hybrid scaffolds were tested in silico with three, shown here, giving good scores while maintaining hypothesized network of interactions. D) Overlay of a docking pose and a crystal structure of a representative hybrid scaffold synthesized in this study.

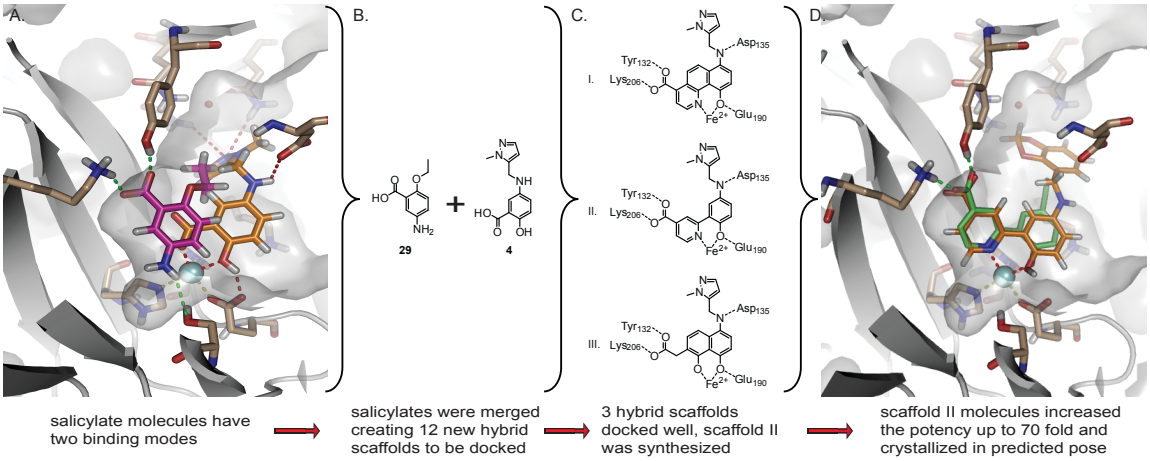

VI. SAR of Hybrid Scaffold

We synthesized the core hybrid scaffold via Suzuki-Miyaura coupling (**Table 4**). Simultaneous nitro group reduction and methyl ether deprotection was followed by acylation of the amino group to generate a small library of N-acylated hybrid analogs (**Table 4**, entries 4-15). Many of the hybrid derivatives strongly inhibited KDM4C, with several – **35**, **36**, **39** - showing IC_{50} values below 70 nM, under the same conditions as the initial TR-FRET assay performed with 2 μM α-KG. Because these potencies are below the ability of the assay to reliably measure inhibition of KMD4C, these compounds were subsequently retested in the presence of 50 μM α-KG. These more stringent conditions allow for more accurate determination of IC_{50} values and a better comparison of relative potencies of tested compounds. Under these more stringent conditions, several molecules showed low micromolar inhibition of KDM4C – **35**, **36**, **39**, **40**, and **42**.

Table 4: Synthesis and inhibitory potencies of acylated hybrid scaffolds.

Top: synthetic route to N-acyl hybrid derivatives. c) Pd6 mixed catalyst, Cs_2CO_3, 20:1 acetonitrile/water, 100 °C, 24 hr; d) NaI, HBr, 110 °C, 4 days; e) Typically, i. NHS, R-COCl, MeCN, 20 °C, 1 hr; ii. SPSA011, 1:1:1 MeCN:H_2O:MeOH, 20 °C, 16 hrs.

Bottom: selected hybrid derivatives tested for inhibition of KDM4C using TR-FRET with the indicated concentration of α-KG.

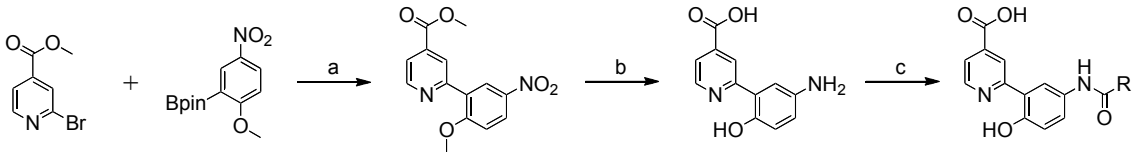

Compound	IC_{50} (μM), 2 μM αKG IC_{50} (μM), 50 μM αKG	Compound	IC_{50} (μM), 2 μM αKG IC_{50} (μM), 50 μM αKG	Compound	IC_{50} (μM), 2 μM αKG IC_{50} (μM), 50 μM αKG
1. 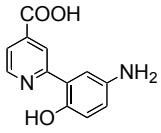 **30**	8.3 N.D.	6. 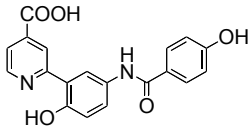 **35**	0.064 2.6	11. 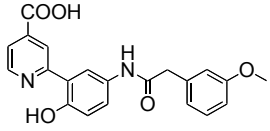 **40**	0.14 1.5
2. 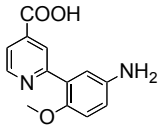 **31**	310 N.D.	7. 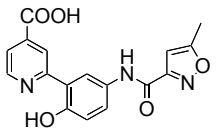 **36**	0.065 5.0	12. 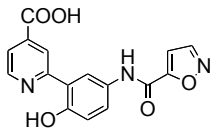 **41**	1.02 N.D.
3. 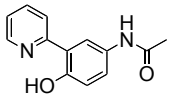 **32**	N.I.	8. 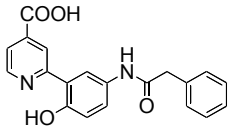 **37**	0.43 17	13. 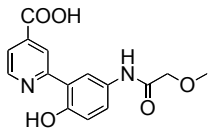 **42**	0.14 7.4
4. 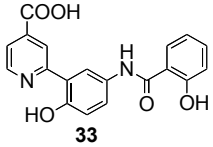 **33**	4.6 N.D.	9. 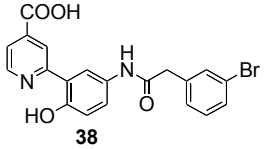 **38**	0.17 3.4	14. 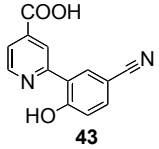 **43**	6.0 N.D.
5. 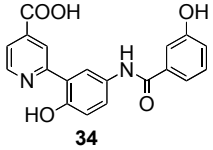 **34**	0.46 N.D.	10. 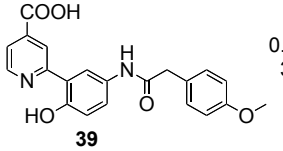 **39**	0.069 3.7	15. 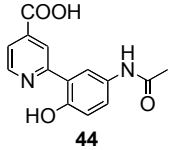 **44**	1.2 40

The advantage conferred by the hybrid molecules over the lead salicylates is best illustrated by direct comparison of correspondingly derivatized compounds (**Table 5**). Compared to the amino derivatized salicylate derivatives, the potencies of hybrid molecules are improved as much as nearly three orders of magnitude. The greatest improvement between corresponding derivatives was observed for **5**, which has a measured IC_{50} of 98 μM, and **42**, which under identical assay conditions has a measured IC_{50} of 0.14 μM, a difference of 700-fold (**Table 5**). Several other pairs of compounds, such as **4** vs **45** and **28** vs **46,** showed good improvements in affinity, if not to quite the same extent. Naturally, there were also exceptions where the hybrid scaffold did not improve the potency, such as compound **21** vs. compound **47** (**Table 5**).

Table 5: Potency comparison between 5-aminosalicylates and the corresponding hybrid molecules.

Selected 5-aminosalicylate and hybrid derivatives tested for inhibition of KDM4C using TR-FRET with 2 μM α-KG.

Compound	IC_{50} (μM), 2 μM αKG	Compound	IC_{50} (μM), 2 μM αKG
1. 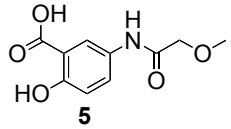 **5**	98	5. 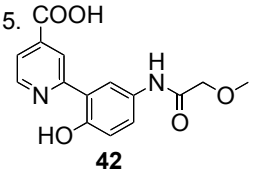 **42**	0.14
2. 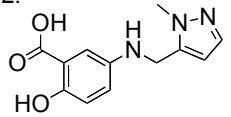 **4**	58	6. 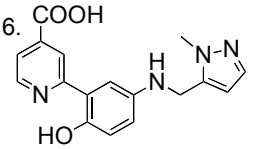 **45**	0.77
3. 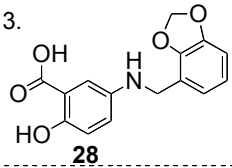 **28**	15	7. 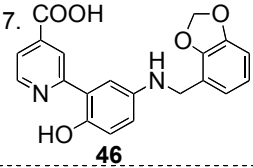 **46**	0.56
4. 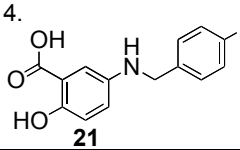 **21**	5.2	8. 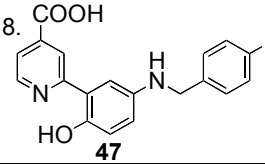 **47**	2.5

VII. Inhibitory Mechanism of Hybrid Scaffold Derivatives

Two of the most potent acylated hybrid derivatives, **42** and **35**, were selected for further *in vitro* characterization. We first determined through competition assays that both compounds bind competitively with respect to αKG, but not with respect to peptide substrate (**Table 6**). Because of the variability we observed in IC_{50} measurements across different types of assays and especially with changes in the concentration of αKG, we sought to measure K_i values for these inhibitors. In full competition assays, **42** and **35** had measured K_i values of 0.68 μM and 0.043 μM, respectively, and are competitive with αKG (**Figure 4 A,B**, **Table 6**). As a control, the generic inhibitor 2,4-PDCA(**1**) was also tested and as expected it had a competitive mode of inhibition with respect to αKG and a K_i of 0.002 μM **(Figure 4C, Table 6)**. Of note, for compound **42** we measure a lower IC_{50} (0.14 μM, **Table 4**) than K_i (0.38 μM, **Table 6**). We believe this result can be explained by differences between the assays, as incorporating a pre-incubation step in the K_i assay in an effort to make the assays more similar substantially reduced the measured K_i (data not shown).

Table 6: K_i values for 1, 35 and 42.

A) Competition experiments performed with a range of αKG and peptide concentrations.

Compound	K_i (μM)	LE	IC_{50} (μM) for concentrations [αKG], [peptide] (μM)		
			[50],[50]	[50],[250]	[5],[50]
1. 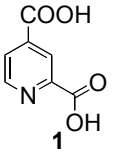 **1**	0.002	0.98	1.5	1.9	0.53
2. 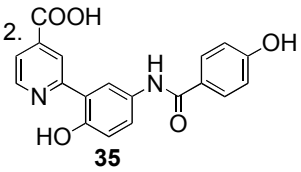 **35**	0.043	0.39	4.8	5.5	1.1
3. 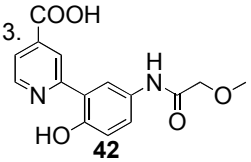 **42**	0.68	0.38	14.2	14.9	3.3

Figure 4: Lineweaver-Burk Plots of Competition with αKG.

Plots of 1/[α-KG] vs. $1/V_i$ for a range of concentrations of A) 42, B) 35, and C) 1. ● = 19 μM inhibitor, ■ = 6 μM inhibitor, ◆ = 2 μM inhibitor, ▲ = 0.7 μM inhibitor, ▼ = 0 μM inhibitor.

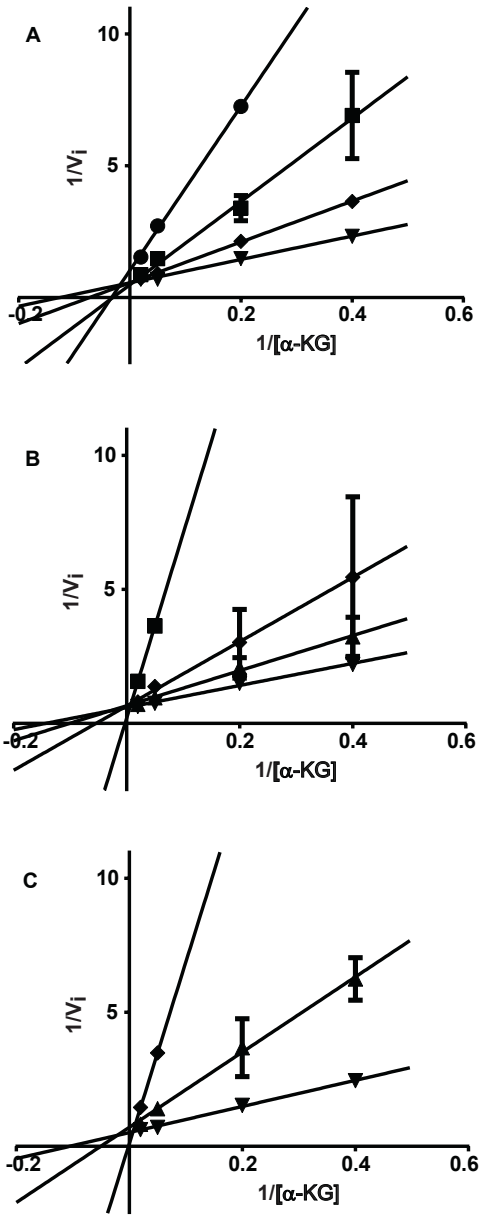

VIII. Selectivity of Hybrid Scaffold Derivatives

We next investigated the *in vitro* selectivity of five acylated hybrid derivatives against representative members of other subfamilies of JmjC domain-containing demethylases. We tested each inhibitor against the H3K4 demethylases KDM5A (JARID1A, RBP2) and KDM5B (JARID1B, PLU-1), the H3K27 demethylase KDM6B (JMJD3), the H3K36me2 demethylase KDM2A (FBXL11), the H3K9me1/2 demethylase KDM3A (JMJD1A), and the asparagine hydroxylase FIH (**Figure 5A**). The fold selectivity is calculated as the ratio of the IC_{50} for a given target and the IC_{50} for KDM4C obtained using the same type of assay. KDM5A and FIH selectivity is assayed by MALDI, using a consistent high concentration of αKG (100 μM). The remaining demethylases are assayed by AlphaScreen with αKG present at concentrations approximating the K_M for each enzyme. While the parent hybrid scaffold **30** shows only 6-fold selectivity for KDM4C over FIH (**Figure 5B, Table 7**), the N-acetyl derivatization of this core scaffold (**44**) leads to a strong enhancement in selectivity, as no activity is detected with this compound against FIH at the limit of the MALDI assay (IC_{50} >500 μM) (**Table 7**). This selectivity for inhibition of KDM4C over FIH is critical, given the important physiological role of FIH in regulating the transcriptional response to hypoxia. All tested derivatives show 6-fold or greater selectivity for KDM4C versus the H3K36me2 demethylase KDM2A, with the best selectivity (24-fold) achieved by **42**. Variable selectivity versus the H3K27 demethylase KDM6B was observed, ranging from less than 2-fold to greater than 26-fold, with **42** as the most selective compound. We note that the fold selectivity reported for **44** against KDM2A and KDM6B is a lower bound, as the compound is inactive up to the detection limits of the assay (IC_{50} >100 μM for

KDM2A and KDM6B). Poor selectivity was observed for KDM4C versus the H3K4 demethylases KDM5A and KDM5B. Finally, these compound show minimal selectivity for KDM4C versus the H3K9me1/2 demethylase KDM3A. As expected, our inhibitors do not discriminate between KDM4 isoforms (KDM4C vs KDM4D, **Table 7**)

Figure 5: JmjC Phylogenetic Diagram and Selectivity of Hybrid and Acetyl Derivative.

A) Phylogenetic diagram of the catalytic domains of selected JmjC proteins, with KDM4C highlighted in red, and enzymes used in counter-screening highlighted in blue. **B**) Selectivity of hybrid scaffold **30** for KDM4C over FIH (6-fold) compared to selectivity of acetylated derivative **44**, which does not inhibit FIH.

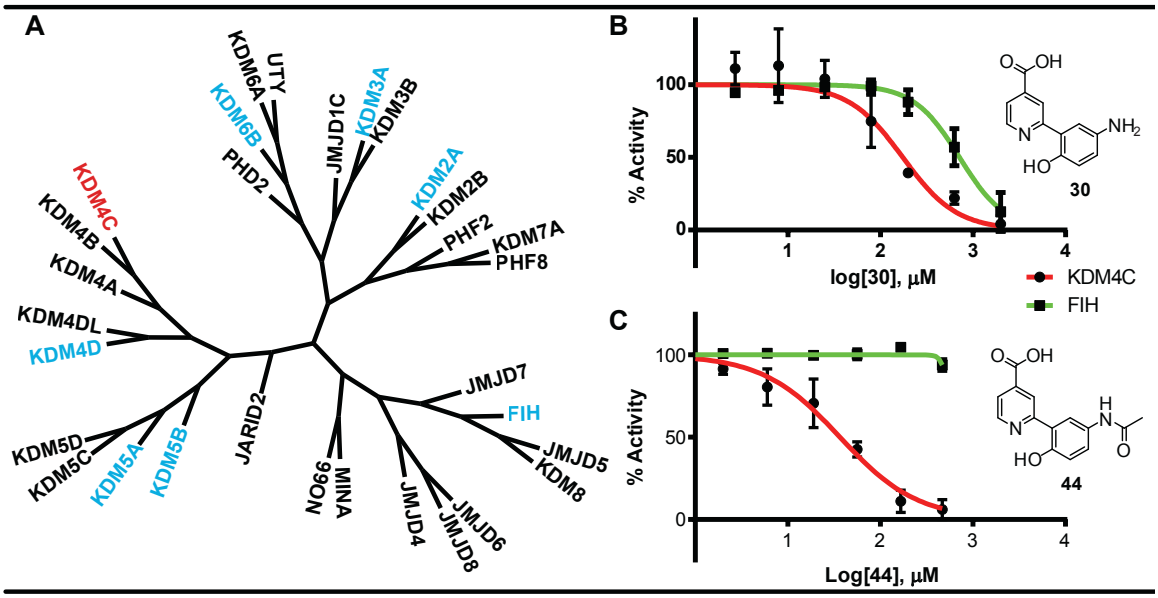

Table 7: Selectivity of Hybrid Derivatives.

Selectivity against FIH and KDM5A was determined by a MALDI assay with 100 μM αKG. For comparison, potency of these molecules against KDM4C was determined under identical conditions. Selectivity against other JmjC domain containing proteins was determined by AlphaScreen. αKG concentrations used are approximately the K_M for each of the enzymes: KDM2A, 10 μM αKG; KDM6B, 2 μM αKG; KDM5B, 5 μM αKG; KDM3A, 5 μM αKG; KDM4C, 2 μM αKG; and KDM4D, 2 μM αKG. ND = not determined in this study, values have been reported elsewhere.[102]

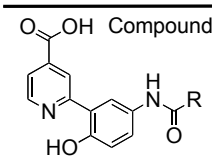 Compound	MALDI Assays			AlphaScreen Assays					
	KDM4C	FIH	KDM5A	KDM4C	KDM2A	KDM6B	KDM5B	KDM3A	KDM4D
	IC_{50} (μM) (selectivity)			IC_{50} (μM) (selectivity)					
1. 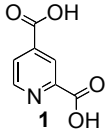 **1**	0.42	8.6 (20)	0.76 (2)	2.6*	4.1* (2)	33* (13)	ND	8.0* (3)	1.1* (-2)
2. R =  **44**	63	>500 (>8)	240 (4)	15	>100 (>6)	>100 (>6)	72 (5)	33 (2)	14 (1)
3. R =  **42**	47	>500 (>11)	180 (4)	3.8	91 (24)	>100 (>26)	12 (3)	11 (3)	4.2 (1)
4. R = 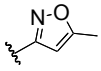 **36**	16	>500 (>31)	23 (1)	5.5	76 (14)	31 (6)	2.7 (-2)	5.7 (1)	9.2 (2)
5. R = 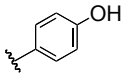 **35**	5.9	>500 (>85)	45 (4)	12	89 (7)	27 (2)	19 (1)	2.3 (-5)	13 (1)
6. R = 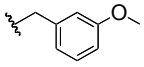 **40**	7.3	>500 (>68)	52 (7)	9.9	89 (9)	16 (2)	22 (2)	9 (1)	11 (1)

IX. Crystallography

An innovation of this study was the use of docking poses to guide fragment fusion—a strategy that is often considered risky even when guided by crystal structures. Though the fused ligands were up to 100-fold more potent than the initial hits, this apparent success is not fully compelling without atomic resolution structures. Therefore, to investigate the agreement between docking predictions and experimentally observed orientations, and to enable future elaboration, crystal structures of hybrid compounds in complex with KDM4A, a representative KDM4 enzyme that is well suited for crystallographic studies,[59,61,64,85] were determined with **35**, **36**, **40**, **42**, **43**, and **44** (**Figure 6A-F**). The resolution of the structures ranged from 1.82 to 2.39 Å (**Figure 6**). Unambiguous positions for the ligands in the structures were identified in unbiased difference density maps (Fo-Fc for compound **36** contoured at 2.5s **Figure 6H**), and refined well to place the inhibitors.

In each of the six complexes, the 2-(3-amino-6-hydroxyphenyl)pyridine-4-carboxylic acid scaffold of the compounds superposes well with the docked pose, making almost all the same key interactions with the metal and αKG pocket (**Figure 6**). As predicted in the docking poses, in all six structures the inhibitor carboxylate salt bridges with Lys206 N^{ε} (~2.7 Å), and hydrogen bonds with Tyr132 OH (~2.7 Å), mimicking the interactions observed between the carboxylic acid of the α-KG cofactor in the active site (pdb ID 2OX0). [19,20] Similarly, in both the docking and the crystal structures, the inhibitor pyridine ring stacks with Phe185, while the pyridine nitrogen, as expected, chelates the active site metal (Ni^{2+} or Mn^{2+} as a mimic of oxygen sensitive Fe^{2+}), an interaction analogous to the interaction between the metal and previously identified inhibitors like

2,4-PDCA (pdb ID 2VD7) [85] and 4'-[(2-aminoethyl)carbamoyl]-2,2'-bipyridine- 4-carboxylic acid (pdb ID 3PDQ). [61] The second interaction formed with the metal is with the hydroxyl moiety (~2.1 Å) of the N-acylamino substituted phenol ring. As in the docked structures, in the crystal structures this forms an octahedral geometry, with an angle of 171° between the inhibitor's hydroxyl group, the metal, and the N^{ε} of His276, with the other metal ligands derived from Glu190, His278 and a water molecule.

The one substantial difference between the docking poses and the crystallographic results is in the position of the exocyclic amide substituent, common to five compounds whose complex was determined **(Figure 6).** Whereas this has little effect on the overall placement of the inhibitors in the site, the details of the hydrogen-bonding to the enzyme change. In the docking predictions, the amide proton is predicted to hydrogen bond with Asp135. While a hydrogen bond between this amide and the protein is observed crystallographically, in some of the complexes (for example, **39**) the amide engages both Tyr177 and Asp135 through a bridging water molecule, while in the crystal structure of **47** with KDM4A, Tyr177 and Asp135 form water-mediated hydrogen bond with the oxygen atom of the exocyclic amide of the inhibitor.

Figure 6: Crystal structures of hybrid compounds in complex with KDM4A.

Six co-crystal structures were obtained with KDM4A and the hybrid salicylate series molecules **A) 43**, **B) 44**, **C) 36**, **D) 40**, **E) 35**, and **F) 42** to a resolution of 2.39, 1.82, 2.28, 2.27, 2.16, and 2.15 Å, respectively. Interacting residues are shown as sticks. G) As a representative structure, compound **36** (wheat) is superposed with the docked salicylate compound **4** (orange) and its corresponding docked hybrid scaffold II compound **45** (green). **H)** Omit map (green) for compound **36** contoured at 2.5σ. **I)** 2Fo-Fc composite omit map (gray) contoured at 1σ showing residues 5 Å around compound **36**. **J)** Surface representation of KDM4A active site with inhibitor **36**. **K)** Hydrogen bond network with compound **36**. **L)** Stacking interactions with compound **36**; the hydrophobic centers are indicated by a green sphere.

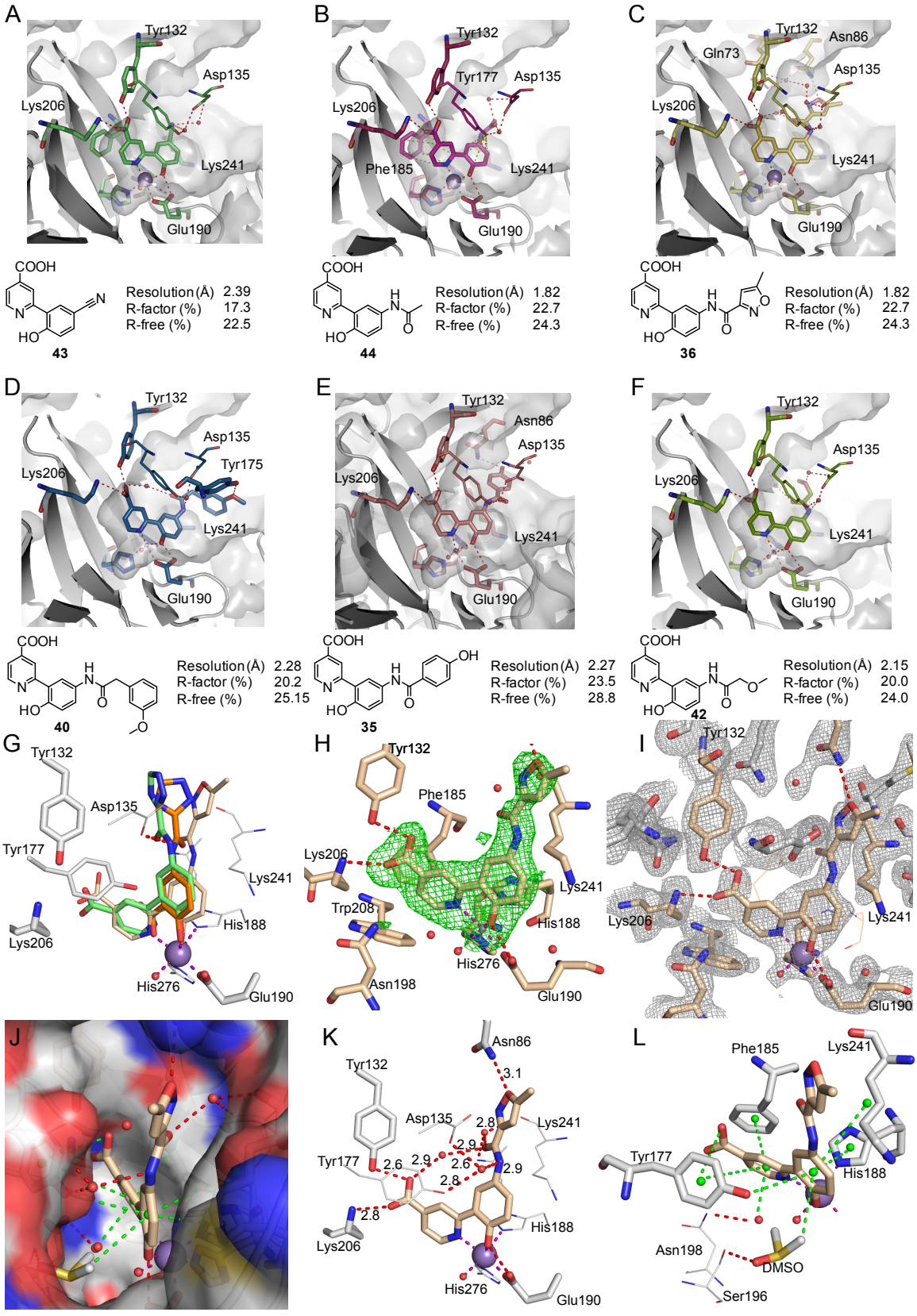
A
Tyr132
Asp135
Lys206
Lys241
Glu190
COOH
HO
43
Resolution (Å) 2.39
R-factor (%) 17.3
R-free (%) 22.5
B
Tyr132
Tyr177
Asp135
Lys206
Phe185
Lys241
Glu190
COOH
HO
44
Resolution (Å) 1.82
R-factor (%) 22.7
R-free (%) 24.3
C
Tyr132
Asn86
Gln73
Asp135
Lys206
Lys241
Glu190
COOH
HO
36
Resolution (Å) 1.82
R-factor (%) 22.7
R-free (%) 24.3
D
Tyr132
Asp135
Tyr175
Lys206
Lys241
Glu190
COOH
HO
40
Resolution (Å) 2.28
R-factor (%) 20.2
R-free (%) 25.15
E
Tyr132
Asn86
Asp135
Lys206
Lys241
Glu190
COOH
HO
OH
35
Resolution (Å) 2.27
R-factor (%) 23.5
R-free (%) 28.8
F
Tyr132
Asp135
Lys206
Lys241
Glu190
COOH
HO
42
Resolution (Å) 2.15
R-factor (%) 20.0
R-free (%) 24.0
G
Tyr132
Asp135
Tyr177
Lys241
Lys206
His188
His276
Glu190
H
Tyr132
Phe185
Lys206
Lys241
Trp208
His188
His276
Asn198
Glu190
I
Tyr132
Lys206
Lys241
Glu190
J
K
Asn86
3.1
Tyr132
Asp135
2.8
Lys241
2.9
Tyr177
2.6
2.9
2.6
2.9
2.8
2.8
His188
Lys206
His276
Glu190
L
Phe185
Lys241
Tyr177
His188
Asn198
DMSO
Ser196

The acyl moieties of these inhibitors follow the peptide binding pocket and mostly occupy the area in which Ser10, Thr11 and Gly12 of the Histone H3 substrate bind (**Figure 7**).[20] For example, the hydroxyl moiety of the 4-hydroxylbenzoic-acid derived inhibitor **38** occupies the region of the active site where the carbonyl moiety of Gly12 is positioned in the crystal structure with the substrate. This allows the hydroxyl group to form a hydrogen bond with Asn86 (~2.9 Å). A similar interaction is observed between Asn86 and the oxygen in the oxazole ring of **39** (~3.0 Å) (**Figure 6**). The **39** structure has the most defined density for the compound, which may be due to the unique inward position of loop 309-311 in chain A, that restricts the position of the flexible loop near the active site. Only one structure – that of **43** - was obtained for phenylacetic acid amide derivatives. The poor electron density for the acyl moiety in this compound suggests conformational flexibility and a possibility that this group may occupy multiple position in the binding pocket, a possibility that we favor over compound hydrolysis in the solution, given the stability in solution of a model acylated derivative (**Figure 8**). In its most well defined position, the acyl group is positioned in the space generally occupied by Thr11 of the H3 substrate, with the oxygen atom of the methoxy substituent forming a hydrogen bond with Tyr175 (~3.0 Å). In the complex with the histone substrate, this Tyr residue engages the carbonyl oxygen of Lys 9.

Figure 7: Hybrid Derivative Compared With Substrate.

The crystal pose of **44** (magenta) in the KDM4A active with 2Fo-Fc density contoured at 1σ compare to the published histone H3 peptide and 2-oxoglutarate (green, pdbID 2OQ6).

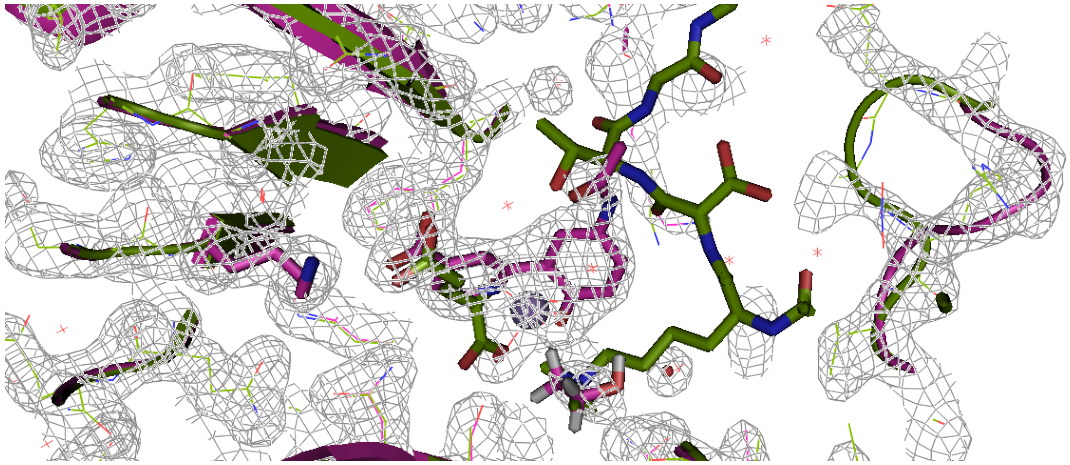

Figure 8: Compound stability test.

UPLC analysis shows the stability of **44** in solution over the course of 1 week.

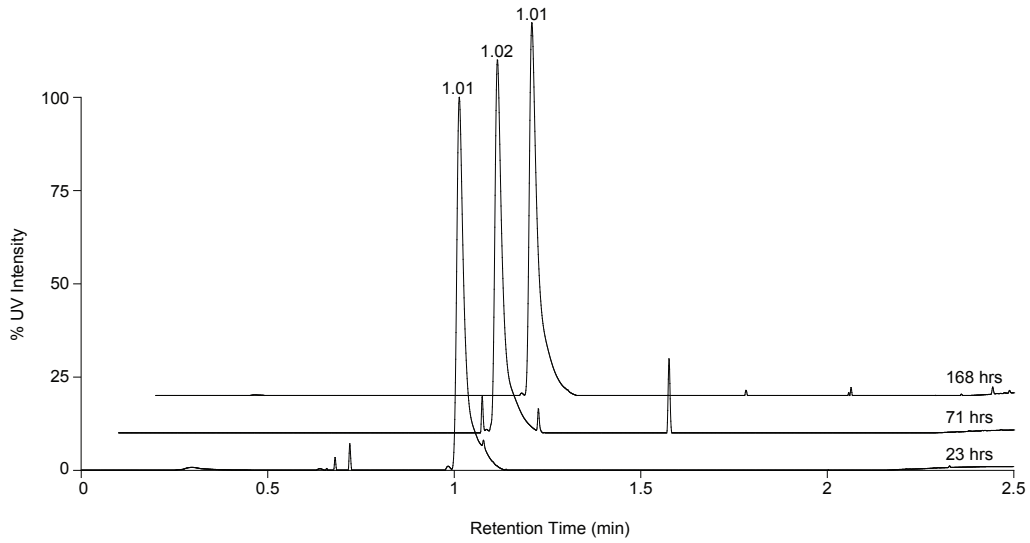

X. Discussion

Two key observations emerge from this study. First, against a soluble enzyme with little ligand precedence, a structure-based docking screen of a 600,000 fragment library efficiently revealed new inhibitors. Due to the sensitivity of the FRET assay, inhibition rates in the millimolar range could be reliably measured for the KDM4C enzyme, and all the fragments identified from docking studies inhibited the enzyme. More conservatively, if one only counts fragments with IC_{50} values better than 200 μM and LE values of 0.3 or better, the hit rate of our screen is 50%. Whereas structure-based docking has been shown to be effective in fragment prioritization, this was often against model enzymes, like β-lactamase [103,104] for which there was substantial ligand precedence; this is much less true for KDM4C, a target of active biological interest with little ligand precedence. This supports the pragmatism of docking a large library of fragments for new lead discovery. Second, and more ambitiously, this study represents the first use of docking poses to guide a fragment-fusing and synthetic elaboration strategy, one born out by the affinity maturation of the early compounds and the subsequent crystallography that is consistent with the docking predictions.

Both fragment-based and structure-based docking screens are often prosecuted against enzymes for which ligand precedence is low, and are considered challenging, or for which novel chemotypes are desired. One way they do so is by interrogating libraries of available molecules that contain many more molecules than those accessible to most empirical screens. This is especially true in fragment-based screening, where empirical libraries are rarely much larger than 50,000 molecules, but over 600,000 are available commercially and are readily docked. Naturally, this is only interesting if docking can

pragmatically prioritize among such a large space to discover new and potent fragments. The high hit rates observed here, and the ability to discover novel compounds even when compared to running full HTS screens is astonishing, for example based on an ECFP4-based Tanimoto coefficient of similarity fragment **6** is the most novel compound that we discovered in this screen with a score of 0.24 (fragments **2-8** scored between 0.24-0.63 to any compound described in ChEMBL, both literature based molecules for KDM4A/C and Pubchem HTS Assay AID2123 deposited for KDM4A, fragment **3** was least novel and resembled compound CHEMBL1443943). Good ligand efficiencies of compounds **2-8**, (LE = 0.3 - 0.45) further support the pragmatism of fragment docking against these novel docking targets.

Perhaps a greater challenge than fragment discovery is fragment optimization, which has typically demanded a close integration of structure-determination, modeling, and synthesis. An innovation of this study is the use of docked geometries of two classes of orientations to guide the design of a fused family of molecules, uniting features of each. This strategy was ambitious for several reasons. Fragment joining is often considered more difficult than fragment elaboration, though joining was the first strategy for optimization proposed[105] and has been successfully practiced.[106,107]In instances where this approach was successful, it has been guided by experimental binding geometries, either from NMR or from crystallography, not by docking poses. The success of the strategy here—buttressed by the two-log orders of affinity gained by the fused molecules, and the correspondence of the docking predictions to the subsequent crystallographic results—support the use of docking not only to prioritize initial hits for testing, but also to guide their optimization. This is also supported by earlier studies that suggest that docked

fragments can have high-fidelity to experimental structures[103,108-110]and that docking can prioritize among multiple binding modes sometimes suggested by those experimental structures.[104]

Important caveats bear consideration. Most importantly, we do not suggest that docking can replace the cycles of structure-determination and synthesis that are widely practiced in the field for fragment discovery and optimization—indeed, this study itself uses such cycles. We used docking to guide fusing and optimization because we were unable to determine the co-complex structures of the initial salicylate fragment hits, which bind in the 50 to 200 μM range. Thus, we do not advocate docking as a first strategy to guide fragment fusing and optimization. However, when determining initial fragment structures is difficult, this study suggests that considering docking as a tool for optimization is a viable option.

In summary, this study has revealed how discovery of the novel mid-micromolar 5-aminosalicylates series of inhibitors has been used for fragment linking to yield a hybrid scaffold. Optimization of this new scaffold has lead to nanomolar hybrid inhibitors of the KDM4 family of epigenetic erasers. A detailed analysis of representative compounds revealed a competitive binding mode with respect to α-KG that is supported by crystal structures (**Figure 6**), with K_i values of 43 nM for **35** and 0.68 μM for **42** (**Figure 4A,B**, **Table 6**). Interestingly, addition of an acyl moiety to the hybrid scaffold both increases potency against the KDM4 demethylase family and selectivity versus the asparagine hydroxylase FIH (**Figure 5B, Table 7**). Selectivity versus FIH is especially important as this hydroxylase is critical for the hypoxic response, and controls a large downstream transcriptional network. In addition, substantial selectivity is achieved

against the H3K36 demethylase KDM2A and the H3K27 demethylase KDM6B. Selectivity of our molecules against the KDM5 and KDM3 subfamilies remains limited. This study supports the pragmatism of docking screens for chemotype identification and elaboration in fragment based discovery for an epigenetic "eraser" target. Our work sets the stage for further elaboration of these molecules to improve their selectivity with the ultimate goal of using them as potent and selective chemical probes of KDM4 family demethylase function in physiology and disease.

XI. Materials and Methods

Cloning of KDM4C and other enzymes:

FIH:

The full-length *fih* gene was PCR amplified from a pcDNA3 plasmid (gift from Denise Chan) and subcloned into a pBH4 expression plasmid containing an N-terminal His_6 tag (gift from Wendell Lim), using BamHI and NotI restriction sites. Fwd primer: 5'-gatcggatccgcggcgacagcggcggaggctgtggcctctggctct-3'. Rev primer: 5'-gatcggcggccgcctagttgtatcggcccttgatcattgt-3'. Correct insertion of the *fih* gene was confirmed by sequencing. The expression plasmid was transformed into Rosetta 2(DE3)pLysS Competent Cells (EMD Biosciences), and a single colony was used to inoculate a 50 mL overnight culture. This culture was used to inoculate six 1 L cultures, which were induced with 0.2 mM IPTG for 16 hrs at 18° C upon reaching an OD_{600} of 0.6. Cell pellets were collected by centrifugation and stored at -80° C. Thawed pellets were resuspended in lysis buffer (20 mM Tris-HCl pH 7.9, 300 mM NaCl, 0.5 mM pmsf, 5 ug/mL DNAse, 5 mM BME, 20 mM imidazole), and lysed by three passages through a microfluidizer. The cell lysate was clarified by centrifugation, and the supernatant was incubated for 1 hr at 4° C with 4 mL bed volume TALON Metal Affinity Resin (Clontech Laboratories). The resin was then washed with 30 mL of lysis buffer followed by elution with lysis buffer supplemented with 250 mM imidazole. Protein containing fractions were combined and loaded onto a Superdex S75 size-exclusion column, eluting with 20 mM Tris-HCl pH 7.9 and 300 mM NaCl. Protein containing fractions were analyzed by SDS-PAGE, and fractions judged to contain FIH with >95 % purity were combined, concentrated, aliquoted, and frozen in liquid nitrogen for storage at -80° C. Electrospray

ionization MS found a mass consistent with the desired construct (calculated: 42910 Da, observed: 42964 Da).

KDM4C:

KDM4C (amino acids 1-352) was PCR amplified from a pCR4-TOPO plasmid (open biosystems) and subcloned into a pBH4 expression plasmid containing an N-terminal His_6 tag (gift from Wendell Lim), using BamHI and NotI restriction sites. Fwd primer: 5'-agtcttggatccatggaggtggccgaggtggaaagtc-3'. Rev primer: 5'-agtcttgcggccgcctaggatgctggagtaggcttcgtgtgatcaatgg-3'. Correct insertion of the *KDM4C* gene was confirmed by sequencing. The expression plasmid was transformed into Rosetta 2(DE3)pLysS Competent Cells (EMD Biosciences), and a single colony was used to inoculate a 50 mL overnight culture. This culture was used to inoculate six 1 L cultures, which were induced with 0.2 mM IPTG for 16 hrs at 18° C upon reaching an OD_{600} of 0.6. Cell pellets were collected by centrifugation and stored at -80° C. Thawed pellets were resuspended in lysis buffer (50 mM HEPES pH 8, 500 mM NaCl, 0.5 mM pmsf, 0.1 mg/mL DNAse, 20 mM imidazole), and lysed by three passages through a microfluidizer. The cell lysate was clarified by centrifugation, and the supernatant was incubated for 1 hr at 4° C with 4.5 mL bed volume Ni-NTA Agarose (Quiagen). The resin was then washed with 60 mL of lysis buffer lacking PMSF and DNAse, followed by elution with elution buffer (50 mM HEPES pH 8, 50 mM NaCl, 250 mM imidazole). Protein containing fractions were combined and loaded onto a Superdex S75 size-exclusion column, eluting with 10 mM HEPES pH 8 and 500 mM NaCl. Protein containing fractions were analyzed by SDS-PAGE, and fractions judged to contain KDM4C with >95 % purity were combined, concentrated, aliquoted, and frozen in liquid nitrogen for storage at -80° C.

KDM5A:

KDM5A was expressed and purified as previously described. [9]

KDM2A, KDM5B, KDM6B, KDM3A, KDM4D:

These enzymes were expressed and purified as previously described.[111]

Docking and choosing molecules:

All 20 chains from the structures of KDM4A (PDB ID: 2GP5, 2GP3, 2OQ7, 2OQ6, 2Q8C, 2VD7, 2YBK, 2WWJ, 3NJY, 3PDQ) and KDM4C (PDB ID: 3PDQ) were superposed. The residues that orient towards the actives site were 100% conserved between KDM4A and KDM4C. Even though at first glance the active site loop encompassing residues Leu153 to Thr173 (Ile168 to Val171 pointing towards the active site) might look different, the sequence between KDM4A and KDM4C in this area is conserved. The loop however adopts different orientations and higher b-factors are observed in this area in some structures. Therefore for docking we considered the KDM4A and KDM4C structures to be identical and since structures 2VD7, 2YBK, 2WWJ, 3NJY, and 3PDQ were crystallized with inhibitors we favored those as possible receptors for docking. In the end 3PDQ chain B was chosen as the docking model as it had the best resolution among the 5 inhibitor-structures and the loop encompassing residues Leu153 to Thr173 was well defined.

The end 3PDQ chain B was prepared by replacing the Ni^{2+} metal in the active site to the catalytically relevant Fe(II) metal. Next, docking was calibrated by running docking studies with known inhibitors and looking at both enrichment and pose recapitulation. In the optimization the Fe(II) metal was reduced to a charge of +1.1, +1.2,

+1.3, and +1.4 and the extra charge from the Fe(II) was distributed to the chelating residues of His188, His276 and Glu190. The hydrogen placement was optimized to interact with known inhibitors. A good enrichment of logAUC of 20.28 was obtained with Fe(II) at a charge of 1.3, however only the charge on the two histidine residues, His188, His276, was increased by +0.1. A few spheres were manually trimmed that were away from the metal center. For certain runs Tyr132 had the charge distributed where the each charge polar atom is increased by 0.4, to mimic the active site conditions as it is bridged by Lys206 and Asn280 to create an environment to hydrogen bond to the carboxylic acid of the co-substrate, αKG. Ligand and receptor bin size of 0.4 and overlap of 0.1 was used.

Thermal shift assay*:*

To a 150-mL solution of 50 mM HEPES (pH 7.0), 50 μM NiCl2, 5 μM KDM4C (gift from Lindsey Pack), and 1:1000 dilution of SYPRO Orange was added 3 μL of ligand solution in DMSO (2 v/v % final concentration). The mixture was transferred to a 96-well qPCR tube plate well and loaded onto a Stratagene qPCR instrument (Ashrafi Lab, UCSF). The method was set to start temperature at 25 °C, 7 s/cycle, 3 s ramps, 1 °C/cycle, end temperature at 65 °C, and FRROX channel. After acquisition, the data was processed using GraphPad Prism for curve fitting.

Aggregation assays to test for non-specific inhibition:

Aggregation assays were performed as previously described.[112]

In vitro inhibition assays:

KDM4C Time-resolved FRET assay:

3-fold serial dilutions of compound stocks dissolved in DMSO were added to 5 uL of assay buffer (500mM HEPES pH 7.0, 0.01 v/v % tween-20, 0.01 m/v % BSA) supplemented with 10 uM ammonium iron (II) sulfate hexahydrate, 4 uM or 100 uM αKG, 900 nM Histone H3 (1-21) lysine 9 tri-methylated peptide with biotin tag (anaspec), and 200 uM ascorbic acid in a 384-well opaque white plate (Perkin Elmer). The reaction was started by adding 5 uL of 20 nM KDM4C (1-352) in assay buffer, then sealed and incubated 45 min at ambient temperature. The final concentration of DMSO is 2%. The reaction was quenched by addition of 10 uL of detection mix containing 2 nM europium-conjugated anti-H3K9(me2) antibody (Perkin Elmer), 100 nM Ulight-streptavadin conjugate (Perkin Elmer), 2 mM EDTA pH 8.0, and 1x LANCE detection buffer (Perkin Elmer) in water. The quenched reaction was covered and incubated for 1 hr in the dark, and then read in a SpectraMax M5e plate reader using TR-FRET mode with an excitation wavelength of 320 nm, emission wavelengths of 665 nm and 615 nM, 50 us delay, 500 us integration, and 100 reads per well. Signal was calculated as E_{665}/E_{615}. Values were plotted in GraphPad Prism and fit by non-linear regression to calculate IC_{50}'s.

FIH MALDI Assay:

47.5 uL reactions containing reaction buffer (50 mM Tris-HCl pH 7.5), enzyme, cofactors, additives, and 3-fold compound dilutions from DMSO stocks (1 % final DMSO concentration) are started by the addition of 2.5 uL 1 mM SMDESGLPQLTSYDCEVNAPIQGSRNLLQGEELLRALDQVN peptide substrate

(GenScript), and incubated at 37°C for 45 min. Final concentrations are: 1 mM dithiothreitol, 100 uM αKG, 20 uM ammonium iron (II) sulfate hexahydrate, 4 mM ascorbate, and 540 nM FIH. Reactions are quenched by addition of 0.1 % formic acid and 5 mM EDTA pH 8.0 (final concentrations), then de-salted by zip-tip, eluting in 3 uL of 50 % acetonitrile with 0.1 % formic acid. Elutions are then diluted 1:10 into 0.1 % formic acid in water, and then 1 uL is spotted on a MALDI target plate on top of 1 uL pre-dried 2,5 dihydroxybenzoic acid in a saturated solution of 0.1 % formic acid in water. Spots are allowed to dry and then analyzed using a PE-Biosystems Voyager Elite STR MALDI-TOF in refectron mode. Activity was calculated as the ratio of the area under the peak of product peptide to the sum of the areas under the reactant and product peptides. Values were plotted in GraphPad Prism and fit by non-linear regression to calculate IC_{50}'s.

KDM4C MALDI Assay:

Assay performed as for FIH, with reaction consisting of: reaction buffer (20 mM HEPES pH 7.9, 50 mM NaCl), 100 uM αKG, 50 uM ammonium iron (II) sulfate hexahydrate, 500 uM ascorbate, 1 uM KDM4C, and 3-fold compound dilution series in DMSO (1 % final DMSO concentration). Reactions are started by the addition of 2.5 uL 2 mM peptide substrate ARTKQTARK(me3)STGGKA, with a final reaction volume of 50 uL. Reactions are incubated at ambient temperature for 45 min prior to quenching, de-salting, and analysis.

RBP2 MALDI Assay:

Assay performed as for FIH, with reaction consisting of: reaction buffer (50 mM HEPES pH 7.5, 50 mM KCl), 100 uM αKG, 20 uM ammonium iron (II) sulfate hexahydrate, 500 uM ascorbate, 1 uM RBP2, and 3-fold compound dilution series in DMSO (1 % final

DMSO concentration). Reactions are started by the addition of 2.5 uL 2 mM peptide substrate ARTK(Me3)QTARKSTGGKAPRK, with a final reaction volume of 50 uL. Reactions are incubated at ambient temperature for 20 min prior to quenching, de-salting, and analysis.

AlphaScreen Assays:

These assays were performed as previously described.[111]

K_i Determination:

FDH-coupled assay for generation of Lineweaver-Burk plots: To a black 96-well round-bottom Microfluor 1 plate (Thermo Scientific) was added reaction buffer (10 mM HEPES pH 7.9, 50 mM NaCl, 0.01 v/v % Tween-20), enzymes, cofactors, additives, and 3-fold compound dilutions from DMSO stocks (1 v/v % final DMSO concentration), to a final volume of 90 μL. Each well was then mixed thoroughly by manual pipetting, followed by the immediate addition of 10 μL of ARK(Me3)STGGK peptide substrate. Typical final concentrations are: 50 μM ammonium iron (II) sulfate hexahydrate, 500 μM ascorbate, 2 mM NAD^+, 0.0252 U formaldehyde dehydrogenase (FDH) per reaction, 1 μM KDM4C(1-352), 50 μM peptide substrate, and variable concentration of α-KG (2.5 – 50 μM). The reaction was monitored by measuring the change in fluorescence intensity over time on a SpectraMax M5e plate reader with an excitation wavelength of 350 nm and emission wavelength of 460 nm.

Determination of Ki values: Ki values were determined by FDH-coupled assay under identical conditions to those described above, except that the inhibitor was incubated for 15 min in reaction mixture lacking the peptide and α−KG, and the enzyme

concentration was 500 nM. Following incubation, the reaction was initiated by addition of α−KG (10 – 100 μM) and peptide substrate.

Data Analysis:

The rate of the first two minutes of the reaction is calculated by a linear fit, normalized to the fluorescence intensity of 1μM NADH. Values are plotted in GraphPad Prism. The Morrison equation for tight-binding inhibition is used to globally fit data derived from testing inhibition in the presence of a range of concentration of αKG:[113]

$$v_i = v_{0-} \frac{v_0\left([E] + [I] + K_i^{app}\right) - v_0\sqrt{([E] + [I] + K_i^{app})^2 - 4[E][I]}}{2[E]}$$

With the form of K_i^{app} for competitive inhibitors:

$$K_i^{app} = K_i(1 + \frac{[S]}{K_m})$$

Synthesis:

General Synthetic Methods

All reagents and solvents were purchased as the highest available grade from Sigma-Aldrich and used without further purification, unless otherwise indicated. Reverse-phase high performance liquid chromatography (RP-HPLC) was performed with a Varian ProStar solvent delivery system equipped with a Phenomenex Luna 10 μm C18(2) 100 Å column. Separation was achieved using a gradient of acetonitrile or methanol in water with 0.1% TFA, at a flow rate of 15 mL/min. 1H and 13C NMR were recorded on a Varian Innova 400 MHz spectrometer. Mass spectrometry (ESI-MS) was performed using a Waters Acquity UPLC/ESI-TQD with a 2.1 x 50 mm Acquity UPLC BEH C18 column.

1

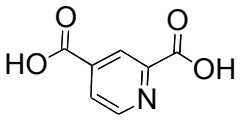

Purchased from Acros.

2

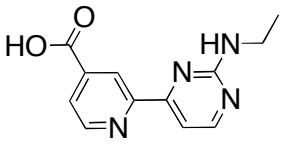

Purchased from Chembridge.

3a

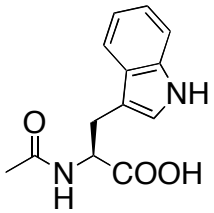

Molecular Weight: 246.26

Combine L-Tryptophan (6 mmol, 1.226 g), urea (10.3 mmol, 0.661 g), and 1.8 mL of a 3.3 N aqueous solution of NaOH in a 50 mL beaker and mix well. Place in a microwave oven (1100 W) along with a 500 mL beaker full of water, and microwave on high for 4 min. Remove from microwave and cool to 0 °C. Add 3 mL of a 2 N aqueous solution of HCl, isolate the precipitate by filtration, and wash the precipitate with water. Crude yield is 848.5 mg (3.43 mmol, 57 %). HPLC purification of 100 mg crude material (0.1 % TFA, acetonitrile/water gradient: 0-5 min, 20 % B; 5-30 min, 20-100 % B; 30-60 min,

100 % B) followed by freeze drying yielded 92.9 mg of solid (0.38 mmol, 53 %). LCMS $[M-H]^-$ *m/z* = 246.08. 1H NMR (400 MHz, DMSO-d6) δ 12.51 (s, 1H), 10.85 (s, 1H), 7.51 (d, J = 7.8 Hz, 1H), 7.33 (d, J = 8.1 Hz, 1H), 7.09 (d, J = 2.4 Hz, 1H), 7.06 (ddd, J = 8.1, 7.0, 1.2 Hz, 1H), 6.97 (ddd, J = 7.9, 7.1, 1.0 Hz, 1H), 6.11 (d, J = 8.1 Hz, 1H), 5.61 (s, 2H), 4.46 – 4.32 (m, 1H), 3.10 (dd, J = 14.6, 5.3 Hz, 1H), 3.01 (dd, J = 14.7, 7.0 Hz, 1H). 13C NMR (100 MHz, DMSO) δ 174.38, 158.16, 136.05, 127.43, 123.55, 120.86, 118.37, 118.33, 111.28, 109.69, 53.14, 27.87.

3b

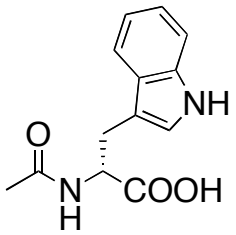

Molecular Weight: 246.26

Combine D-Tryptophan (3 mmol, 0.614 g), urea (4.99 mmol, 0.300 g), and 0.9 mL of a 3.3 N aqueous solution of NaOH in a 50 mL beaker and mix well. Place in a microwave oven (1100 W) along with a 500 mL beaker half-full of water, and microwave on high for 2 min. Remove from microwave and cool to 0 °C. Add 1.5 mL of a 2 N aqueous solution of HCl, isolate the precipitate by filtration, and wash the precipitate with water. Yield: 942.7 mg of solid (3.82 mmol, 128 %). LCMS $[M+H]^+$ *m/z* = 248.63. 1H NMR (400 MHz, DMSO-d6) δ 10.83 (s, 1H), 7.51 (d, J = 8.2 Hz, 1H), 7.32 (d, J = 8.1 Hz, 1H), 7.09 (d, J = 2.3 Hz, 1H), 7.04 (t, J = 7.0 Hz, 1H), 7.00 – 6.91 (m, 1H), 6.08 (d, J = 8.1 Hz, 1H), 5.58 (s, 2H), 5.39 (s, 1H), 4.31 (s, 1H), 3.10 (dd, J = 14.6, 5.5 Hz, 1H), 3.00 (dd, J = 14.5,

6.7 Hz, 1H). 13C NMR (126 MHz, DMSO) δ 174.41, 158.16, 136.06, 127.44, 123.57, 120.88, 118.39, 118.34, 111.29, 109.69, 53.14, 27.87.

4

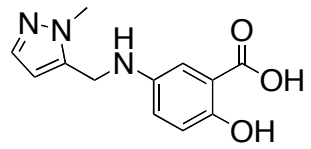

Molecular Weight: 247.25

Combine 5-aminosalicylate (1 mmol, 153 mg), 1-methyl-1H-pyrazole-5-carbaldehyde (0.5 mmol, 49.2 µL), and 10 mL EtOH in a flame-dried round bottom flask fitted with a reflux condenser, under an argon atmosphere. Stir 2 hrs at 100°C. Add sodium borohydride (1 mmol, 38 mg), stir 15 hrs at ambient temperature. Quench with 20 mL saturated NH_4Cl, then extract into 2 x 50 mL EtOAc. Combine the organic layers and wash with saturated NaCl, then dry over Na_2SO_4, filter, and concentrate under reduced pressure, yielding 218.8 mg crude product (0.88 mmol, 177 %). HPLC purification of 22.2 mg crude product (0.1 % TFA, acetonitrile/water gradient**:** 0-5 min, 15 % B; 5-25 min, 15-80 % B; 25-35 min, 80-100 % B; 35-50 min, 100 % B) followed by freeze drying yielded 12.3 mg of product (0.050 mmol, 98 %). LCMS $[M-H]^-$ *m/z* = 246.45. ^{1}H NMR (400 MHz, Acetonitrile-d3) δ 7.71 (s, 1H), 7.13 (d, J = 2.8 Hz, 1H), 6.98 (dd, J = 8.9, 2.8 Hz, 1H), 6.83 (d, J = 8.9 Hz, 1H), 6.42 (s, 1H), 4.38 (s, 2H), 3.95 (s, 3H). 13C NMR (126 MHz, DMSO) δ 171.77, 158.49, 158.19, 137.26, 117.70, 116.50, 114.20, 112.73, 106.01, 36.42, 36.32.

5

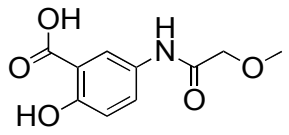

Purchased from Enamine, Ltd.

6

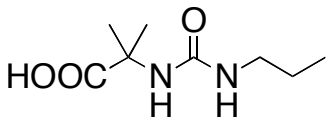

Molecular Weight: 188.22

Combine 2-Aminoisobutylic acid (2 mmol, 206 mg), 1-isocyanatopropane (2.1 mmol, 200 uL), and 3 mL 0.33 N NaOH in a 10 mL flask, and stir at ambient temperature 2 days. Remove precipitate by filtration, then acidify solution to pH 2.0 with 2 N HCl. Extract with EtOAc and concentrate under reduced pressure. HPLC purification (0.1 % TFA, acetonitrile/water gradient: 0-5 min, 20 % B; 5-30 min, 20-100 % B; 30-60 min, 100 % B) followed by freeze drying yielded 67 mg of solid (0.36 mmol, 18 %). LCMS $[M+H]^+$ *m/z* = 189.11. 1H NMR (400 MHz, DMSO-d6) δ 8.23 (s, 1H), 3.29 (t, J = 7.0 Hz, 2H), 1.50 (p, J = 7.2 Hz, 2H), 1.27 (s, 6H), 0.80 (t, J = 7.4 Hz, 3H). 13C NMR (100 MHz, DMSO) δ 177.56, 155.50, 57.63, 24.69, 20.92, 10.96.

7

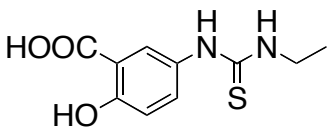

Molecular Weight: 240.28

Combine 5-Aminosalicylic acid (1 mmol, 153 mg), Ethyl isocyanate (1 mmol, 90 uL), and 2 mL acetonitrile in a 50 mL flask, and reflux 1.5 hrs. Cool to ambient temperature, add 20 mL DMF, and reflux an additional 75 min. Cool to ambient temperature and concentrate under reduced pressure. Suspend crude material in 20 mL EtOAc and extract with 10 mL saturated aqueous $NaHCO_3$. Wash with 2 x 20 mL EtOAc, and then re-extract from combined EtOAc with 2 x 10 mL saturated aqueous $NaHCO_3$. Acidify with 60 mL 2 N HCl, then extract with 3 x 20 mL EtOAc. Wash with 50 mL brine, dry over Na_2SO_4, filter, and concentrate under reduced pressure. HPLC purification (0.1 % TFA, acetonitrile/water gradient: 0-10 min, 20 % B; 10-25 min, 20-80 % B; 25-30 min, 80 % B; 35-60 min, 100 % B) followed by freeze drying yielded 156.3 mg of solid (0.65 mmol, 65 %). LCMS $[M-H]^-$ *m/z* = 239.44. 1H NMR (400 MHz, DMSO-d6) δ 11.12 (s, 1H), 9.25 (s, 1H), 7.77 – 7.53 (m, 1H), 7.45 (d, J = 8.8 Hz, 1H), 6.91 (d, J = 8.8 Hz, 1H), 3.45 (s, 2H), 1.09 (t, J = 7.1 Hz, 3H). 13C NMR (126 MHz, DMSO) δ 180.72, 171.59, 158.34, 132.83, 130.62, 126.02, 117.15, 112.50, 56.04, 18.58, 14.29.

8

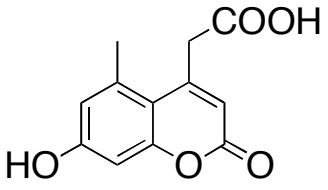

Molecular Weight: 234.20

Add citric acid (5.04 mmol, 968 mg) portion-wise to 1.4 mL H_2SO_4, and stir for 40 min at ambient temperature, then for 70 min at 70 °C. Cool to 0 °C and add 5-methylbenzene-1,3-diol (3.97 mmol, 492 mg) portion-wise over 15 min. Stir at 0 °C for 2 hrs, then pour

reaction onto 30 g ice. Collect filtrate, and wash with 4 x 5 mL water. Elute filtrate with 5 x 5 mL saturated aqueous $NaHCO_3$. Acidify filtrate with 30 mL 2 N HCl and extract with 2 x 30 mL EtOAc. Wash combined EtOAc with 2 x 50 mL brine, dry over Na_2SO_4, and concentrate under reduced pressure. Yield: 152.2 mg (0.65 mmol, 16 %). LCMS $[M-H]^-$ *m/z* = 233.50. 1H NMR (400 MHz, Chloroform-d) δ 6.94 (dd, J = 2.1, 1.2 Hz, 1H), 6.81 (s, 1H), 6.15 (t, J = 1.8 Hz, 1H), 4.03 (d, J = 1.7 Hz, 2H), 2.49 – 2.44 (m, 3H). 13C NMR (126 MHz, CDCl3) δ 216.50, 162.53, 159.93, 153.24, 149.60, 146.22, 144.27, 112.97, 112.28, 110.86, 102.29, 33.14, 22.50.

9

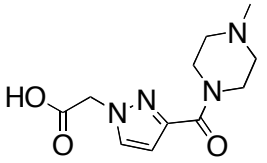

Molecular Weight: 252.27

Combine 1-(2-methoxy-2-oxoethyl)pyraole-3-carboxylic acid (Aurora) (0.16 mmol, 30 mg), HATU (0.187 mmol, 71 mg), DIPEA (0.172 mmol, 30 μL), *N*-methylpiperazine (0.27 mmol, 30 μL) and dry DMF (0.7 mL) in a 5 mL flask, and stir at ambient temperature overnight. Concentrate the reaction under reduced pressure, then partition between water (1 mL) and ethyl acetate (2 mL). Wash twice with ethyl acetate (2 mL). HPLC purification of the aqueous layer (0.1 % TFA, acetonitrile/water gradient: 0-5 min, 0 % B; 5-30 min, 0-30 % B; 30-60 min, 100 % B) followed by freeze drying yielded 19.0 mg of solid (0.070 mmol, 46 %). LCMS $[M+H]^+$ *m/z* = 253. 1H NMR (400 MHz, Deuterium Oxide) δ 7.80 (dd, J = 2.4, 0.9 Hz, 1H), 6.72 (dd, J = 2.3, 1.0 Hz, 1H), 5.14 (d, J = 0.7 Hz, 2H), 4.75 – 4.56 (m, 3H), 3.81 – 3.47 (m, 2H), 3.47 – 3.07 (m, 2H), 3.01 –

2.92 (m, 4H), 2.10 – 1.98 (m, 3H). 13C NMR (100 MHz, D2O) δ 172.34, 165.37, 163.68, 163.33, 145.52, 134.36, 119.76, 118.39, 115.49, 108.92, 53.77, 53.47, 44.93, 43.53, 40.24, 1.47.

10

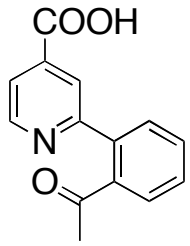

Molecular Weight: 241.24

Combine methyl 2-chloroisonicotinate (0.76 mmol, 130 mg), 2-acetylphenylboronic acid (1.39 mmol, 229 mg) (Alpha Aesar), 2.3 mL aqueous 2 M K_2CO_3, and 3 mL 1,4-dioxane in a 50 mL flask, and bubble with Ar for 10 min. Add $Pd(PPh_3)_4$ (0.073 mmol, 84 mg) and stir 12 hrs at reflux. Cool to ambient temperature, dilute with 30 mL EtOAc, and wash organic layer with 2 x 10 mL saturated aqueous $NaHCO_3$. Acidify the combined aqueous layers with 2 N HCl and extract with 2 x 15 mL n-BuOH, then concentrate under reduced pressure. HPLC purification (0.1 % TFA, acetonitrile/water gradient: 0-10 min, 20 % B; 10-25 min, 20-80 % B; 25-30 min, 80 % B; 35-60 min, 100 % B) followed by freeze drying yielded 73.8 mg of solid (0.31 mmol, 40 %). LCMS $[M-H]^-$ *m/z* = 240.50. 1H NMR (400 MHz, Deuterium Oxide) δ 9.19 (d, J = 6.4 Hz, 1H), 8.72 (s, 1H), 8.30 – 8.22 (m, 2H), 7.91 – 7.77 (m, 3H), 2.09 (d, J = 0.9 Hz, 3H). 13C NMR (126 MHz, D2O) δ 166.65, 151.03, 150.32, 143.29, 139.14, 134.42, 131.59, 128.22, 125.17, 123.88, 123.38, 120.17, 101.64, 25.74.

11

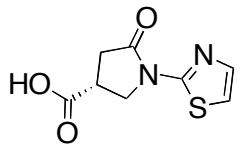

Purchased from Enamine.

12

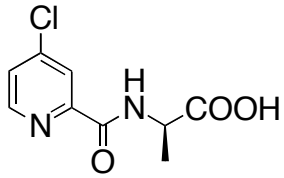

Molecular Weight: 228.63

Combine 4-chloropicolinic acid (0.52 mmol, 81 mg), L-alanine methyl ester HCl (0.58 mmol, 81 mg), 1-Ethyl-3-(3-dimethylaminopropyl)carbodiimide HCL (0.55 mmol, 105 mg), hydroxybenzotriazole (0.57 mmol, 77 mg), diisopropylethylamine (0.80 mmol, 140 uL), and 1 mL DMF in a 10 mL Schlenk flask and stir at ambient temperature 18 hrs. Concentrate under reduced pressure and then add 5 mL EtOAc. Wash with 2 x 5 mL 5 % aqueous citric acid, then 2 x 5 mL 5 % aqueous $NaHCO_3$, then 2 x 5 mL water, then 10 mL brine. Dry over Na_2SO_4 and concentrate under reduced pressure. Purify by flash chromatography eluting with EtOAc/hexanes (20/80) to give 72 mg crude intermediate. 44 mg of this material is dissolved in 1.2 mL 6 N HCl and 1.2 mL 1,4-dioxane in a 10 mL flask, and stirred at 60 °C for 9 hrs. Volatiles are removed under reduced pressure. HPLC purification (0.1 % TFA, acetonitrile/water gradient: 0-5 min, 25 % B; 5-30 min, 25-100 % B; 30-60 min, 100 % B) followed by freeze drying yields 21.7 mg of solid (0.095 mmol, 53 %). LCMS $[M-H]^-$ *m/z* = 227.43. 1H NMR (400 MHz, DMSO-d6) δ

8.90 (s, 1H), 8.66 (d, J = 5.3 Hz, 1H), 8.04 (s, 1H), 7.80 (dd, J = 5.3, 0.9 Hz, 1H), 4.60 – 4.40 (m, 1H), 1.43 (d, J = 7.0 Hz, 3H). 13C NMR (126 MHz, DMSO) δ 173.59, 162.25, 151.18, 150.17, 144.67, 126.71, 122.02, 47.88, 17.23.

13

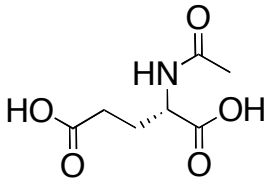

Purchased from Oakwood.

14

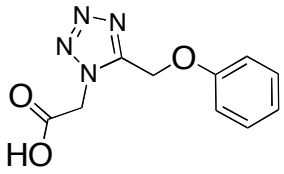

Purchased from Otava.

15

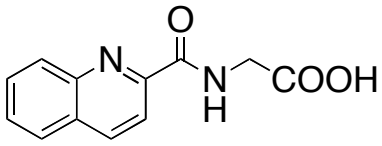

Molecular Weight: 230.22

Combine quinoline-2-carbonyl chloride (1.07 mmol, 205 mg), glycine methyl ester HCl (1.06 mmol, 134 mg), and 20 mL CH_2Cl_2 in a 100 mL schlenk flask and stir while adding Et_3N (24.4 mmol, 3.4 mL) dropwise over 5 min. Stir at ambient temperature 2 days, then

wash with 2 x 20 mL water, dry over Na_2SO_4, and concentrate under reduced pressure. Purify by flash chromatography, eluting in EtOAc/hexanes (25/75), to give 147 mg crude intermediate. 70 mg of this material is dissolved in 1.5 mL 6 N HCl and 1.5 mL 1,4-dioxane in a 10 mL flask, and stirred at 60 °C for 1 hr. Volatiles are removed under reduced pressure. HPLC purification (0.1 % TFA, acetonitrile/water gradient: 0-5 min, 30 % B; 5-30 min, 30-100 % B; 30-60 min, 100 % B) followed by freeze drying yields 54.4 mg of solid (0.24 mmol, 46 %). LCMS $[M+H]^+$ *m/z* = 231.57. 1H NMR (400 MHz, DMSO-d6) δ 12.74 (s, 1H), 9.13 (t, J = 6.1 Hz, 1H), 8.59 (dd, J = 8.5, 0.7 Hz, 1H), 8.19 – 8.08 (m, 3H), 7.89 (ddd, J = 8.4, 6.9, 1.5 Hz, 1H), 7.74 (ddd, J = 8.1, 6.9, 1.2 Hz, 1H), 4.05 (d, J = 6.1 Hz, 2H). 13C NMR (126 MHz, DMSO) δ 171.09, 164.20, 149.64, 146.02, 138.02, 130.68, 129.18, 128.92, 128.22, 128.18, 118.60, 41.23.

16

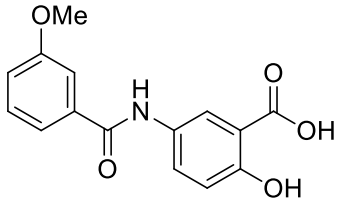

Molecular Weight: 287.27

Combine 3-methoxybenzoyl chloride (0.13 mmol, 22 mg), N-hydroxysuccinamide (0.26 mmol, 30 mg), diisopropylethylamine (0.5 mmol, 87 μL) and 1.5 mL acetonitrile and stir at ambient temperature for 30 min. Then add 5-aminosalicylate (0.13 mmol, 20 mg), and stir at ambient temperature for 5 hrs. Acidify reaction with 2 M HCl, extract with EtOAc, and concentrate under reduced pressure. HPLC purification (0.1 % TFA, acetonitrile/water gradient: 0-5 min, 20 % B; 5-25 min, 20-100 % B) followed by freeze drying yields 13.7 mg of white solid (0.048 mmol, 37 %). LCMS $[M+H]^+$ *m/z* = 288. ^1H

NMR (400 MHz, DMSO) δ 11.06 (s, 1H), 10.19 (s, 1H), 8.27 (d, *J* = 2.7 Hz, 1H), 7.88 (dd, *J* = 8.9, 2.7 Hz, 1H), 7.58 – 7.47 (m, 1H), 7.44 (t, *J* = 7.9 Hz, 1H), 7.15 (ddd, *J* = 8.2, 2.6, 0.9 Hz, 1H), 6.97 (d, *J* = 8.9 Hz, 1H), 4.15 (s, 1H), 3.84 (s, 1H). ^{13}C NMR (100 MHz, DMSO) δ 171.93, 165.14, 159.39, 157.61, 136.32, 130.97, 129.75, 128.91, 122.10, 119.98, 117.50, 117.26, 113.00, 112.59, 55.54.

17

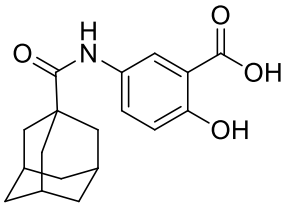

Molecular Weight: 315.36

Combine 1-adamantanecarbonyl chloride (0.13 mmol, 26 mg), N-hydroxysuccinamide (0.26 mmol, 30 mg), diisopropylethylamine (0.5 mmol, 87 μL) and 1.5 mL acetonitrile and stir at ambient temperature for 30 min. Then add 5-aminosalicylate (0.13 mmol, 20 mg), and stir at ambient temperature for 5 hrs. Acidify reaction with 2 M HCl, extract with EtOAc, and concentrate under reduced pressure. HPLC purification (0.1 % TFA, acetonitrile/water gradient: 0-5 min, 50 % B; 5-30 min, 50-100 % B) followed by freeze drying yielded 1.0 mg of white solid (0.0032 mmol, 2.5 %). LCMS $[M+H]^+$ *m/z* = 316. ^{1}H NMR (400 MHz, DMSO) δ 9.06 (s, 1H), 7.96 (d, *J* = 2.8 Hz, 1H), 7.68 (dd, *J* = 8.9, 2.8 Hz, 1H), 6.74 (d, *J* = 8.8 Hz, 1H), 2.02 (s, 2H), 1.91 (s, 3H), 1.70 (s, 3H). 13C NMR (126 MHz, MeOD) δ 179.46, 175.58, 163.17, 162.89, 159.87, 129.73, 129.20, 126.30, 125.92, 120.07, 119.41, 117.09, 116.95, 42.32, 40.12 (3C), 37.61 (3C), 29.76 (3C).

18

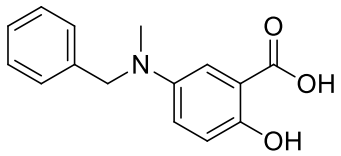

Molecular Weight: 257.28

Combine 0.25 mmol paraformaldehyde (0.25 mmol, 7.5 mg), DLSA001 (0.12 mmol, 29 mg), $NaCNBH_3$ (0.32 mmol, 20 mg), and 2 mL EtOH in a round bottom flask fitted with a reflux condenser. Heat to 100°C for 2 hrs. Cool to ambient temperature and acidify with 2 M HCl. HPLC purification (0.1 % TFA, acetonitrile/water gradient: 0-5 min, 10 % B; 5-30 min, 10-80 % B) followed by freeze drying yielded 11.9 mg of white solid (0.046 mmol, 39 %). LCMS $[M+H]^+$ *m/z* = 258. ^{1}H NMR (400 MHz, DMSO) δ 11.08 (s, 1H), 7.47 – 7.07 (m, 5H), 6.90 (d, *J* = 7.7 Hz, 1H), 4.55 (s, 1H), 3.01 (s, 2H). ^{13}C NMR (100 MHz, DMSO) δ 171.51, 158.57, 158.20, 128.47, 128.35, 127.63, 124.28, 117.95, 116.95, 114.05, 112.94, 58.28, 40.58.

19

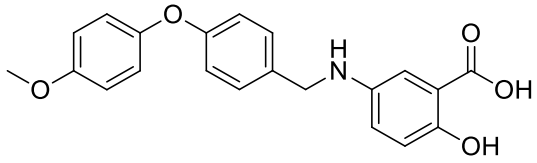

Molecular Weight: 365.38

Combine 4-(4-methoxyphenoxy)benzaldehyde (0.25 mmol, 57 mg), 5-aminosalicylate (0.12 mmol, 18 mg), $NaCNBH_3$ (0.32 mmol, 20 mg), and 2 mL EtOH in a round bottom flask fitted with a reflux condenser. Heat to 100°C for 2 hrs. Cool to ambient temperature and acidify with 2 M HCl. HPLC purification (0.1 % TFA, acetonitrile/water gradient: 0-5 min, 30 % B; 5-30 min, 30-100 % B) followed by freeze drying yielded 17.2 mg of

yellow solid (0.047 mmol, 23 %). LCMS $[M+H]^+$ *m/z* = 366. ^{1}H NMR (400 MHz, DMSO) δ 7.34 (dd, *J* = 8.4, 3.0 Hz, 1H), 7.17 (s, 1H), 7.04 (d, *J* = 8.7 Hz, 1H), 6.99 – 6.92 (m, 2H), 6.89 (dd, *J* = 8.6, 3.3 Hz, 1H), 6.81 (dd, *J* = 8.9, 3.3 Hz, 1H), 4.25 (s, 1H), 3.74 (d, *J* = 3.6 Hz, 2H). ^{13}C NMR (100 MHz, DMSO) δ 171.73, 157.23, 155.60, 154.70, 154.61, 149.48, 129.63, 123.87, 120.73, 120.58, 117.68, 117.26, 115.08, 112.80, 55.40, 48.45, 1.15.

20

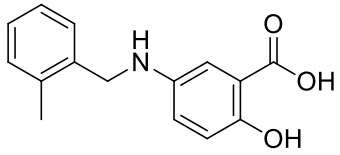

Molecular Weight: 257.28

Combine 2-methylbenzaldehyde (0.25 mmol, 30 mg), 5-aminosalicylate (0.12 mmol, 18 mg), $NaCNBH_3$ (0.32 mmol, 20 mg), and 2 mL EtOH in a round bottom flask fitted with a reflux condenser. Heat to 100°C for 2 hrs. Cool to ambient temperature and acidify with 2 M HCl. HPLC purification (0.1 % TFA, acetonitrile/water gradient: 0-5 min, 10 % B; 5-30 min, 10-80 % B) followed by freeze drying yielded 36.2 mg of white solid (0.14 mmol, 70 %). LCMS $[M+H]^+$ *m/z* = 258.28. ^{1}H NMR (400 MHz, DMSO) δ 7.34 – 7.27 (m, 1H), 7.20 – 7.11 (m, 4H), 7.03 (dd, *J* = 8.9, 2.7 Hz, 1H), 6.81 (d, *J* = 8.9 Hz, 1H), 4.23 (s, 2H), 2.31 (s, 3H). ^{13}C NMR (100 MHz, DMSO) δ 171.82, 154.37, 138.65, 136.27, 135.99, 130.11, 128.14, 127.22, 125.78, 123.47, 117.68, 113.95, 112.78, 46.82, 18.65.

21

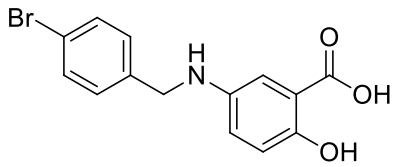

Molecular Weight: 322.15

Combine 5-aminosalicylate (0.2 mmol, 31 mg), 4-bromobenzaldehyde (0.2 mmol, 37 mg), and 2 mL EtOH in a round bottom flask fitted with a reflux condenser. Heat to 100°C for 1 hr. Then add sodium borohydride (0.4 mmol, 15 mg), and heat to 100°C for 3 hrs. Acidify reaction with 2 M HCl. HPLC purification (0.1 % TFA, acetonitrile/water gradient: 0-5 min, 10 % B; 5-20 min, 10-35 % B; 20-30 min, 35-75 % B) followed by freeze drying yielded 35.5 mg of orange solid (0.11 mmol, 55 %). LCMS $[M+H]^+$ *m/z* = 322.13, 324.11. 1H NMR (400 MHz, DMSO-d6) δ 10.50 (s, 1H), 7.51 (s, 1H), 7.49 (s, 1H), 7.32 (s, 1H), 7.29 (s, 1H), 6.92 (d, J = 2.9 Hz, 1H), 6.85 (dd, J = 8.8, 3.0 Hz, 1H), 6.72 (d, J = 8.9 Hz, 1H), 4.19 (s, 2H). 13C NMR (126 MHz, DMSO) δ 172.01, 152.84, 140.99, 139.69, 131.14 (2C), 129.42 (2C), 121.88, 119.57, 117.47, 112.48, 111.45, 46.51.

22

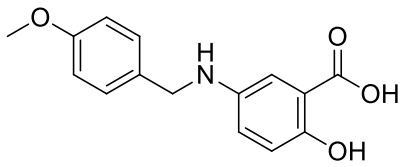

Molecular Weight: 273.28

Combine 4-methoxybenzaldehyde (0.25 mmol, 30.4 µL), 5-aminosalicylate (0.12 mmol, 18 mg), $NaCNBH_3$ (0.32 mmol, 20 mg), and 2 mL EtOH in a round bottom flask fitted with a reflux condenser. Heat to 100°C for 2 hrs. Cool to ambient temperature and acidify with 2 M HCl. HPLC purification (0.1 % TFA, acetonitrile/water gradient: 0-5 min, 10 %

B; 5-30 min, 10-80 % B) followed by freeze drying yielded 46.9 mg of white solid (0.17 mmol, 86 %). LCMS $[M-H]^-$ *m/z* = 272.19. ^{1}H NMR (400 MHz, DMSO) δ 7.56 (s, 1H), 7.32 (dd, *J* = 8.5, 3.4 Hz, 3H), 7.00 – 6.87 (m, 3H), 4.36 (d, *J* = 3.0 Hz, 2H), 3.73 (d, *J* = 3.8 Hz, 3H). ^{13}C NMR (100 MHz, DMSO) δ 171.27, 159.30, 158.94, 158.13, 130.81, 127.47, 126.25, 120.60, 118.17, 113.91, 113.47, 55.15, 51.59.

23

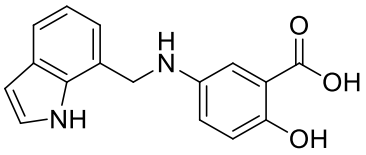

Molecular Weight: 282.29

Combine 5-aminosalicylate (0.2 mmol, 31 mg), 1*H*-indole-7-carbaldehyde (0.2 mmol, 29 mg) (Acros), and 2 mL EtOH in a round bottom flask fitted with a reflux condenser. Heat to 100°C for 1 hr. Then add sodium borohydride (0.4 mmol, 15 mg), and heat to 100°C for 3 hrs. Acidify reaction with 2 M HCl. HPLC purification (0.1 % TFA, acetonitrile/water gradient: 0-5 min, 10 % B; 5-30 min, 10-80 % B) followed by freeze drying yielded 14.3 mg of yellow solid (0.051 mmol, 25 %). LCMS $[M-H]^-$ *m/z* = 281.21. ^{1}H NMR (400 MHz, DMSO) δ 11.24 (s, 1H), 7.51 (d, *J* = 7.8 Hz, 2H), 7.42 (s, 1H), 7.41 – 7.38 (m, 2H), 7.23 (d, *J* = 7.9 Hz, 2H), 7.16 (d, *J* = 7.0 Hz, 2H), 6.99 (t, *J* = 7.6 Hz, 2H), 6.88 (d, *J* = 8.7 Hz, 1H), 6.48 (dd, *J* = 2.9, 1.5 Hz, 1H), 4.61 (s, *J* = 14.2 Hz, 3H). ^{13}C NMR (100 MHz, DMSO) δ 171.34, 161.95, 134.24, 127.82, 125.18, 120.95, 120.70, 119.60, 118.60, 117.56, 117.16, 114.25, 112.72, 101.34, 93.76, 60.55.

24

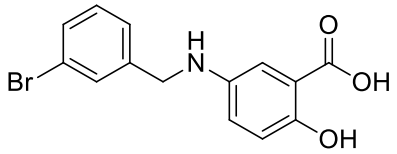

Molecular Weight: 322.15

Combine 5-aminosalicylate (0.2 mmol, 31 mg), 3-bromobenzaldehyde (0.2 mmol, 23.3 μL), and 2 mL EtOH in a round bottom flask fitted with a reflux condenser. Heat to 100°C for 1 hr. Then add sodium borohydride (0.4 mmol, 15 mg), and heat to 100°C for 3 hrs. Acidify reaction with 2 M HCl. HPLC purification (0.1 % TFA, acetonitrile/water gradient: 0-5 min, 10 % B; 5-20 min, 10-35 % B; 20-30 min, 35-75 % B) followed by freeze drying yielded 23.7 mg of orange solid (0.074 mmol, 37 %). LCMS $[M+H]^+$ *m/z* = 322.09, 324.08. 1H NMR (400 MHz, DMSO-d6) δ 7.66 (s,1H), 7.50 (d, J = 7.9 Hz, 1H), 7.46 – 7.39 (m, 1H), 7.39 – 7.22 (m, 2H), 7.05 (d, J = 27.5 Hz, 1H), 6.76 (dd, J = 8.6, 3.2 Hz, 1H), 4.37 (s, 2H). 13C NMR (126 MHz, DMSO) δ 171.87, 130.60, 130.51, 130.12, 129.74, 126.59, 121.74, 121.72, 117.61, 112.62, 47.17.

25

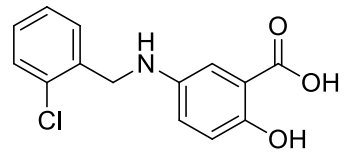

Molecular Weight: 277.70

Combine 5-aminosalicylate (0.2 mmol, 31 mg), 2-chlorobenzaldehyde (0.2 mmol, 22.5 μL), and 2 mL EtOH in a round bottom flask fitted with a reflux condenser. Heat to 100°C for 1 hr. Then add sodium borohydride (0.4 mmol, 15 mg), and heat to 100°C for 3 hrs. Acidify reaction with 2 M HCl. HPLC purification (0.1 % TFA, acetonitrile/water

gradient: 0-5 min, 10 % B; 5-10 min, 10-35 % B; 10-30 min, 35-80 % B) followed by freeze drying yielded 39.2 mg of white solid (0.14 mmol, 70 %). LCMS $[M+H]^+$ *m/z* = 276.13. 1H NMR (400 MHz, DMSO-d6) δ 10.53 (s, 1H), 7.48 – 7.38 (m, 2H), 7.34 – 7.25 (m, 2H), 6.95 (d, J = 2.9 Hz, 1H), 6.88 (dd, J = 8.8, 3.0 Hz, 1H), 6.76 (dd, J = 8.8, 0.4 Hz, 1H), 4.30 (s, 2H). 13C NMR (126 MHz, DMSO) δ 171.90, 166.70, 153.17, 140.48, 136.67, 132.60, 132.37, 131.57, 130.80, 130.62, 129.23, 129.01, 128.58, 127.24, 127.18, 122.01, 117.62, 112.53, 111.61, 45.06.

26

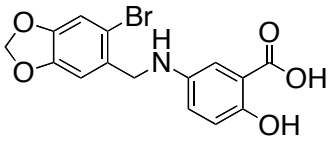

Molecular Weight: 366.16

Combine 5-aminosalicylate (0.065 mmol, 10 mg), 6-bromo-1,3-benzodioxole-5-carboxaldehyde (0.13 mmol, 30 mg), 1 mL EtOH and 100 uL acetic acid in a round bottom flask fitted with a reflux condenser. Stir 2 hrs at 100°C. Add sodium borohydride (0.26 mmol, 10 mg), stir 30 min at 100°C. HPLC purification (0.1 % TFA, methanol/water gradient**:** 0-8 min, 5 % B; 8-22 min, 5-75 % B; 22-34 min, 100 % B) followed by freeze drying yielded 9.7 mg of product (0.027 mmol, 41 %). LCMS $[M-H]^-$ *m/z* = 364.00, 365.95. 1H NMR (400 MHz, DMSO-d6) δ 10.53 (s, 1H), 7.21 (d, J = 0.5 Hz, 1H), 6.94 (d, J = 4.6 Hz, 2H), 6.85 (d, J = 2.9 Hz, 1H), 6.77 (s, 1H), 6.03 (s, 2H), 4.15 (s, 2H). 13C NMR (126 MHz, DMSO) δ 171.92, 153.26, 147.30, 147.17, 131.49, 122.08, 117.64, 112.83, 112.58, 112.34, 112.31, 108.67, 101.97, 101.87, 47.50.

27

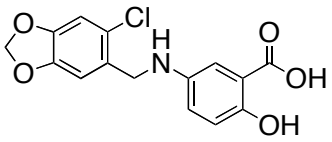

Molecular Weight: 321.71

Combine 5-aminosalicylate (0.065 mmol, 10 mg), 6-chloro-1,3-benzodioxole-5-carboxaldehyde (0.13 mmol, 24 mg), 1 mL EtOH and 100 uL acetic acid in a round bottom flask fitted with a reflux condenser. Stir 2 hrs at 100°C. Add sodium borohydride (0.26 mmol, 10 mg), stir 30 min at 100°C. HPLC purification (0.1 % TFA, methanol/water gradient**:** 0-8 min, 5 % B; 8-22 min, 5-75 % B; 22-34 min, 100 % B) followed by freeze drying yielded 10.1 mg of product (0.031 mmol, 48 %). LCMS $[M-H]^-$ *m/z* = 320.08. 1H NMR (400 MHz, DMSO-d6) δ 10.55 (s, 1H), 7.07 (s, 1H), 6.96 (d, J = 2.9 Hz, 1H), 6.94 (s, 1H), 6.87 (dd, J = 8.8, 2.9 Hz, 1H), 6.76 (d, J = 8.9 Hz, 1H), 6.03 (d, J = 0.4 Hz, 2H), 4.19 (s, 2H). 13C NMR (126 MHz, DMSO) δ 171.89, 153.31, 146.96, 146.68, 140.12, 129.90, 123.83, 122.18, 117.63, 112.58, 111.92, 109.54, 108.46, 101.90, 44.97.

28

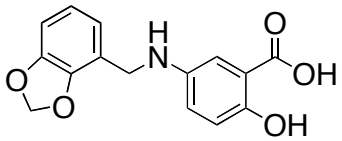

Molecular Weight: 287.27

Combine 5-aminosalicylate (0.4 mmol, 61 mg), 2,3-(Methylenedioxy)benzaldehyde (0.4 mmol, 45.8 µL) (Combi-Blocks), and 4 mL EtOH in a round bottom flask fitted with a reflux condenser. Stir 30 min at 100°C. Add sodium borohydride (0.8 mol, 30 mg), stir

30 min at 100°C. HPLC purification (0.1 % TFA, acetonitrile/water gradient**:** 0-10 min, 20 % B; 10-40 min, 20-100 % B; 40-50 min, 100 % B) followed by freeze drying yielded 85.3 mg of product (0.30 mmol, 74 %). LCMS $[M-H]^-$ *m/z* = 286.15. 1H NMR (400 MHz, DMSO-d6) δ 7.31 (s, 1H), 7.12 – 7.05 (m, 1H), 6.98 – 6.73 (m, 5H), 6.01 (d, J = 2.4 Hz, 2H), 4.31 (s, 2H), 4.18 (s, 1H). 13C NMR (126 MHz, DMSO) δ 171.94, 153.49, 146.72, 145.05, 122.53, 121.48, 121.40, 121.24, 120.86, 117.55, 112.55, 107.28, 107.09, 100.75, 57.21, 41.81

29

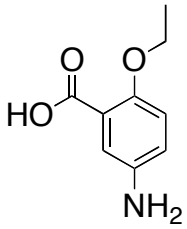

Purchased from ChemBridge.

30

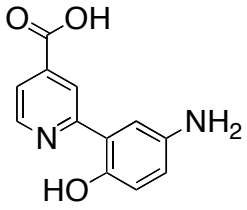

Molecular Weight: 230.22

Combine methyl 2-bromoisonicotinate (1.28 mmol, 277 mg) (Combi-Blocks), 2-methyl-5-nitrophenylboronic acid pinacol ester (0.85 mmol, 237 mg) (Frontier Scientific), Cs_2CO_3 (1.63 g), CombiPhos-Pd6 (0.1 mmol, 50 mg) (CombiPhos Catalysts), and 10 mL

DMF in a 15 mL pressure vial. Stir 20 hrs at 100° C. Dilute in 75 mL water, acidify to pH 2 with 2N HCl, then extract three times with 50 mL EtOAc. Wash the combined organic phase with 5 % citric acid, then with 50 mL saturated NaCl with 1 mL added 2N HCl, then concentrate under reduced pressure. Transfer the crude reaction to a new 15 mL pressure vial, and add 6 mL 48 % aqueous HBr (Sigma) and NaI (4 mmol, 600 mg). Stir at 100° C for 4 days. Dilute in 50 mL water, wash once with 50 mL EtOAc, and then concentrate the aqueous fraction under reduced pressure. HPLC purification (0.1 % TFA, acetonitrile/water gradient**:** 0-10 min, 10 % B; 10-89 min, 10-40 % B; 89-90 min, 40-100 % B; 90-100 min, 100 % B) followed by freeze drying yielded 38 mg of product (0.165 mmol, 19 %). LCMS $[M+H]^+$ *m/z* = 231.54. ^{1}H NMR (400 MHz, DMSO) δ 8.85 (d, J = 5.1 Hz, 1H), 8.52 (d, J = 0.8 Hz, 1H), 8.07 (d, J = 2.1 Hz, 1H), 7.92 – 7.79 (m, 1H), 7.38 – 7.27 (m, 1H), 7.10 (dd, J = 8.7, 0.8 Hz, 1H). 13C NMR (126 MHz, DMSO) δ 165.89, 157.98, 156.42, 156.02, 148.73, 139.77, 125.18, 121.54, 120.85, 120.32, 118.69.

31

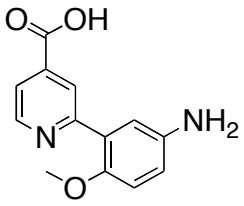

Molecular Weight: 244.25

This compound is purified as a side-product of the reaction to produce SPSA011. LCMS $[M+H]^+$ *m/z* = 245.19. 1H NMR (400 MHz, DMSO-d6) δ 8.86 (dd, J = 5.0, 0.9 Hz, 1H), 8.38 (dd, J = 1.6, 0.9 Hz, 1H), 7.78 (dd, J = 5.0, 1.6 Hz, 1H), 7.76 (d, J = 2.7 Hz, 1H), 7.31 (dd, J = 8.8, 2.7 Hz, 1H), 7.25 (d, J = 8.9 Hz, 1H), 3.88 (s, 3H). 13C NMR (126

MHz, DMSO) δ 166.26, 154.91, 154.68, 150.42, 138.32, 127.88, 123.64, 123.30, 123.17, 121.42, 113.50, 56.29

32

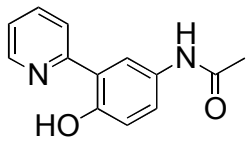

Purchased from Sigma.

33

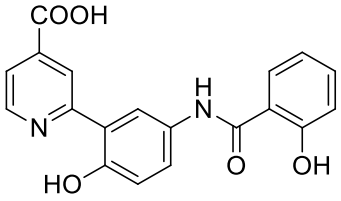

Molecular Weight: 350.32

To a glass vial, add 2-(Acetoxy)benzoyl chloride (0.071 mmol, 14 mg), N-hydroxysuccinimide (0.13 mmol, 15 mg), and 0.5 mL acetonitrile. Stir at ambient temperature for 1 hr. Add SPSA011 (0.013 mmol, 3 mg) in 0.5 mL 1:1:1 water/acetonitrile/methanol, and stir at ambient temperature for 16 hrs. Intermediate HPLC purification (0.1 % TFA, MeOH/water gradient: 0-5 min, 15 % B; 5-10 min, 15-40 % B; 10-35 min, 40-80 % B) followed by concentration at reduced pressure. The concentrate was transferred to a sealed pressure vial with 0.5 mL 2 M NaOH and heated to 100 °C for 1 hr. The reaction was quenched with 2 M HCl. Final HPLC purification (0.1 % TFA, MeOH/water gradient: 0-5 min, 15 % B; 5-10 min, 15-50 % B; 10-35 min, 50-100 % B) followed by freeze drying yielded 0.9 mg of yellow solid (0.003 mmol, 20

%). LCMS $[M+H]^+$ *m/z* = 351.26. ^{1}H NMR (400 MHz, DMSO-d_6) δ 10.35 (s, 1H), 8.84 (d, *J* = 5.4 Hz, 1H), 8.50 (s, 1H), 8.37 (s, 1H), 8.00 (d, *J* = 7.9 Hz, 1H), 7.84 (d, *J* = 5.3 Hz, 1H), 7.72 (dd, *J* = 8.2, 1.5 Hz, 1H), 7.44 (s, 1H), 7.00 (s, 1H), 6.99 (d, *J* = 2.8 Hz, 1H), 6.97 (s, 1H). 13C NMR (126 MHz, D2O) δ 175.16, 170.36, 169.84, 169.60, 164.62, 164.44, 164.34, 164.06, 163.78, 160.31, 150.41, 146.27, 135.22, 131.05, 129.58, 126.58, 126.28, 125.72, 125.39, 123.56, 122.67, 121.86, 121.43, 120.23, 119.11, 116.78, 115.53, 114.46.

34

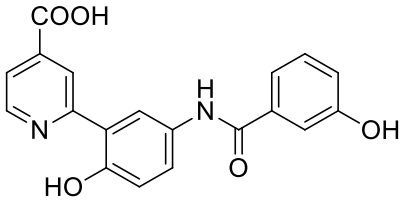

Molecular Weight: 350.32

To a glass vial, add 3-(Acetoxy)benzoyl chloride (0.071 mmol, 14 mg), N-hydroxysuccinimide (0.13 mmol, 15 mg), and 0.5 mL acetonitrile. Stir at ambient temperature for 1 hr. Add SPSA011 (0.013 mmol, 3 mg) in 0.5 mL 1:1:1 water/acetonitrile/methanol, and stir at ambient temperature for 16 hrs. The reaction mixture was then transferred to a sealed pressure vial with 0.5 mL 2 M NaOH and heated to 100 °C for 1 hr. The reaction was quenched with 2 M HCl. HPLC purification (0.1 % TFA, MeOH/water gradient: 0-5 min, 15 % B; 5-10 min, 15-50 % B; 10-35 min, 50-100 % B) followed by freeze drying yielded 1.9 mg of yellow solid (0.005 mmol, 32 %). LCMS $[M+H]^+$ *m/z* = 351.16. ^{1}H NMR (400 MHz, DMSO-d_6) δ 10.11 (s, 1H), 9.74 (s, 1H), 8.83 (dd, *J* = 5.3, 1.1 Hz, 1H), 8.45 (d, *J* = 16.9 Hz, 1H), 7.88 – 7.80 (m, 1H), 7.45 –

7.39 (m, 1H), 7.38 – 7.27 (m, 2H), 6.97 (ddt, *J* = 4.9, 2.6, 1.3 Hz, 2H), 6.95 (d, *J* = 1.2 Hz, 1H). 13C NMR (126 MHz, DMSO) δ 165.91, 165.18, 157.39, 154.72, 148.16, 140.09, 136.42, 131.28, 129.42, 124.47, 121.12, 119.26, 119.07, 118.78, 118.38, 118.04, 117.73, 114.44.

35

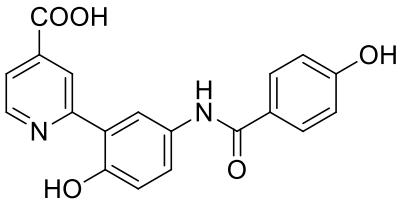

Molecular Weight: 350.32

To a glass vial, add 4-(Acetoxy)benzoyl chloride (0.071 mmol, 14 mg), and 0.5 mL acetonitrile. Stir at ambient temperature for 1 hr. Add SPSA011 (0.013 mmol, 3 mg) in 0.5 mL 1:1:1 water/acetonitrile/methanol, and stir at ambient temperature for 16 hrs. The reaction mixture was then transferred to a sealed pressure vial with 0.5 mL 2 M NaOH and heated to 100 °C for 1 hr. The reaction was quenched with 2 N HCl. HPLC purification (0.1 % TFA, MeOH/water gradient: 0-5 min, 15 % B; 5-10 min, 15-50 % B; 10-35 min, 50-100 % B) followed by freeze drying yielded 2.0 mg of yellow solid (0.006 mmol, 34 %). LCMS $[M+H]^+$ *m/z* = 351.18. 1H NMR (400 MHz, DMSO-d6) δ 12.99 (s, 1H), 10.08 (s, 1H), 9.95 (s, 1H), 8.83 (dd, J = 5.1, 0.8 Hz, 1H), 8.53 – 8.35 (m, 2H), 7.87 (d, J = 8.7 Hz, 2H), 7.85 – 7.80 (m, 2H), 6.95 (d, J = 8.8 Hz, 1H), 6.87 (d, J = 8.7 Hz, 2H). 13C NMR (126 MHz, DMSO) δ 165.91, 164.76, 160.44, 157.43, 154.54, 148.13, 140.07, 131.52, 129.53 (2C), 125.41, 124.47, 121.07, 119.21, 118.93, 118.70, 117.69, 114.90 (2C).

36

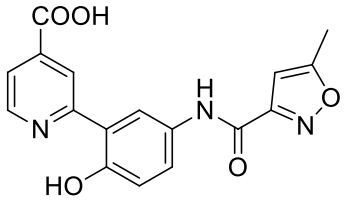

Molecular Weight: 339.30

To a glass vial, add 5-methylisoxazole-3-carboxyl chloride (0.071 mmol, 10 mg) (Oakwood Research), N-hydroxysuccinimide (0.13 mmol, 15 mg), and 0.5 mL acetonitrile. Stir at ambient temperature for 1 hr. Add SPSA011 (0.013 mmol, 3 mg) in 0.5 mL 1:1:1 water/acetonitrile/methanol, and stir at ambient temperature for 16 hrs. HPLC purification (0.1 % TFA, MeOH/water gradient: 0-10 min, 15 % B; 10-15 min, 15-40 % B; 15-35 min, 40-80 % B) followed by freeze drying yielded 1.5 mg of yellow solid (0.004 mmol, 40 %). LCMS $[M+H]^+$ *m/z* = 340.16. 1H NMR (400 MHz, DMSO-d6) δ 13.16 (s, 1H), 10.57 (s, 1H), 8.82 (d, J = 5.1 Hz, 1H), 8.49 (d, J = 2.5 Hz, 1H), 8.46 (s, 1H), 7.85 (d, J = 2.5 Hz, 1H), 7.85 – 7.81 (m, 2H), 6.97 (d, J = 8.8 Hz, 1H), 6.67 (d, J = 1.1 Hz, 1H), 2.54 (s, 3H). 13C NMR (126 MHz, DMSO) δ 171.42, 165.85, 159.30, 157.13, 157.04, 155.26, 147.96, 130.12, 124.37, 121.27, 119.29, 119.25, 118.83, 117.84, 101.60, 11.92.

37

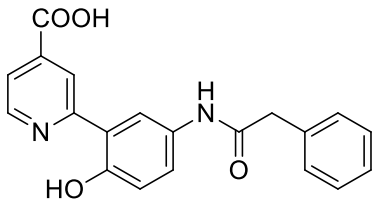

Molecular Weight: 348.35

To a glass vial, add phenylacetyl chloride (0.071 mmol, 9.4 μL) (Sigma), N-hydroxysuccinimide (0.13 mmol, 15 mg), and 0.5 mL acetonitrile. Stir at ambient temperature for 1 hr. Add SPSA011 (0.013 mmol, 3 mg) in 0.5 mL 1:1:1 water/acetonitrile/methanol, and stir at ambient temperature for 16 hrs. HPLC purification (0.1 % TFA, MeOH/water gradient: 0-10 min, 15 % B; 10-15 min, 15-50 % B; 15-35 min, 50-90 % B) followed by freeze drying yielded 0.3 mg of yellow solid (0.001 mmol, 8 %). LCMS $[M+H]^+$ *m/z* = 349.18. ^{1}H NMR (400 MHz, DMSO-d_6) δ 10.11 (s, 1H), 8.81 (d, *J* = 5.2 Hz, 1H), 8.40 (s, 1H), 8.28 (d, *J* = 2.7 Hz, 1H), 7.84 – 7.75 (m, 1H), 7.62 – 7.52 (m, 1H), 7.34 (d, *J* = 6.7 Hz, 3H), 7.21 (s, 1H), 7.08 (s, 1H), 7.00 – 6.86 (m, 2H), 3.62 (s, 2H). 13C NMR (126 MHz, DMSO) δ 168.74, 165.87, 157.17, 154.25, 148.27, 139.84, 136.09, 131.38, 129.12(2C), 128.32(2C), 126.53, 123.23, 121.08, 119.40, 119.05, 117.90, 117.85, 43.35.

38

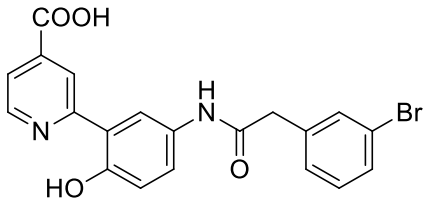

Molecular Weight: 427.25

To a glass vial, add 2-(3-bromophenyl)acetyl chloride (0.71 mmol, 17 mg), N-hydroxysuccinimide (0.13 mmol, 15 mg), and 0.5 mL acetonitrile. Stir at ambient temperature for 1 hr. Add SPSA011 (0.013 mmol, 3 mg) in 0.5 mL 1:1:1 water/acetonitrile/methanol, and stir at ambient temperature for 16 hrs. HPLC purification (0.1 % TFA, MeOH/water gradient: 0-10 min, 15 % B; 10-15 min, 15-50 % B; 15-35 min, 50-90 % B) followed by freeze drying yielded 0.6 mg of yellow solid

(0.001 mmol, 13 %). LCMS $[M+H]^+$ *m/z* = 427.09, 429.05. ^{1}H NMR (400 MHz, DMSO-d_6) δ 10.13 (d, *J* = 1.5 Hz, 1H), 8.81 (dd, *J* = 5.3, 1.3 Hz, 1H), 8.41 (s, 1H), 8.27 (s, 1H), 7.84 – 7.77 (m, 1H), 7.62 – 7.51 (m, 2H), 7.50 – 7.42 (m, 1H), 7.39 – 7.25 (m, 2H), 6.92 (dd, *J* = 8.8, 1.5 Hz, 1H), 3.65 (d, *J* = 1.6 Hz, 2H). 13C NMR (126 MHz, DMSO) δ 218.95, 168.15, 165.87, 157.12, 154.31, 148.27, 139.88, 138.74, 131.93, 131.21, 130.45, 129.43, 128.33, 123.23, 121.47, 121.09, 119.42, 117.97, 117.87, 42.61.

39

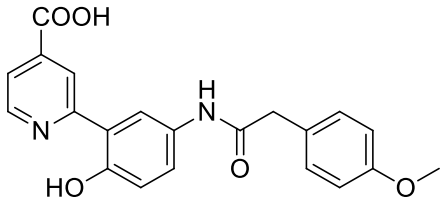

Molecular Weight: 378.38

To a glass vial, add 2-(4-methoxyphenyl)acetyl chloride (0.071 mmol, 10.9 µL), N-hydroxysuccinimide (0.13 mmol, 15 mg), and 0.5 mL acetonitrile. Stir at ambient temperature for 1 hr. Add SPSA011 (0.013 mmol, 3 mg) in 0.5 mL 1:1:1 water/acetonitrile/methanol, and stir at ambient temperature for 16 hrs. HPLC purification (0.1 % TFA, MeOH/water gradient: 0-10 min, 15 % B; 10-15 min, 15-50 % B; 15-35 min, 50-90 % B) followed by freeze drying yielded 1.1 mg of yellow solid (0.003 mmol, 29 %). LCMS $[M+H]^+$ *m/z* = 379. ^{1}H NMR (400 MHz, DMSO-d_6) δ 10.05 (s, 1H), 8.87 – 8.76 (m, 1H), 8.41 (s, 1H), 8.27 (s, 1H), 7.82 (d, *J* = 5.3 Hz, 1H), 7.58 (d, *J* = 8.5 Hz, 1H), 7.29 – 7.24 (m, 2H), 6.94 – 6.86 (m, 2H), 3.73 (d, *J* = 1.9 Hz, 3H), 3.54 (d, *J* = 1.3 Hz, 2H). 13C NMR (126 MHz, DMSO) δ 169.09, 165.87, 158.02, 157.17, 154.23, 148.23, 131.42, 130.09 (2C), 127.98, 123.20, 121.08, 119.35, 119.01, 117.83, 113.75 (2C), 55.04, 42.47.

40

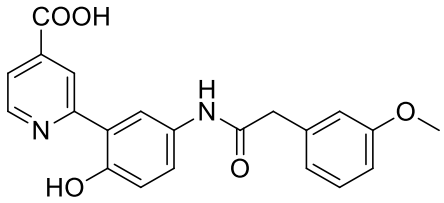

Molecular Weight: 378.38

To a glass vial, add 2-(3-methoxyphenyl)acetyl chloride (0.071 mmol, 11.1 μL), N-hydroxysuccinimide (0.13 mmol, 15 mg), and 0.5 mL acetonitrile. Stir at ambient temperature for 1 hr. Add SPSA011 (0.013 mmol, 3 mg) in 0.5 mL 1:1:1 water/acetonitrile/methanol, and stir at ambient temperature for 16 hrs. HPLC purification (0.1 % TFA, MeOH/water gradient: 0-5 min, 15 % B; 5-10 min, 15-50 % B; 10-35 min, 50-100 % B) followed by freeze drying yielded 1.6 mg of yellow solid (0.004 mmol, 25 %). LCMS $[M+H]^+$ *m/z* = 379.20. ^{1}H NMR (400 MHz, DMSO-d_6) δ 10.09 (s, 1H), 8.81 (d, *J* = 5.2 Hz, 1H), 8.41 (d, *J* = 1.3 Hz, 1H), 8.27 (d, *J* = 2.6 Hz, 1H), 7.81 (dd, *J* = 5.2, 1.4 Hz, 1H), 7.59 (dd, *J* = 8.9, 2.5 Hz, 1H), 7.23 (d, *J* = 8.1 Hz, 1H), 6.94 – 6.91 (m, 2H), 6.91 (s, 1H), 6.85 – 6.79 (m, 1H), 3.75 (s, 3H), 3.59 (s, 2H). 13C NMR (126 MHz, DMSO) δ 169.05, 166.32, 159.67, 157.57, 154.76, 137.97, 131.80, 129.79, 123.66, 121.79, 121.59, 119.84, 119.52, 118.34, 118.30, 115.37, 112.36, 55.46, 43.87.

41

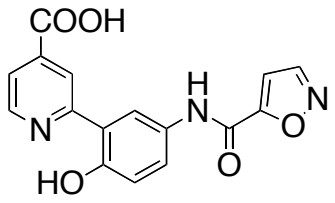

Molecular Weight: 325.28

To a glass vial, add isoxazole-5-carbonyl chloride (0.071 mmol, 9.3 mg) (Maybridge), N-hydroxysuccinimide (0.13 mmol, 15 mg), and 0.5 mL acetonitrile. Stir at ambient temperature for 1 hr. Add SPSA011 (0.013 mmol, 3 mg) in 0.5 mL 1:1:1 water/acetonitrile/methanol, and stir at ambient temperature for 16 hrs. HPLC purification (0.1 % TFA, MeOH/water gradient: 0-5 min, 15 % B; 5-10 min, 15-40 % B; 10-35 min, 40-100 % B) followed by freeze drying yielded 1.0 mg of orange solid (0.004 mmol, 33 %). LCMS $[M+H]^+$ *m/z* = 326.18. 1H NMR (400 MHz, DMSO-d6) δ 10.72 (s, 1H), 8.84 (dd, J = 5.2, 0.8 Hz, 1H), 8.82 (d, J = 1.9 Hz, 1H), 8.48 (dd, J = 1.5, 0.9 Hz, 1H), 8.43 (d, J = 2.6 Hz, 1H), 7.86 – 7.81 (m, 2H), 7.24 (d, J = 1.9 Hz, 1H), 7.00 (d, J = 8.9 Hz, 1H). 13C NMR (126 MHz, DMSO) δ 165.87, 162.78, 157.05, 155.36, 153.78, 151.92, 148.25, 140.01, 129.79, 124.63, 121.28, 119.75, 119.48, 119.13, 117.95, 106.62.

42

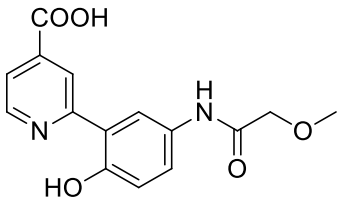

Molecular Weight: 302.28

To a glass vial, add 2-methoxyacetyl chloride (0.071 mmol, 6.5 μL), N-hydroxysuccinimide (0.13 mmol, 15 mg), and 0.5 mL acetonitrile. Stir at ambient temperature for 1 hr. Add SPSA011 (0.013 mmol, 3 mg) in 0.5 mL 1:1:1 water/acetonitrile/methanol, and stir at ambient temperature for 16 hrs. HPLC purification (0.1 % TFA, MeOH/water gradient: 0-10 min, 15 % B; 10-15 min, 15-40 % B; 15-35 min, 40-80 % B) followed by freeze drying yielded 1.5 mg of yellow solid

(0.005 mmol, 50 %). LCMS $[M+H]^+$ *m/z* = 303.22. ^{1}H NMR (400 MHz, DMSO-d_6) δ 9.70 (s, 1H), 8.82 (d, *J* = 5.2 Hz, 1H), 8.45 (s, 1H), 8.34 (d, *J* = 2.5 Hz, 1H), 7.83 (dd, *J* = 5.2, 1.5 Hz, 1H), 7.74 (dd, *J* = 9.1, 2.3 Hz, 1H), 6.92 (d, *J* = 8.8 Hz, 1H), 3.99 (s, 2H), 3.40 (s, 3H). 13C NMR (126 MHz, DMSO) δ 167.72, 165.87, 157.34, 154.66, 148.11, 139.97, 130.52, 123.98, 121.10, 119.28, 118.74, 118.69, 117.71, 71.78, 58.74

43

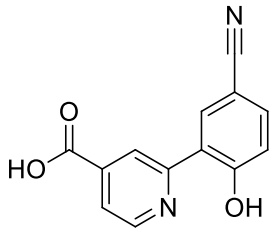

Molecular Weight: 240.21

To a sealed pressure vial was added methyl 2-bromo-4-pyridinecarboxylate (0.19 mmol, 30 mg), 5-cyano-2-hydroxyphenylboronic acid (0.28 mmol, 61 mg) (Combi-Blocks), cesium carbonate (0.70 mmol, 228 mg), Pd6 mixed catalyst (0.014 mmol, 7 mg) (CombiPhos), and 2 mL DMF. The mixture was heated to 120 °C for 5 hr. Upon cooling to ambient temperature, the mixture was acidified with 2 M HCl, extracted with EtOAc, washed with brine, and concentrated. The product was isolated by HPLC purification (0.1 % TFA, acetonitrile/water gradient: 0-5 min, 10 % B; 5-20 min, 10-40 % B; 20-30 min, 40-100 % B) followed by freeze drying yielded 3.0 mg of grey solid (0.013 mmol, 7 %) and the unhydrolyzed methyl ester was not collected. LCMS $[M+H]^+$ *m/z* = 241.18. ^{1}H NMR (400 MHz, DMSO) δ 8.85 (d, *J* = 5.1 Hz, 1H), 8.68 (s, 1H), 8.62 (d, *J* = 2.1 Hz, 1H), 7.88 (dd, *J* = 5.2, 0.9 Hz, 1H), 7.76 (dd, *J* = 8.5, 2.1 Hz, 1H), 7.12 (d, *J* = 8.5 Hz,

1H). ^{13}C NMR (100 MHz, DMSO) δ 166.02, 162.21, 155.71, 148.35, 140.42, 139.87, 135.12, 133.30, 122.21, 121.20, 120.89, 119.14, 101.86.

44

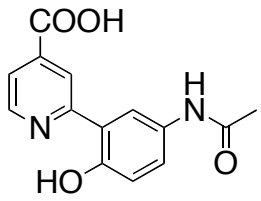

Molecular Weight: 272.26

To a glass vial was added SPSA011 (2 mg, 0.009 mmol), acetic anhydride (5 µL, 0.053 mmol, Sigma), and 250 µL water. The reaction was allowed to stir at ambient temperature for 30 min then diluted in HPLC solvent. HPLC purification (0.1 % TFA, MeOH/water gradient: 0-5 min, 15 % B; 5-10 min, 15-50 % B; 10-35 min, 50-90 % B) followed by freeze drying yielded 2.2 mg of yellow solid (0.008 mmol, 90 %). LCMS $[M+H]^+$ *m/z* = 273.57. 1H NMR (400 MHz, DMSO-d6) δ 9.86 (s, 1H), 8.82 (dd, J = 5.2, 0.8 Hz, 1H), 8.41 (dd, J = 1.5, 0.9 Hz, 1H), 8.23 (d, J = 2.6 Hz, 1H), 7.82 (dd, J = 5.1, 1.4 Hz, 1H), 7.57 (dd, J = 8.8, 2.6 Hz, 1H), 6.91 (d, J = 8.8 Hz, 1H), 2.03 (s, 3H). 13C NMR (126 MHz, DMSO) δ 167.90, 165.87, 157.23, 154.14, 148.23, 139.90, 131.49, 123.30, 121.08, 119.39, 118.94, 117.86, 117.80, 23.87.

45

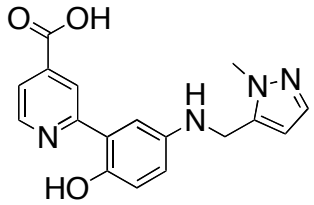

Molecular Weight: 324.33

Combine SPSA011 (0.017 mmol, 4 mg), 1-methyl-1H-pyrazole-5-carbaldehyde (0.034 mmol, 3.3 µL), and 1 mL EtOH in a round bottom flask fitted with a reflux condenser. Stir 2 hrs at 100°C. Add sodium borohydride (0.068 mmol, 2.6 mg), stir 30 min at 100°C. HPLC purification (0.1 % TFA, methanol/water gradient**:** 0-8 min, 5 % B; 5-22 min, 5-75 % B; 22-34 min, 100 % B) followed by freeze drying yielded 1.8 mg of product (0.00356 mmol, 33 %). LCMS $[M+H]^+$ *m/z* = 325.16. 1H NMR (400 MHz, Methanol-d4) δ 8.79 (dd, J = 5.3, 0.9 Hz, 1H), 8.53 (t, J = 1.2 Hz, 1H), 7.98 (dd, J = 5.3, 1.4 Hz, 1H), 7.76 (d, J = 2.7 Hz, 1H), 7.53 (d, J = 2.0 Hz, 1H), 7.23 (dd, J = 8.8, 2.7 Hz, 1H), 7.07 (d, J = 8.8 Hz, 1H), 6.51 (d, J = 2.0 Hz, 1H), 4.75 (s, 2H), 3.70 (s, 3H). 13C NMR (126 MHz, MeOD) δ 165.81, 157.24, 155.77, 146.98, 140.66, 137.97, 137.17, 122.40, 121.42, 119.69, 119.33, 118.95, 116.30, 107.04, 42.38, 35.24.

46

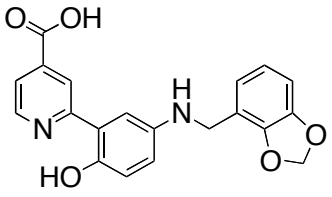

Molecular Weight: 364.35

Combine SPSA011 (0.038 mmol, 9 mg), 2,3-(Methylenedioxy)benzaldehyde (0.075 mmol, 8.6 µL) (Combi-Blocks), 2 mL EtOH, and 100 uL glacial acetic acid in a round bottom flask fitted with a reflux condenser. Stir 3 hrs at ambient temperature. Add sodium borohydride (0.15 mmol, 6 mg), stir 30 min at ambient temperature. Quench by addition of ~10 drops 2N HCl. HPLC purification (0.1 % TFA, methanol/water gradient**:** 0-8 min, 5 % B; 5-22 min, 5-75 % B; 22-34 min, 100 % B) followed by freeze drying yielded 6.4 mg of product (0.018 mmol, 47 %). LCMS $[M-H]^-$ *m/z* = 363.14. 1H NMR (400 MHz, DMSO-d6) δ 8.79 (dd, J = 5.2, 0.8 Hz, 1H), 8.43 (d, J = 1.4 Hz, 1H), 7.80 (dd, J = 5.2, 1.4 Hz, 1H), 7.47 (s, 1H), 7.04 – 6.74 (m, 5H), 6.03 (s, 2H), 4.32 (s, 2H). 13C NMR (126 MHz, DMSO) δ 165.96, 158.17, 157.90, 157.54, 148.08, 146.77, 145.32, 139.89, 121.92, 121.59, 120.88, 119.31, 118.49, 117.40, 115.06, 107.57, 100.84.

47

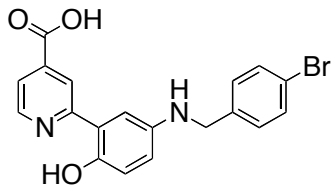

Molecular Weight: 399.24

Combine SPSA011 (0.02 mmol, 4.6 mg), 4-bromobenzaldehyde (0.08 mmol, 15 mg), and 1 mL EtOH in a round bottom flask fitted with a reflux condenser. Stir 2 hrs at 100°C. Add sodium borohydride (0.08 mmol, 3 mg), stir 30 min at 100°C. HPLC purification (0.1 % TFA, methanol/water gradient**:** 0-8 min, 5 % B; 5-22 min, 5-75 % B; 22-34 min, 100 % B) followed by freeze drying yielded 3.2 mg of product (0.008 mmol, 40 %). LCMS $[M+H]^+$ *m/z* = 399.13, 401.11. 1H NMR (400 MHz, DMSO-d6) δ 8.79 (dd, J = 5.1, 0.8 Hz, 1H), 8.41 (s, 1H), 7.79 (dd, J = 5.2, 1.4 Hz, 1H), 7.55 (d, J = 8.4 Hz, 2H),

7.39 (d, J = 8.4 Hz, 2H), 7.26 – 6.95 (m, 1H), 6.83 (s, 1H), 4.36 (s, 2H), 1.75 (s, 1H). 13C NMR (126 MHz, DMSO) δ 171.91, 166.41, 158.61, 158.35, 157.87, 148.63, 140.31, 131.70 (2C), 130.84 (2C), 121.39, 120.06, 118.84, 118.06, 115.71, 22.99.

Chapter 3: Inhibition of Histone Lysine Demethylases by DR241 and Derivatives

I. Introduction

KDM4 subfamily members of JmjC domain containing histone lysine demethylases are frequently amplified and required for proliferation in several types of cancer, including esophageal squamous cell carcinomas, [51] primary mediastinal B cell lymphomas, Hodgkin lymphomas,[52]androgen-dependent prostate carcinomas,[36]and basal-like breast cancers. [53] This subfamily consists of five catalytically active members, A-E, each of which contains N-terminal JmjN and JmjC domains which are both required for catalysis. The removal of a methyl group from the ε-amine of tri- and di-methyllysine is accomplished by oxidation of the methyl group by molecular oxygen to form an unstable hemiaminal, which spontaneously decomposes with elimination of formaldehyde (**Figure 1-1**). This reaction requires Fe^{II} and an alpha-ketoglutarate (αKG) cosubstrate in addition to oxygen. Thus far, several substrates have been identified for the KDM4 subfamily, although only two are well-characterized: methylated lysine 9 of histone H3 (H3K9), and, in the case of KDM4A, B, and C only, methylated lysine 36 of histone H3 (H3K36).[25,36,79]

Histone proteins assemble with DNA into nucleosomes, the basic structural element of chromatin, and histone post-translational modifications are known to play an important role in regulating transcription. The modifications removed by the KDM4 enzymes are no exception: H3K36 methylation is associated with transcriptional elongation, and H3K9 methylation promotes heterochromatin formation and gene silencing. [114] Therefore, the KDM4 subfamily has been proposed to promote cellular proliferation and oncogenesis by modulating transcription at one or more oncogene(s)/tumor suppressor(s) by antagonizing H3K9/36 methylation.

Working from this hypothesis, several attempts have been made to use JmjC inhibitors in cellular models of KMD4 oncogenesis, with encouraging results in lung cancer[69]and in prostate cancer. [48,62] However, currently available inhibitors suffer from both low potency and low selectivity, making it difficult to distinguish the effects of inhibiting the KDM4 subfamily from other closely related JmjC proteins. There is therefore a critical need for new and better inhibitors targeting the KDM4 subfamily.

We have previously described our efforts to develop new KDM4 inhibitors based on computational fusing of docked 5-aminosalicylate fragments followed by chemical elaboration, resulting in potent and selective inhibition of a subset of JmjC demethylases. Besides the 5-aminosalicylates, this docking screen of approximately 600,000 small molecule fragments identified several other promising compounds, among which was 2-(2-(ethylamino)pyrimidin-4-yl)isonicotinic acid (DR241), with a measured IC_{50} of 1.18 μM and a Ligand Efficiency (LE) of 0.45, both very favorable for a small molecule fragment. Here we describe our initial efforts to optimize this screening hit, resulting in greatly increased potency against the KDM4 subfamily. Crystal structures of several derivatives confirm the accuracy of the docking predictions and show key interactions resulting in acquisition of potency.

II. Docking Prediction of DR241 Binding Pose

The predicted docking pose of DR241 (**Figure 1**) suggests that the active site iron is coordinated by two heterocyclic nitrogen ligands, one from the pyridine and one from the pyrimidine ring, and that the pyridine carboxylate moiety of DR241 interacts with the side chains of Tyr134 and Lys208. In addition, the exocyclic 2'-amino group of the pyrimidine ring forms a hydrogen bond with the side chain of Glu192. We predict that these interactions are important for the observed inhibitory activity of DR241. Most importantly, this docking pose predicts that DR241 is rotated approximately 90° with respect to the binding pose of αKG, such that the 6' position of the pyrimidine ring is oriented toward the peptide substrate binding pocket. This suggests that modifications at the 6' position of the pyrimidine ring will extend towards the lesser-conserved peptide binding pocket.

Figure 1: Docking Pose of DR241

Docking prediction of DR241 binding to KDM4A, showing important predicted interactions with labeled residues (Tyr134, Glu192, and Lys208), and iron (green sphere).

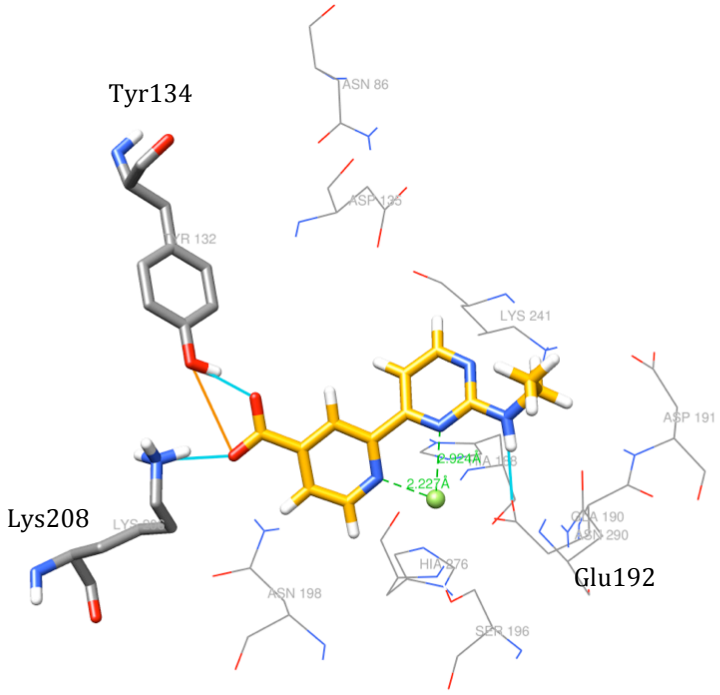

III. Synthesis of 2-(2-aminopyrimidin-4-yl)isonicotinic acid Scaffold

Exploration of the structure-activity relationships of the 2-(2-aminopyrimidin-4-yl)isonicotinic acid scaffold first required us to identify a facile route for synthesis of the scaffold and derivatives. An obvious synthetic scheme involves formation of a carbon-carbon bond between the pyridine and pyrimidine heterocycles as a key reaction. This reaction is non-trivial however, as cross-coupling reactions involving 2-pyridyl substituents are notoriously difficult, primarily due to the instability of the functionalized 2-pyridyl reagents. [115] Numerous attempts to effect this coupling reaction using the methods of Negishi, Stille, and Suzuki with various boronic esters met with limited success. Finally we turned to the method described by Burke et. al. using MIDA protected boronates, [116] which afforded the desired 2-pyridyl coupling reagent (**Scheme 1 A**), and when paired with 4-halo pyrimidines, the desired coupling product (**Scheme 1 D**). Coupling with pre-functionalized pyrimidine regents in an efficient convergent synthesis allowed access to diverse derivatives.

Scheme 1: Synthesis of Inhibitor Scaffold and Derivatives

A) Lithium-halogen exchange and in-situ quenching with $B(OiPr)_3$ gives the intermediate tri-isopropyl borate, followed by ligand exchange to the MIDA ester coupling reagent. B) Iodination followed by nuclophilic aromatic substitution with a variety of amines gives access to 5-aminopyrimidine derivatives used in the subsequent coupling reaction. C) Enolate chemistry with a variety of alkyl halides followed by condensation with guanidine and bromination gives access to 5-alkylpyrimidine derivatives used in the subsequent coupling reaction. D) Suzuki coupling between pyridine MIDA ester and derivatized pyrimidine followed by hydrolysis affords the target compound.

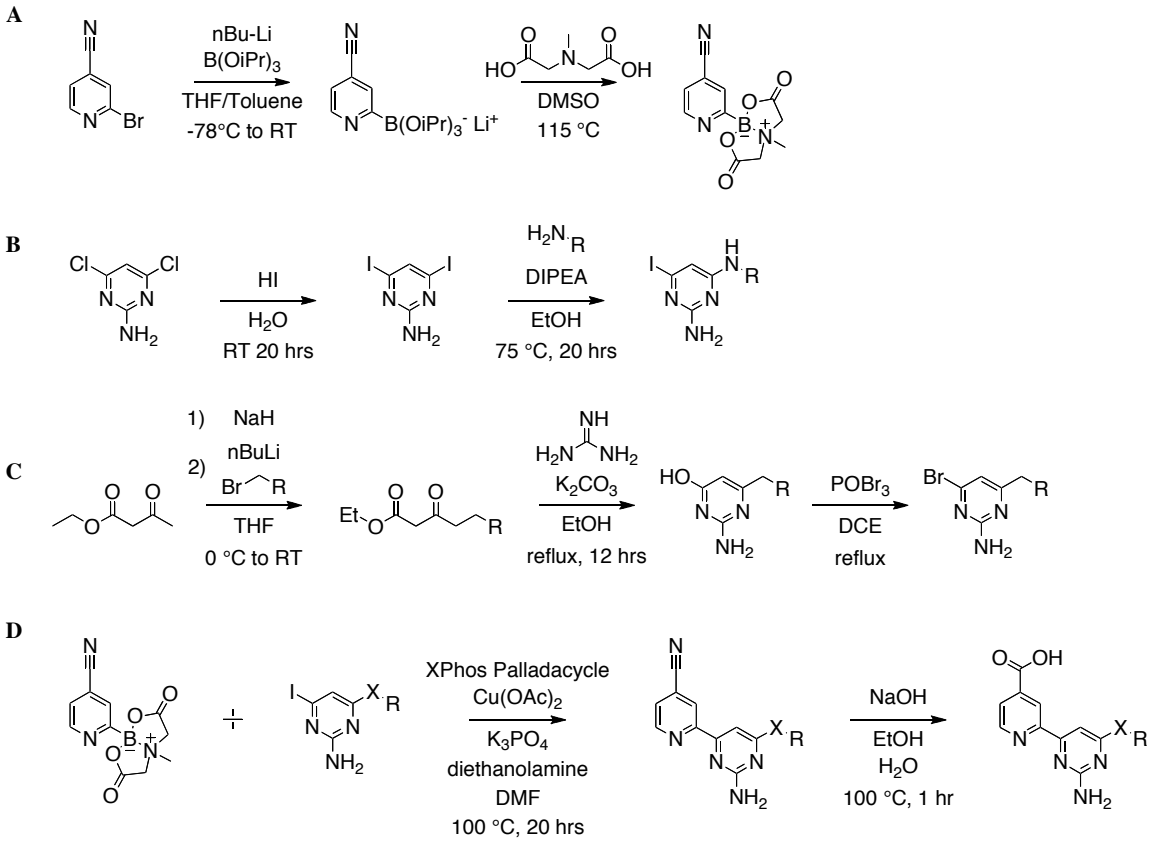

IV. SAR of Inhibitor Scaffold

Initially, we sought to define the critical elements of the 2-(2-aminopyrimidin-4-yl)isonicotinic acid scaffold required for target engagement by systematically altering key predicted interactions between the scaffold and KDM4C. To do this, derivatives of the scaffold with perturbations in individual atoms or chemical motifs predicted to interact with KDM4C were synthesized and tested for inhibition of KDM4C using a Time-Resolved Fluorescence Resonance Energy Transfer (TR-FRET) assay (**Table 1**). These investigations found that the carboxylic acid substituent of the pyridine ring, predicted to coordinate Tyr134 and Lys208 in the enzyme active site, is critical for potent inhibition (EI502-2, **Table 1**). Similarly, the presence of heterocyclic nitrogen atoms predicted to chelate iron is required for inhibition (EI501-6 and EI506-2, **Table 1**). We found that eliminating the ethane group from the exocyclic 2'-amino of the pyrimidine increases potency by 16-fold (IC_{50} from 1.2 μM to 0.075 μM) (EI513-2, **Table 1**). Furthermore, removal of the exocyclic 2'-amino group entirely has the same effect, increasing potency by approximately 16-fold (IC_{50} = 0.070 μM) (EI505-2, **Table 1**), suggesting that the predicted hydrogen bond between this exocyclic nitrogen and Glu192 does not form *in vitro*.

Together, this data allows for two key conclusions: First, by confirming the importance of several key moieties, it is largely supportive of the importance of interactions predicted by docking pose of DR241, and second, by demonstrating SAR around moieties uninvolved in iron chelation (ie carboxylic acid, exocyclic 2' amino group) it suggests a direct binding mode of inhibition rather than inhibition due to iron

chelation in solution, a concerning possibility when inhibiting a metal dependent reaction.

Table 1: SAR of Key Scaffold Functionalities

TR-FRET inhibition assays showing IC_{50} values for compounds derived from DR241, investigating key predicted interactions between the scaffold and KDM4C. αKG concentration is 2 μM.

Compound	IC_{50}, μM
DR241 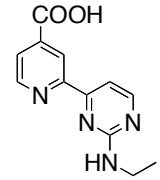	1.2
EI513-2 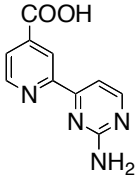	0.070
EI505-2 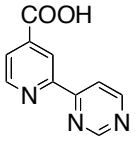	0.070
EI502-2 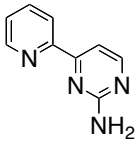	267
EI501-6 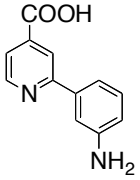	68
EI506-2 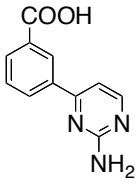	318

V. Continued SAR of DR241-Derived Inhibitors

Having accumulated evidence supporting the predicted docking pose of DR241 and preliminary SAR supporting a direct binding mode of inhibition, we next sought to extend our investigation of this scaffold's SAR, focusing on the 6' position of the pyrimidine ring. We chose this position because of its predicted orientation towards the peptide substrate binding pocket, which in contrast to the highly conserved active site is more divergent across the JmjC family. We hypothesized that by derivatizing from this position we would be able to achieve both more potent and more selective inhibition of the KDM4 subfamily. A diverse set of derivatives was synthesized by the methods presented in **Scheme 1**.

Initially, we sought to determine exocyclic heteroatom tolerance at this position, reasoning that this might uncover any nearby, readily accessible interactions with KDM4C, as well as identify possible linkers for further derivitization. We found that both methoxy and amino derivatives were approximately equipotent with the underivatized scaffold, indicating a lack of nearby enzyme active site contacts (**Table 2**). Next, we appended small, medium, and large groups in order to define the derivative size tolerance. Size seemed to have little effect on enzyme binding, as we saw, for example, approximately equipotent inhibition from a large di-benzyl substituted amino derivative (IC_{50} = 4.79 μM) and from the underivatized scaffold (IC_{50} = 2.71 μM) (**Table 2**). This indicates that there is substantial room around the 6' position of the pyrimidine ring, as would be expected if, as predicted by docking, this position faces the expansive peptide substrate binding pocket.

Although there was limited SAR observed for a range of derivatives of diverse size and functionality, we observed that a 2-phenylethanamino derivative (EI514-2) (IC_{50} = 0.37 μM) conferred increased potency relative to similar derivatives (**Table 2**). We therefore decided to explore the SAR around this derivative by substituting the benzyl ring with different functionalities at different positions (**Table 3 A,B**), and by varying the length and composition of the linker between the benzene and the scaffold (**Table 3 B,C**). We found that hydroxyl substitution of an ethyl linked benzene derivative at any position resulted in minimal change in potency. However, when we replaced the alkyl linker with an exocyclic amino linker, we saw much stronger SAR trends. In this case, the otho-, meta-, and para-hydroxyl benzene derivatives showed IC_{50}'s of 0.34, 0.12, and 6.35 μM, respectively, compared with 1.34 μM for the unsubstituted benzene with an amino linker (**Table 3 A**). We attribute this linker-dependent SAR to restriction of flexibility of the benzene derivatives imposed by the exocyclic amino group versus the more conformationally flexible alkyl linker, which in unfavorable cases may force steric clashes between the benzene moiety and the wall of the peptide binding pocket while in favorable cases may reduce the entropic costs of binding. We further found that for ortho-hydroxyl benzene derivatives, the length of the alkyl linker significantly affects potency. Linker lengths of 0, 1, 2, and 3 carbons result in IC_{50}'s of 1.41, 0.19, 0.72, and 1.15 μM, respectively (**Table 3 C**). Again, we believe that optimum linker length may be explained by invoking a balance between conformational flexibility and entropic costs of binding. Several diverse para-substituted benzene derivatives were tested, with minimal effects on potency (**Table 3 B**).

Overall, exploration of the SAR of DR241 revealed 1) the important contributions of the carboxylate and both iron-chelating moieties to potency, 2) the detrimental effect of the 2'-amino ethane group, and 3) the feasibility of extensive derivatization at the 6' position of the pyrimidine. In this study, we have been able to increase potency of DR241 16-fold by removing the 2'-aminoethane group, and a further 23-fold by incorporating the most potent 6' derivative (NY3_70). The overall increase in potency achieved is therefore approximately 368-fold.

Table 2: 6'-pyrimidine SAR

TR-FRET inhibition assays showing IC_{50} values for compounds derived from DR241, investigating diverse substitutions at the 6' position of the pyrimidine ring. αKG concentration is 50 μM.

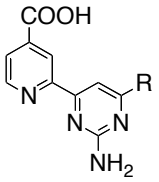

Compound	KDM4C TR-FRET IC_{50} (μM)
EI513-2 	2.71
NY3_8 	2.98
EI517-2 	5.68
NY2_143 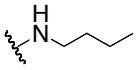	1.24
NY3_44 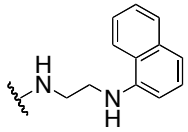	1.43
EI717-2 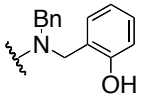	4.79
EI514-2 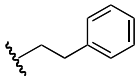	0.37

Table 3: Focused 6'-pyrimidine SAR

TR-FRET inhibition assays showing IC_{50} values for compounds derived from DR241. αKG concentration is 50 μM. A) Amine- and alkyl-linked benzyl and phenol derivatives. B) Para-substituted alkyl-linked benzyl derivatives. C) Varying alkyl linker length with para-hydroxy phenol derivative.

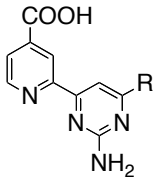

A

Compound	KDM4C TR-FRET IC_{50} (μM)
EI514-2 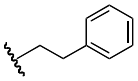	0.37
NY3_33 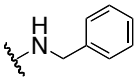	1.34
EI541-2 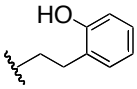	0.72
NY3_36 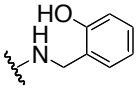	0.34
EI543-2 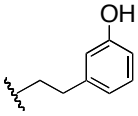	1.39
NY3_70 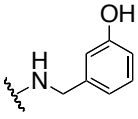	0.12
EI540-2 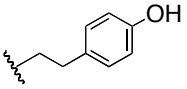	0.27
NY3_37 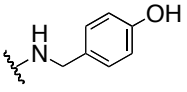	6.35

B

Compound	KDM4C TR-FRET IC_{50} (μM)
EI514-2 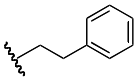	0.37
EI610-2 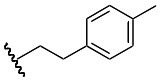	0.63
EI567-2 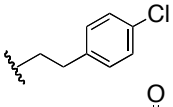	0.59
EI618-4 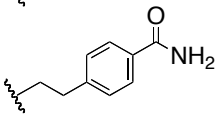	0.73

C

Compound	KDM4C TR-FRET IC_{50} (μM)
EI650-2 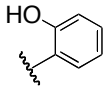	1.41
EI572-2 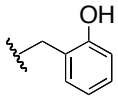	0.19
EI541-2 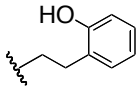	0.72
EI565-2 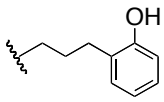	1.15

VI. Crystallography

In order to more fully evaluate docking predictions as well as to identify key interactions made by 6' derivatives and to predict further avenues for derivatization, we sought to obtain co-crystal structures of several inhibitors bound to the KDM4 subfamily member KDM4A. Our collaborators at the Structural Genomics Consortium were able to initially solve a crystal structure of des-ethyl DR241 (EI513-2) (**Figure 2**), which closely matches the predicted binding pose of EI513-2 (**Figure 2**). Important interactions with active site residues are present as predicted, including bonds between the pyridyl carboxylate and the side chains of Tyr134 and Lys208 and chelation of the active site iron by the heterocyclic nitrogen atoms of both pyridyl and pyrimidine rings. Interestingly, the orientation of the 2' exocyclic amino group of the pyrimidine ring with respect to Glu192 was predicted correctly, although the predicted hydrogen bonding interaction does not seem to be present, as discussed earlier.

Figure 2: Comparison of Docking Prediction and Crystal Structure

Overlay of predicted docking pose of des-ethyl DR241 (EI513-2) (pink) and crystallized structure (yellow). Residues making contact with EI513-2 are labeled. Iron (Nickel for the purposes of crystallography) is shown as a green sphere.

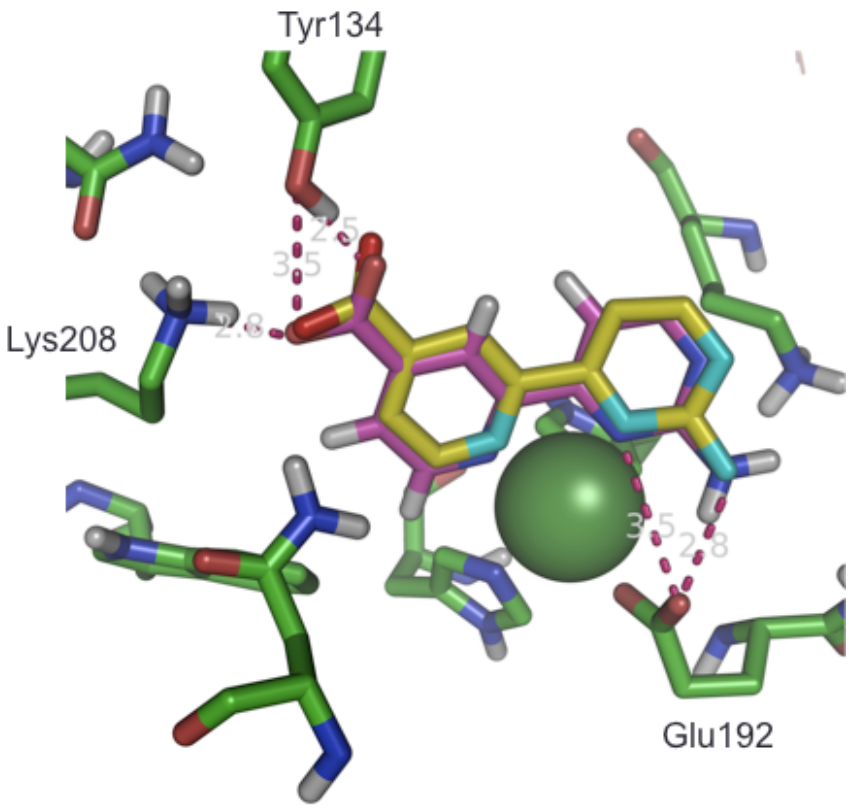

Further efforts yielded crystal structures of several alkyl-linked 6' derivatives: EI514-2, EI543-2, EI540-2, and EI541-2 (**Figure 3**). These structures confirm the binding pose of the core pyridyl-pyrimidine scaffold, which consistently binds to the active site making key contacts with the active site metal, as well as side chains Tyr134 and Lys208. The derivatives extend as expected towards the peptide substrate binding region of the active site, and make key interactions with active site side chains. Interestingly, the derivatives seem to adopt one of two general poses, either 'down' in the case of EI514-2 and EI543-2 (**Figure 3 A**), or 'up' in the case of EI540-2 and EI541-2 (**Figure 3 C,D**). The downward facing meta-hydroxyl substituted derivative, EI514-2, forms a hydrogen bond between the hydroxyl group and the side chain of Asp193. The unsubstituted derivative, EI514-2, almost perfectly overlaps with EI514-2, but lacking a hydroxyl substituent is unable to form a hydrogen bond (**Figure 3 A**). The upward facing para-hydroxyl substituted derivative, EI540-2, forms a hydrogen bond between the hydroxyl group and the side chain of Asn88. The other upward facing derivative, ortho-hydroxyl substituted EI541-2, is rotated with respect to EI540-2 to form a hydrogen bond between the hydroxyl group and the side chain of Asp137 (**Figure 3 D**).

As presented earlier, there is minimal difference in potency across these derivatives despite the presence of specific interactions between them and the active site of KDM4A. It is important to mention here that the electron densities defining the positions of the 6' derivative groups are of poor quality, in contrast to the well-defined density of the core scaffold and the enzyme itself. This likely indicates the presence of multiple binding conformations for each derivative, with the most highly populated one (at cryogenic temperatures) shown in the structure. Multiple binding conformations are

most likely to occur if there is not significant stabilization energy associated with a single conformation. As the peptide binding pocket is large and well-hydrated, it may be that any hydrogen bonds formed between the derivatives and enzyme side chains are associated with displacement of a similar bond between the enzyme side chain and a molecule of water, resulting in a net change in binding energy near zero. This would be consistent with the similar potencies observed across our small panel of crystallized derivatives.

Figure 3: Crystal Structures of 6' Derivatives

Crystal structures of several alkyl-linked benzene/phenol derivatives bound to KDM4A with important interactions labeled. (A) Structures of bound EI514-2 (salmon) and EI543-2 (yellow). (B) Chemical structures of co-crystallized derivatives. (C) Structures of bound EI540-2 (blue) and EI541-2 (pink). (D) Structures of bound EI540-2 (blue) and EI541-2 (pink) rotated 90° relative to (C).

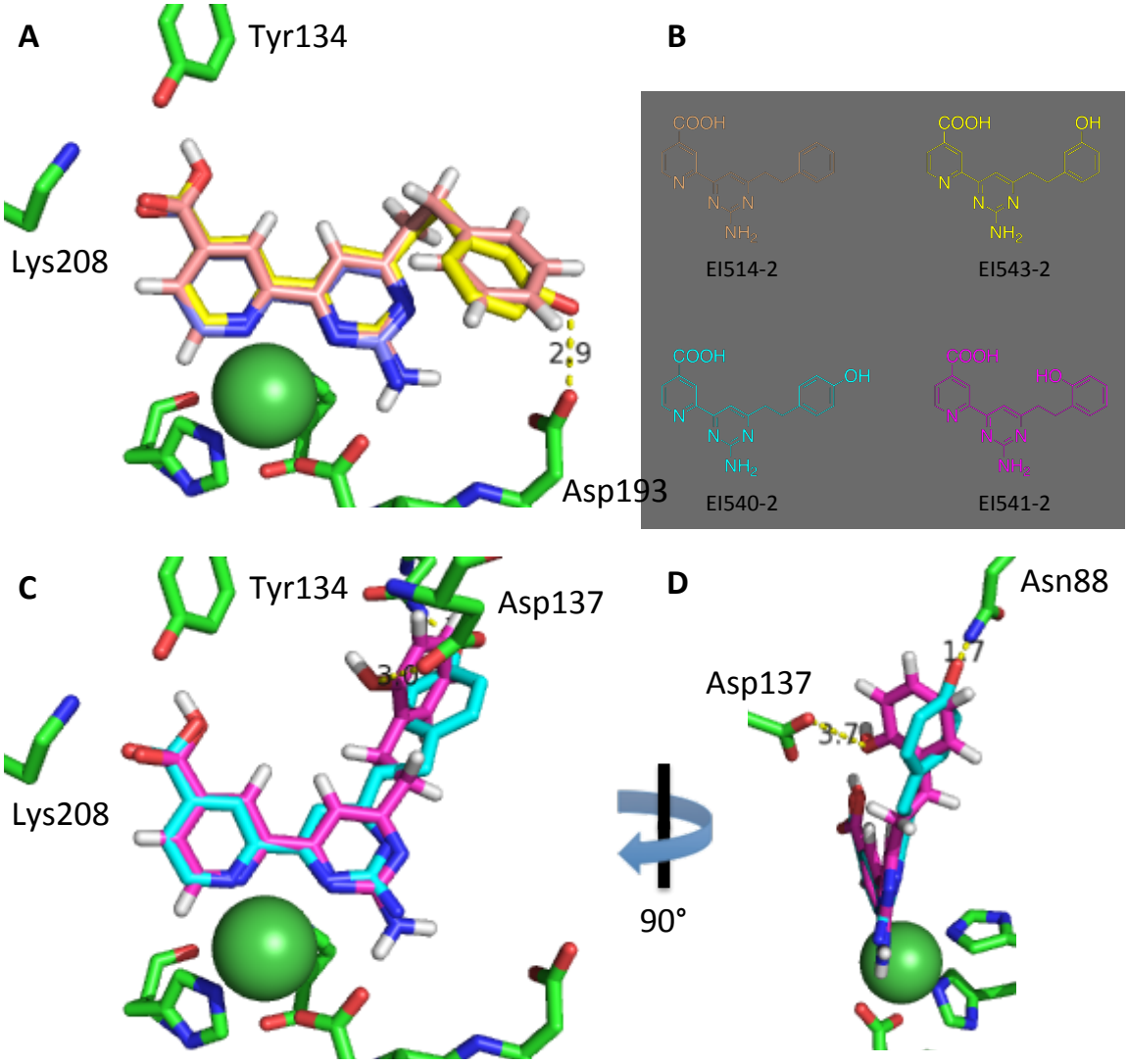

VII. Selectivity

One important goal of our efforts to design an inhibitor of the KDM4 subfamily of JmjC demethylases is to spare to the greatest possible extent other related JmjC demethylases and hydroxylases. Of particular importance are the JmjC hydroxylases, among which are key regulators of the hypoxic response such as PHD2 and FIH. The reaction catalyzed by the JmjC hydroxylases is mechanistically identical to that catalyzed by the JmjC demethylases, with resultant hydroxylation versus demethylation determined by substrate characteristics. As the substrates themselves differ substantially between the KDM4 demethylases and hydroxylases, we reasoned that selectively inhibiting the KDM4 subfamily over the hydroxylases would be a feasible goal. Additionally, uncoupling the transcriptional effects of KDM4 inhibition from those of activating the hypoxic response is critical for being able to correctly attribute a biological response to treatment with a small molecule.

We therefore decided to screen our compounds for inhibition of FIH. Our goal was to first screen as widely as possible, picking from the more potent derivatives. Unfortunately, this effort was complicated by the lack of a suitable antibody against the product of the hydroxylation reaction catalyzed by FIH, which eliminates the possibility of using a relatively simple, high-throughput TR-FRET assay as for KDM4C. We instead relied upon a more laborious MALDI MS assay that directly detects the product and reactant peptides by mass, and can measure the extent of the reaction by calculating the ratio between amounts of the two. Determination of selectivity required the development of both FIH and KDM4C MALDI assays, in order that IC_{50}'s could be compared without complications arising from inherent differences in measured potencies between different

types of assays. In order to feasibly screen as many compounds as possible, we envisioned a triage system in which only a few compound concentrations would initially be tested to give a rough idea of the IC_{50} against FIH, followed by more thorough evaluation of the most promising compounds.

Results are shown in **Table 4**. Gratifyingly, although the MALDI inhibition assay is substantially different from the TR-FRET assay, resulting in different IC_{50} values between the two, we see similar trends in potency between these assays. Specifically, we gain approximately 10-fold in potency comparing the underivatized scaffold to the most potent of the 6' derivatives, which are approximately equipotent to 2,4 PDCA. Further, NY3_36 and EI540-2 are among the most potent derivatives in both assays, while NY3_37 is among the least. There are some slight differences in potency rankings between the assays, but this is likely due to the narrow range of measured potencies across the derivatives combined with the approximate nature of these 'rough' MALDI results, and in our opinion should not be overemphasized. Overall, we feel that the results from the MALDI inhibition assay are consistent with the results from TR-FRET, and help to validate both assays.

We next considered potencies and selectivities versus FIH. Here we see a much larger range of values, from slightly over 1 μM to greater than 100 μM. We also see that selectivities in excess of 10 fold, and probably significantly more, are possible. For example, EI541-2 is 50-fold selective for KDM4C over FIH. Although this data is preliminary and must be confirmed by more careful and thorough follow-up inhibition assays, it is encouraging to see such robust selectivity. Perhaps most importantly, we see an interesting trend suggesting that the composition of the linker region, specifically the

exocyclic atom immediately adjacent to the 6' position of the pyrimidine ring, has a large effect on selectivity. In general, the amino-linked derivatives are less selective than the alkyl-linked derivatives, and the single ether-linked compound profiled seems to be among the more selective as well. This data suggests that selectivity against FIH may be achieved by more fully exploring the SAR around this linker region.

Table 4: Selectivity Versus FIH

MALDI MS inhibition assays against KDM4C and FIH using 0, 1, 10, and 50/100 μM inhibitor, with the highest concentration depending on solubility. All compounds are 6' derivatives of the desethyl-DR241 scaffold. Approximate IC_{50} values are given. The use of '>' indicates that 50 % inhibition was not reached even at the highest concentration of inhibitor tested. Selectivity is calculated as the ratio of the IC_{50} for KDM4C and the IC_{50} for FIH, and compounds are arranged from least to most selective. αKG concentration is 100 μM.

Compound	KDM4C MALDI IC_{50} (μM)	FIH MALDI IC_{50} (μM)	Selectivity
NY3_44 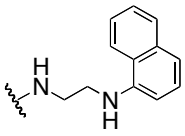	10	1-10	0.1-1
EI517-2 	10-100	10-100	0.1-10
EI513-2 	10	10-100	1-10
NY3_37 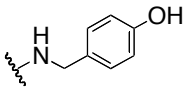	10	10-100	1-10
NY3_33 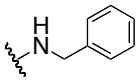	10	10-100	1-10
NY2_143 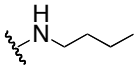	1-10	10-100	1-100
NY3_36 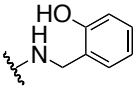	1	10-100	10-100
EI514-2 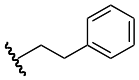	10	>50	>5
EI543-2 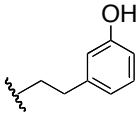	1-10	>50	>5->50
EI540-2 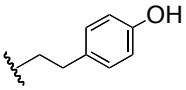	1-10	>50	>5->50
NY3_8 	10	>100	>10
EI541-2 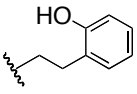	1	50	50

Although selectivity against FIH and other hydroxylases is critical, it is also important, and much more challenging, to achieve selectivity over the more closely related demethylase subfamilies. In order to assess the specificity of our inhibitors for inhibition of the KDM4 subfamily over other demethylases we developed a MALDI assay to assess inhibition of KDM5A, an H3K4 demethylase that is a member of the subfamily most similar to KDM4.

As expected given their similarity, we see minimal selectivity between KDM4C and KDM5A (**Table 5**). For most compounds, the difference in IC_{50}'s between KDM4C and KDM5A is too close to distinguish without testing additional, more closely spaced concentrations of inhibitor, meaning that the selectivity is probably close to one, or at most around 10. It is tempting to claim that some of the apparent selectivity seen, for example 10-fold for EI541-2, may be genuine. However, given the limited number of data points supporting this conclusion and the fairly small window of selectivity observed, more thorough testing would be required to confirm this finding.

Table 5: Selectivity Versus KDM5A

MALDI MS inhibition assays against KDM4C and KDM5A using 0, 1, 10, and 50/100 μM inhibitor, with the highest concentration depending on solubility. All compounds are 6' derivatives of the desethyl-DR241 scaffold. Approximate IC_{50} values are given. The use of '>' indicates that 50 % inhibition was not reached even at the highest concentration of inhibitor tested. Selectivity is calculated as the ratio of the IC_{50} for KDM4C and the IC_{50} for KDM5A, and compounds are arranged in the same order as Table 4. αKG concentration is 100 μM.

Compound	KDM4C MALDI IC_{50} (μM)	KDM5A MALDI IC_{50} (μM)	Selectivity
NY3_44 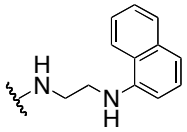	10	1-10	0.1-1
EI517-2 	10-100	10	0.1-1
EI513-2 	10	50	5
NY3_37 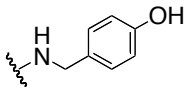	10	10-100	1-10
NY3_33 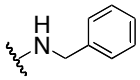	10	1-10	0.1-1
NY2_143 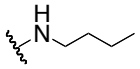	1-10	1-10	0.1-10
NY3_36 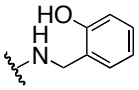	1	1-10	1-10
EI514-2 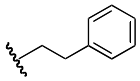	10	1-10	0.1-1
EI543-2 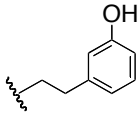	1-10	1-10	0.1-10
EI540-2 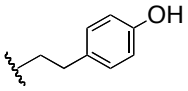	1-10	1-10	0.1-10
NY3_8 	10	10-100	1-10
EI541-2 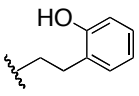	1	10	10

VIII. Conclusion

In conclusion, we have described the development of a series of potent histone demethylase inhibitors based on a scaffold identified by computational docking. This pyridyl-pyrimidine scaffold was synthetically challenging to access, a challenge that was overcome through the use of a recently described MIDA protecting group for the labile 2-pyridyl boronate. This application of the 2-pyridyl MIDA boronate technology extends its functional group tolerance to the versatile cyano group, potentially allowing access to a wide range of novel compounds.

Synthetic access to the scaffold and derivatives thereof allowed for the exploration of its SAR, resulting in compounds with greatly improved potency. Initially, removing the 2' amino ethyl group resulted in a 16-fold improvement in potency. Derivatization at the 6' position of the pyrimidine identified alkyl- or amino- linked phenols with further increases in potency, as much as 23-fold improved over the des-ethyl scaffold, for a total potency increase of approximately 368-fold over the initial fragment. Crystal structures of several derivatives confirm the predicted docking pose of the scaffold, and identify possible contacts between the derivatives and the enzyme active site.

Finally, initial characterization of selectivity for KDM4C over the hydroxylase FIH and the H3K4 demethylase KDM5A shows promise. Selectivity over FIH seems to be largely determined by the linker region immediately adjacent to the 6' position of the pyrimidine ring, and further exploration of this SAR will likely result in increased selectivity. Achieving selectivity over the much more closely related KDM5A is more

challenging, and additional derivatives will need to be synthesized and tested to explore this selectivity.

IX. Materials and Methods

NY4_4

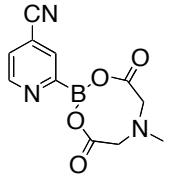

Molecular Weight: 259.03

To a 100 mL schlenk flask was added 2-bromoisonicotinate (Combi-Blocks) (4.63 g, 25.3 mmol), triisopropyl borate (5.53 g, 29.4 mmol), and THF (50 mL). The mixture was cooled to -78 °C prior to dropwise addition of 2.5 M nBu-Li in hexanes (10 mL, 25 mmol) over the course of 40 min. The reaction was maintained at -78 °C for 1 hr, followed by warming to RT for 3 hrs. This triisopropyl borate intermediate was used in the next step without isolation.

To a 250 mL three-neck flask equipped with a short-path distillation apparatus, thermometer with adaptor, and septum stopper was added N-methyliminodiacetic acid (6.34 g, 43 mmol) and 60 mL DMSO. The mixture was heated to approximately 100 °C internal temperature. The triisopropyl borate intermediate was added dropwise while maintaining an internal reaction temperature of approximately 100 °C with continuous distillation of THF. After the addition was complete, the reaction was cooled to approximately 50 °C and vacuum was used to distill the reaction to dryness. The crude reaction mixture was suspended in approximately 100 mL acetonitrile and adsorbed onto 25 g non acid-washed celite, followed by application of vacuum overnight to remove any remaining solvent. The crude reaction mixture adsorbed to celite was then loaded onto a 100 g silica column and eluted with 10 % hexanes in ethyl acetate followed by ethyl

acetate alone to give 1.18 g pure product (4.6 mmol, 18 %). TLC R_f = 0.29 (10 % MeCN/EtOAc). LCMS $[M+H]^+$ *m/z* = 260.28. 1H NMR (600 MHz, Acetonitrile-d3) δ 8.89 (dd, J = 5.0, 1.0 Hz, 1H), 7.90 (dd, J = 1.7, 1.0 Hz, 1H), 7.60 (dd, J = 5.0, 1.7 Hz, 1H), 4.15 – 3.97 (m, 4H), 2.55 (s, 3H).

NY3_26

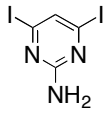

Molecular Weight: 346.90

To a 50 mL flask was added 4,6 dichloropyrimidin-2-amine (420 mg, 2.0 mmol), NaI (400 mg, 2.67 mmol), and hydriodic (57 wt. % in H_2O) (6 mL, 45 mmol). The reaction was heated to 40 °C for 1 hr, then cooled to RT for 20 hrs. The reaction was filtered, and the collected precipitate was washed sequentially twice with 20 mL H_2O, twice with 20 mL saturated sodium bicarbonate, and twice with 20 mL H_2O. The solid was then dried under vacuum, yielding 684 mg product (1.97 mmol, 98 %), which was used without further purification. LCMS $[M+H]^+$ *m/z* = 347.93. 1H NMR (600 MHz, DMSO-d6) δ 7.45 (d, J = 1.4 Hz, 1H), 7.35 (s, 2H).

General Amination Procedure:

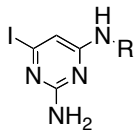

To a 10 mL flask is added NY3_26 (90 mg, 0.25 mmol), amine (0.35 mmol), Hunig's base (122 uL, 0.35 mmol), and 1 mL ethanol. The reaction is heated to 75 °C for 20 hrs,

then cooled to RT and diluted in 50 mL H_2O. The reaction is extracted three times with 50 mL ethyl acetate, which is combined, washed with 50 mL saturated NaCl, then dried over $MgSO_4$. After filtration, the organics are concentrated under reduced pressure, then purified by silica gel chromatography to yield the pure product.

General Coupling Procedure:

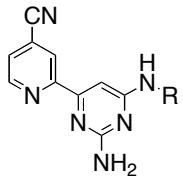

To a 10 mL schlenk flask is added NY3_26 (15 mg, 0.06 mmol), 4-iodo pyrimidine (0.04 mmol), copper(II) acetate (5 mg, 0.028 mmol), xphos palladacycle (1.5 mg, 0.002 mmol), potassium phosphate tribasic (42 mg, 0.20 mmol), diethanolamine (4 uL, 0.04 mmol), and 1 mL DMF. The reaction is heated to 100 °C for 20 hrs, then cooled to RT and quenched by addition of 2 mL 2 N HCl followed by 2 mL 2 N NaOH. The reaction is extracted three times with 5 mL ethyl acetate, then the combined organics are washed with 5 mL saturated NaCl, then dried over $MgSO_4$. After filtration and concentration under reduced pressure the crude reaction is purified by silica gel chromatography to yield the pure product.

General Hydrolysis Procedure:

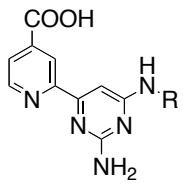

To a 20 mL vial is added the coupled pyridyl-pyrimidine derivative, 2 N NaOH (500 uL, 1 mmol) and 400 uL ethanol. The reaction is refluxed for 4 hrs, then cooled to RT and quenched with 500 uL 2 N HCl. The reaction is then concentrated under reduced pressure, re-suspended in 2 mL ethanol, and filtered through a cotton plug. The filtrate is purified by HPLC to give the final compound (10 – 70 % gradient of methanol in 10 mM NH_4HCO_3 pH 9.5).

NY3_8

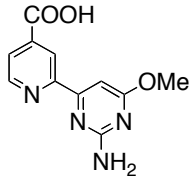

Molecular Weight: 246.22

General Coupling Procedure was carried out using 4-iodo-6-methoxypyrimidin-2-amine (Combi-Blocks) (10 mg, 0.04 mmol). Crude compound was used without silica gel purification. General Hydrolysis Procedure was carried out as described, yielding 0.59 mg product (0.0024 mmol, 6 %). LCMS $[M+H]^+$ *m/z* = 247.23.

NY2_143

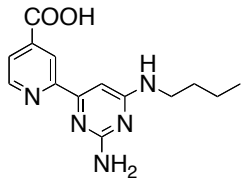

Molecular Weight: 287.32

General Coupling Procedure was carried out using N^4-butyl-N^2-diboc-6-chloropyrimidin-2,4-diamine (16 mg, 0.04 mmol). Crude compound was purified by silica gel

chromatography (1:2 ethyl acetate:hexanes). General Hydrolysis Procedure was carried out as described, yielding 1.3 mg product (0.005 mmol, 11 %). LCMS $[M+H]^+$ *m/z* = 288.32. 1H NMR (400 MHz, Methanol-d4) δ 8.93 (dd, J = 4.9, 0.9 Hz, 1H), 8.52 (t, J = 1.1 Hz, 1H), 8.10 (dd, J = 4.9, 1.4 Hz, 1H), 6.82 (s, 1H), 3.55 (t, J = 7.1 Hz, 2H), 1.71 – 1.61 (m, 2H), 1.46 (dt, J = 14.9, 7.4 Hz, 2H), 0.99 (t, J = 7.4 Hz, 3H).

NY3_44

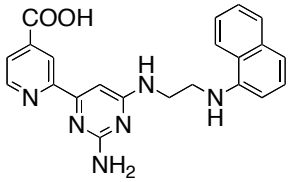

Molecular Weight: 400.43

General Amination Procedure was carried out as described, using N-(1-naphthyl)ethylenediamine (91 mg, 0.35 mmol). The product was purified by silica gel chromatography (1:4 ethyl acetate:hexanes). General Coupling Procedure was carried out as described using N^4-(N-(1-naphthyl)ethylenediamine)-6-chloropyrimidin-2,4-diamine (15 mg, 0.04 mmol). The product was purified by silica gel chromatography (2:3 ethyl acetate:hexanes). General Hydrolysis Procedure was carried out as described, yielding 1.5 mg product (0.0037 mmol, 9 %). LCMS $[M+H]^+$ *m/z* = 401.31.

NY3_33

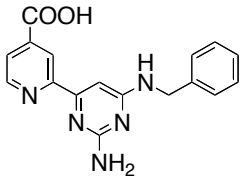

MW: 321.33

General Amination Procedure was carried out as described, using benzylamine (38 uL, 0.35 mmol). The product was purified by silica gel chromatography (1:2 ethyl acetate:hexanes). General Coupling Procedure was performed as described, using N^4-benzylamine-6-chloropyrimidin-2,4-diamine (13 mg, 0.04 mmol). The product was purified by silica gel chromatography (5:2 ethyl acetate:dichloromethane + 0.2 % triethylamine), followed by HPLC (10 – 70 % acetonitrile in H_2O + 0.1 % trifluoroacetic acid). General Hydrolysis Procedure was performed as described, yielding 1.9 mg product (0.0059 mmol, 15 %). LCMS $[M+H]^+$ *m/z* = 322.19.

NY3_36

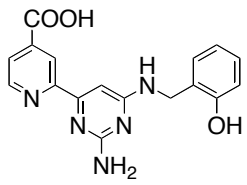

Molecular Weight: 337.33

General Amination Procedure was carried out as described, using 2-aminomethyl phenol (45 mg, 0.37 mmol). The product was purified by silica gel chromatography (1:2 ethyl acetate:hexanes). General Coupling Procedure was performed as described, using N^4-(2-aminomethyl phenol)-6-chloropyrimidin-2,4-diamine (14 mg, 0.04 mmol). The product was purified by silica gel chromatography (2:1 ethyl acetate:dichloromethane + 1 % triethylamine). General Hydrolysis Procedure was performed as described, yielding 1.1 mg product (0.0033 mmol, 8.2 %). LCMS $[M+H]^+$ *m/z* = 338.24.

NY3_37

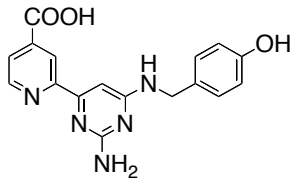

Molecular Weight: 337.33

General Amination Procedure was carried out as described, using 4-aminomethyl phenol (43 mg, 0.35 mmol). The product was purified by silica gel chromatography (1:1 ethyl acetate:hexanes). General Coupling Procedure was performed as described, using N^4-(4-aminomethyl phenol)-6-chloropyrimidin-2,4-diamine (20 mg, 0.06 mmol). The product was purified by silica gel chromatography (4:1 ethyl acetate:dichloromethane + 1 % triethylamine). General Hydrolysis Procedure was performed as described, yielding 0.7 mg product (0.002 mmol, 3.5 %). LCMS $[M+H]^+$ *m/z* = 338.28.

NY3_70

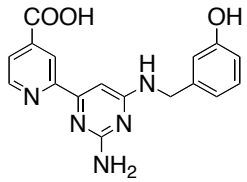

Molecular Weight: 337.33

General Amination Procedure was carried out as described, using 3-aminomethyl phenol (43 mg, 0.35 mmol). General Coupling Procedure was performed as described, using N^4-(3-aminomethyl phenol)-6-chloropyrimidin-2,4-diamine (21 mg, 0.06 mmol). The product was purified by silica gel chromatography (3:1 ethyl acetate:dichloromethane). General Hydrolysis Procedure was performed as described, yielding 3.7 mg product (0.01 mmol, 18 %). LCMS $[M+H]^+$ *m/z* = 338.24.

Chapter 4: Cellular Inhibition of KDM4C

I. Introduction

Having developed a variety of histone demethylase inhibitors with favorable *in vitro* potency and selectivity, we next sought to test these inhibitors in cells. As discussed in previous chapters, there are certain barriers to activity in the context of cells that are not present when inhibiting a recombinant target. These include the presence of a hydrophobic membrane that must be crossed by the inhibitor, a multitude of potential off-target proteins that are not present in a simplified reconstituted system, degredative enzymes that may metabolize the inhibitor, and the possibility of redundant or otherwise incompletely understood pathways leading to modulation of a given cellular readout of inhibitor activity.

Although there are several examples of published demethylase inhibitors with cell activity[63,65,67,69,73,102], the majority are inactive. And even among the few cell active demethylase inhibitors there are often, and in the case of inhibitors targeting the KDM4 subfamily, always, significant liabilities that restrict their further development or use as chemical probes of cellular demethylase function. Importantly, in most cases the cellular potency is much lower than the *in vitro* potency, raising the likelihood of off-target effects when cells are treated at the high concentrations necessary for efficacy. Efforts to increase cellular activity have met with limited success.

We have used several strategies to identify and attempt to overcome these challenges, including simplified cellular systems, multiple cell lines, independent assays to uncouple cellular activity from cellular permeability, and various chemical modifications to increase hydrophobicity. Although ultimately unsuccessful, we believe

that the infrastructure developed during the course of this work and the knowledge gained have positioned us well for future efforts to develop cell active demethylase inhibitors.

II. Transient Transfection Assay

Anticipating that we would likely encounter problems achieving cell permeability given the hydrophilic, charged nature of our inhibitors, we first sought to employ a simplified cellular readout eliminating as many confounding factors as possible. Previous efforts to develop demethylase inhibitors have made use of transient transfection assays for this purpose.[67,73,102] In these assays, a JmjC histone lysine demethylase or a catalytically active fragment thereof is transiently transfected into some convenient human cell line, often HeLa or similar, which is then treated with inhibitor. Immunofluorescence is then used to visualize changes in the substrate histone methyl mark, and changes in the amount of substrate present with and without inhibitor treatment are compared.

We implemented an assay of this type to monitor cellular inhibition of the catalytic domain of KDM4C (**Figure 1**). There are a couple of important features of our assay worth discussing. First, we chose to use only the catalytic portion of KDM4C in order to both recapitulate as closely as possible the construct used for *in vitro* testing, and also to prevent reader domain-mediated recruitment of KDM4C to specific genomic loci in order to induce global demethylation. Ensuring global demethylation increases the range of the assay and greatly simplifies data analysis. Second, we were unable to achieve robust expression and demethylation using HeLa cells as previously reported,[66,73] and therefore developed this assay using U2OS osteosarcoma cells. In an attempt to control for cell type-specific effects we also tested inhibition in HEK293 cells.

Figure 1: Transient Transfection Assay

Schematic representation of the transient transfection assay. U2OS cells are first seeded in a 96-well glass-bottom plate, and allowed to attach. They are then transfected with the catalytic portion of KDM4C (amino acids 1-420) with GFP fused to the C-terminus, treated with inhibitors, and allowed to grow for 48 hours. They are then fixed, permeabilized, stained with anti-H3K9(Me3) antibody, and imaged. An overlay of images acquired on the same field of view in the GFP channel and H3K9(Me3) channel allows identification of successfully transfected cells and correlation of transfection with the amount of H3K9(Me3) present in the nucleus. In untreated cells, successful transfection results in depletion of H3K9(Me3), while H3K9(Me3) levels are normal in successfully transfected cells treated with cell-active inhibitor.

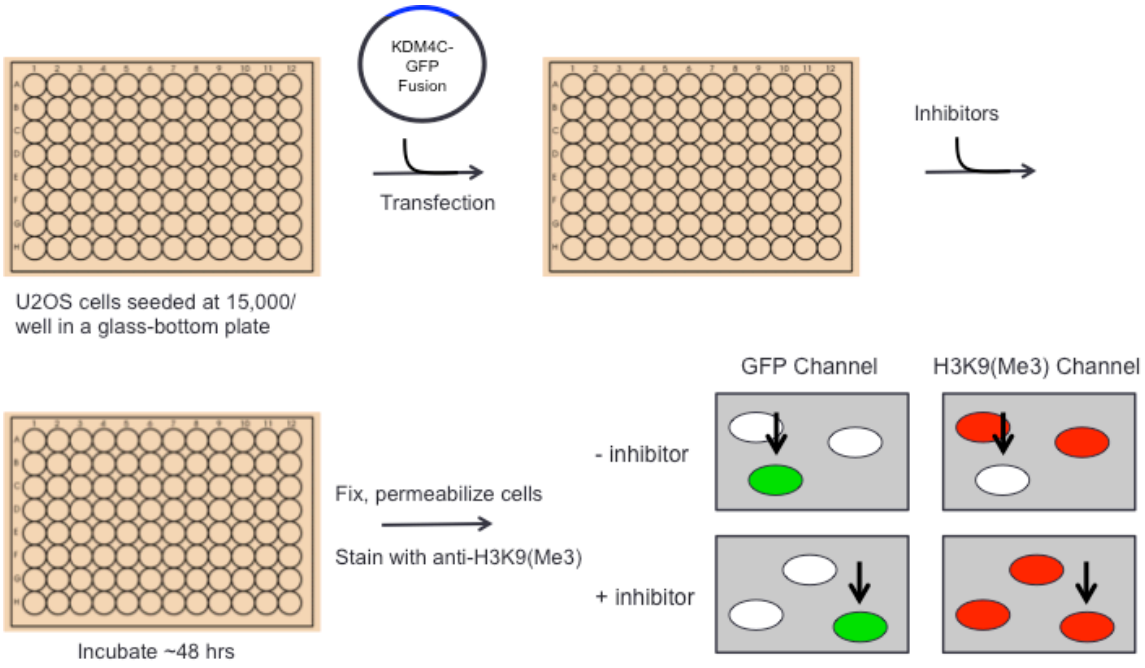

To validate our assay, we used the cell active JmjC demethylase inhibitor IOX1. This compound robustly inhibits cellular demethylation at a concentration of 500 μM (**Figure 2**). We next tested a small panel of hybrid derivatives and DR241 derivatives showing good *in vitro* activity (**Figure 3**). Unfortunately, none of these compounds inhibited KDM4C in this cellular assay up to the highest concentrations tested.

Figure 2: Transient Transfection Assay Validation

Transient transfection assay without inhibitor treatment (top) and treated with control inhibitor IOX1 (middle/bottom). Red arrows identify individual GFP+ cells.

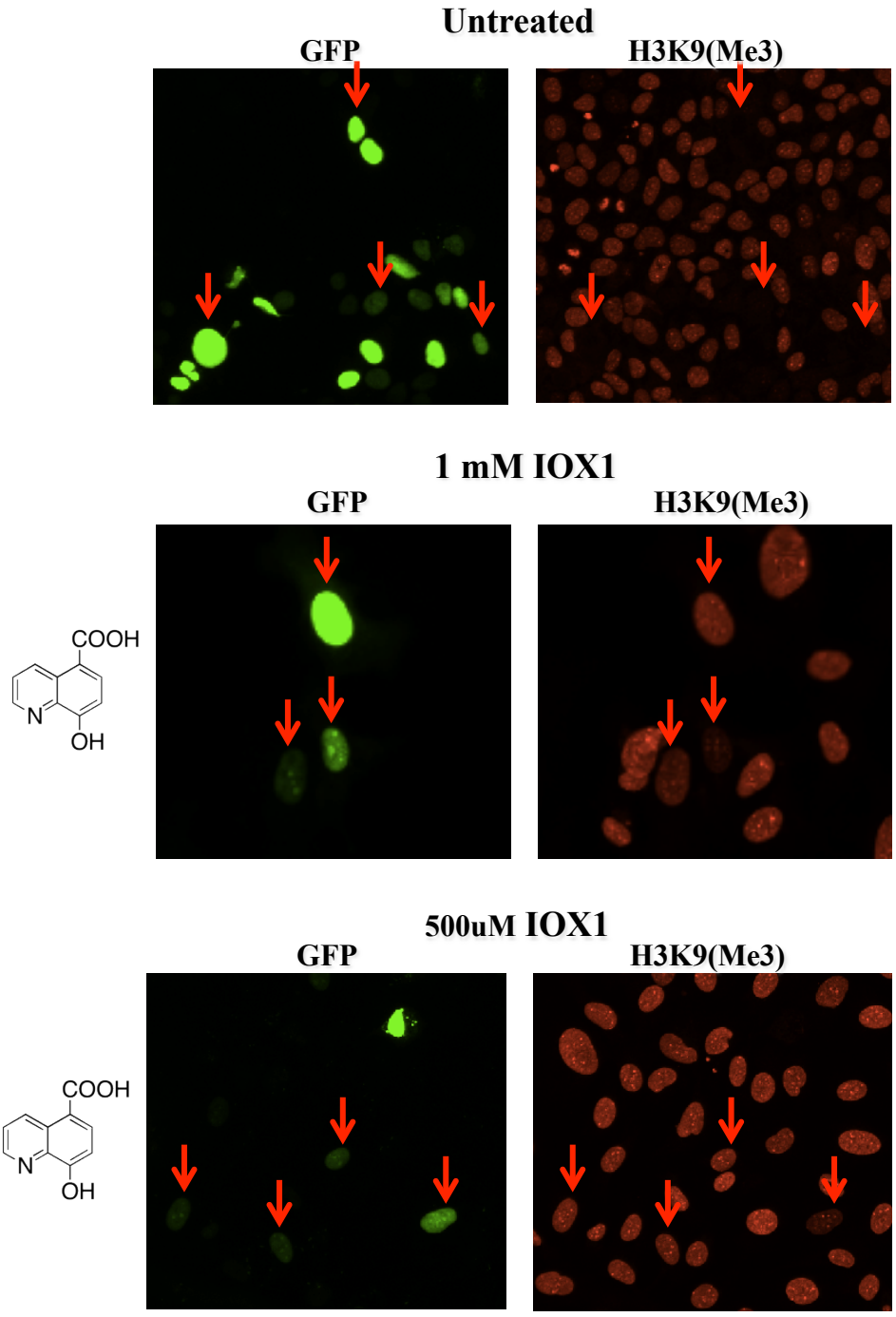

Figure 3: Transient Transfection Assay With Hybrid and DR241 Derivatives

Transient transfection assay in U2OS cells with a small panel of Hybrid and DR241 derivatives. The concentration of compound shown is in each case the highest tested. Compound concentration was limited by solubility. Red arrows identify individual GFP+ cells.

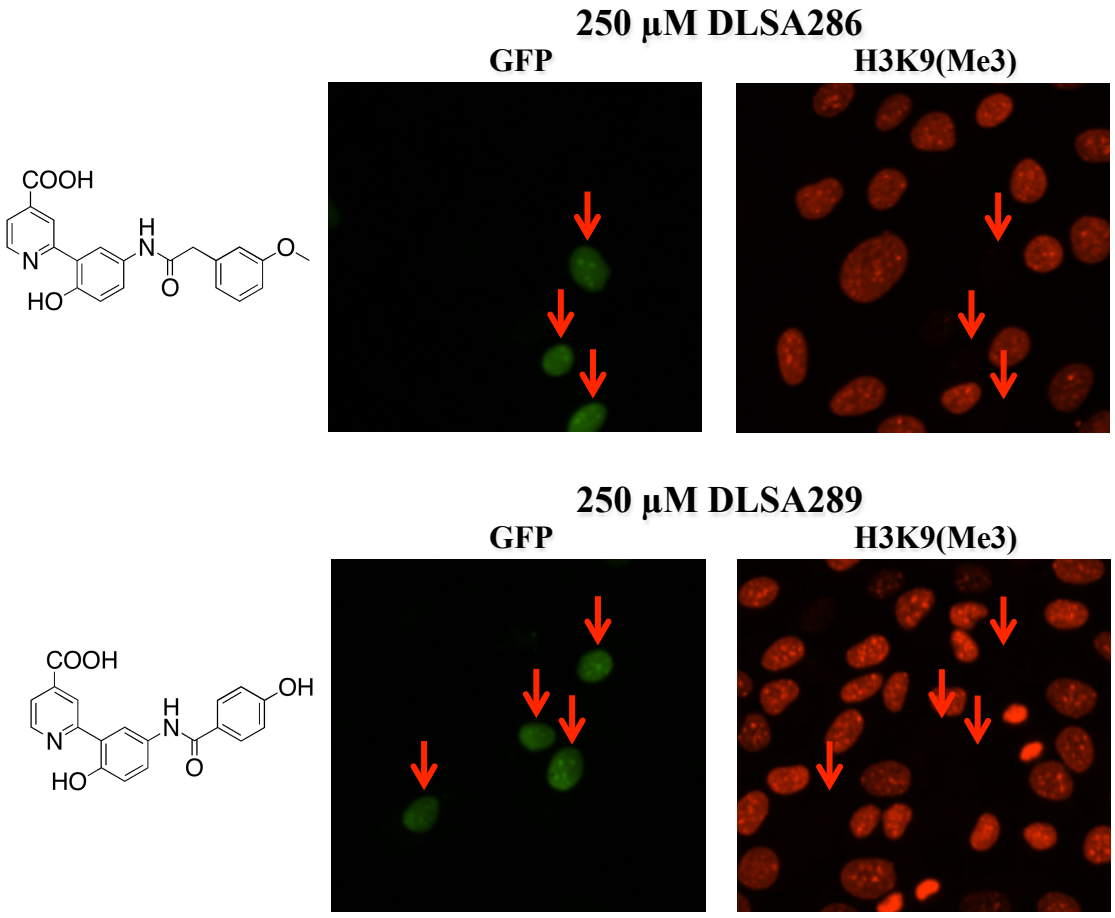

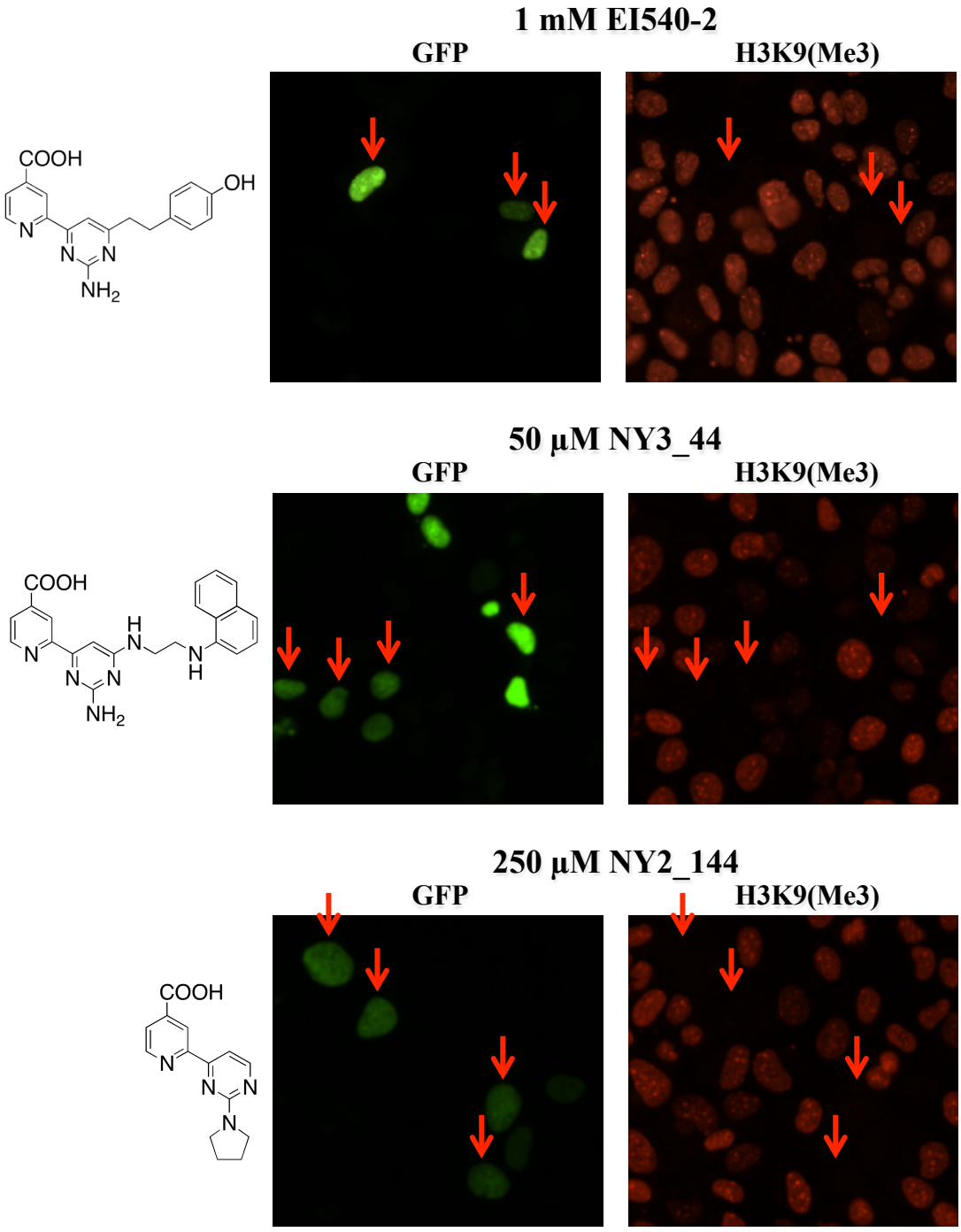
1 mM EI540-2
GFP
H3K9(Me3)
COOH
OH
N
N
N
NH2
50 µM NY3_44
GFP
H3K9(Me3)
COOH
H
N
N
H
N
N
N
NH2
250 µM NY2_144
GFP
H3K9(Me3)
COOH
N
N
N
N

III. Synthesis and Testing of Ester Pro-Drugs

We next considered the possibility that the charged carboxylic acid moiety common to all of our inhibitors may be preventing compound transit across the hydrophobic cellular membrane. In order to address this possibility we pursued two approaches: First, we made a variety of ester pro-drugs. An uncharged ester facilitates passage across the cellular membrane, whereupon non-specific cellular esterases cleave the ester to reveal the active acidic form of the molecule. We tried this initially because there is precedent among published demethylase inhibitors containing carboxylic acids for acquisition of cellular activity upon esterification. [66,67,73]

A small panel of esters was synthesized (**Scheme 1**), chosen both for diversity and for specific desirable properties. Methyl and methylacetate esters were selected for ease of synthesis (**Scheme 1, A, B**). N-octyl, n-butyl, and ethyl esters were selected based on a promising report of their use in achieving both cell activity and *in vitro* selectivity in the context of the inhibitor IOX1, [66] with the N-octyl ester of IOX1 reportedly active both in cells and *in vitro*, with a high degree of *in vitro* selectivity for the KDM4 subfamily (**Scheme 1, C**). In contrast, we found that the N-octyl ester of the hybrid scaffold (NY4_55) was not active as an *in vitro* inhibitor of KDM4C (**Figure 4**). Finally, tertiary amine-containing esters were selected in response to the poor aqueous solubility exhibited by many of the alkyl esters (**Scheme 1, D**).

Scheme 1: Ester Synthesis

Synthesis of diverse esters was accomplished using the following reactions. A) Reaction of a carboxylic acid containing derivative with TMS-diazomethane in a mixture of DMF and methanol at room temperature for 30 minutes affords the desired methyl ester. B) Reaction of an acetylated hybrid derivative with bromomethyl acetate in DMF in the presence of triethylamine at room temperature for 45 minutes affords the desired methyl acetate ester. C) Reaction of an acetylated hybrid derivative with 1-octanol, 1-butanol, or ethanol in THF in the presence of 4-dimethylaminopyridine and 1-ethyl-3-(3-dimethylaminopropyl)carbodiimide at room temperature for 20 hours affords the desired alkyl ester. D) Reaction of an acetylated hybrid derivative with carbonyldiimidazole in DMF at room temperature for 1 hour, followed by addition of (1-methylpiperidin-4-yl)methanol, 1,8-diazabicycloundec-7-ene, and 2-(dimethylamino)ethanol, 1-methylpiperidin-4-ol, or (1-methylpiperidin-4-yl)methanol and a further reaction at 40°C for 16 hours affords the desired tertiary-amine containing ester.

A

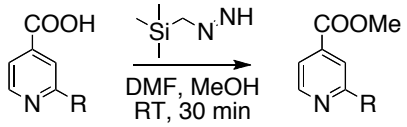

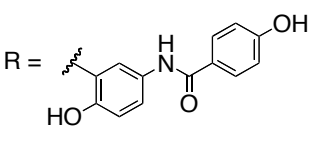

DLS289 Me-ester

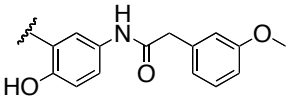

DLS286 Me-ester

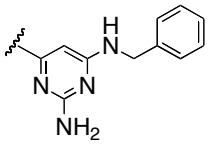

NY3_54

B

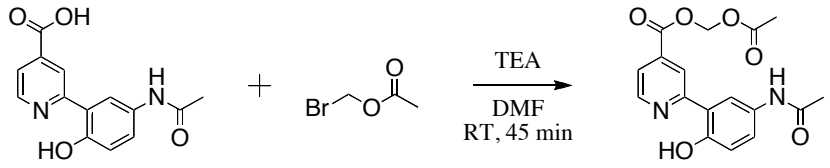

NY4_52

C

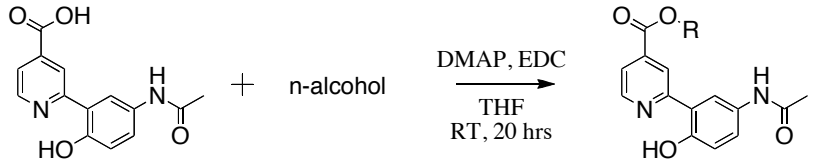

NY4_55 NY4_98 NY4_81

D

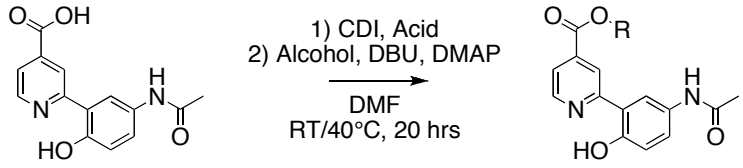

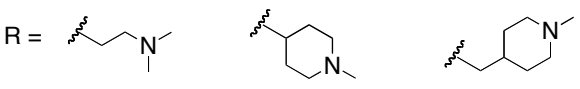

NY4_120 NY4_118 NY4_121

We tested DLSA289 Me-ester, DLSA286 Me-ester, NY3_54, NY4_52 and NY4_55 for inhibition of KDM4C in U2OS cells using the transient transfection assay (**Figure 5** and data not shown). Unfortunately, none showed inhibition of KDM4C up to the highest concentrations used. One important caveat is that we found rapid hydrolysis of NY4_120 in PBS at 37 °C. After 1 hr, only 8.3 % of this compound remained, the rest being converted to the acid (data not shown). As this was the only compound tested for stability in solution, it is possible that the other esters are similarly unstable. Whether this is detrimental to cell activity or not is difficult to say, as it may be that an ester pro-drug that undergoes uncatalyzed hydrolysis would be able to cross the cell membrane and then spontaneously hydrolyze to the active acid without relying on the presence of cellular esterases for this conversion. However, it is also possible that hydrolysis is too rapid for efficient cellular entry, and this may contribute to ester inactivity in cells. More work is needed to study the stability of hybrid derivative esters in cell culture.

Figure 4: *In Vitro* Inhibition of KDM4C By NY4_55

MALDI inhibition assay of KDM4C with IOX1 and NY4_55. The calculated IC_{50} for IOX1 is 11 μM.

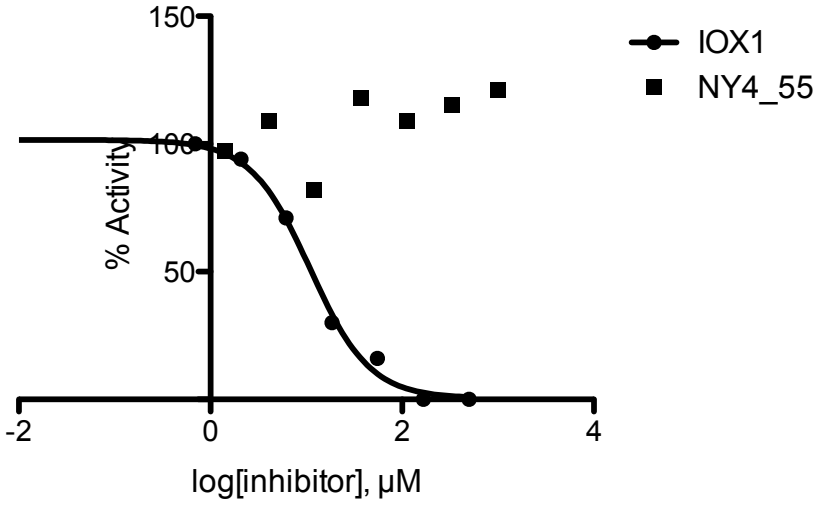

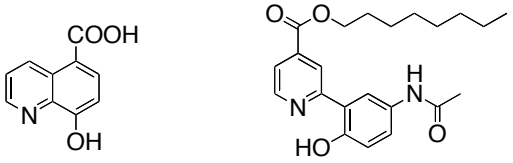

IOX1 NY4_55

Figure 5: Transient Transfection Assay Testing Methyl Esters in U2OS Cells

Transient transfection assay in U2OS cells with a small panel of methyl ester compounds. The concentration of compound shown is in each case the highest tested. Red arrows identify individual GFP+ cells.

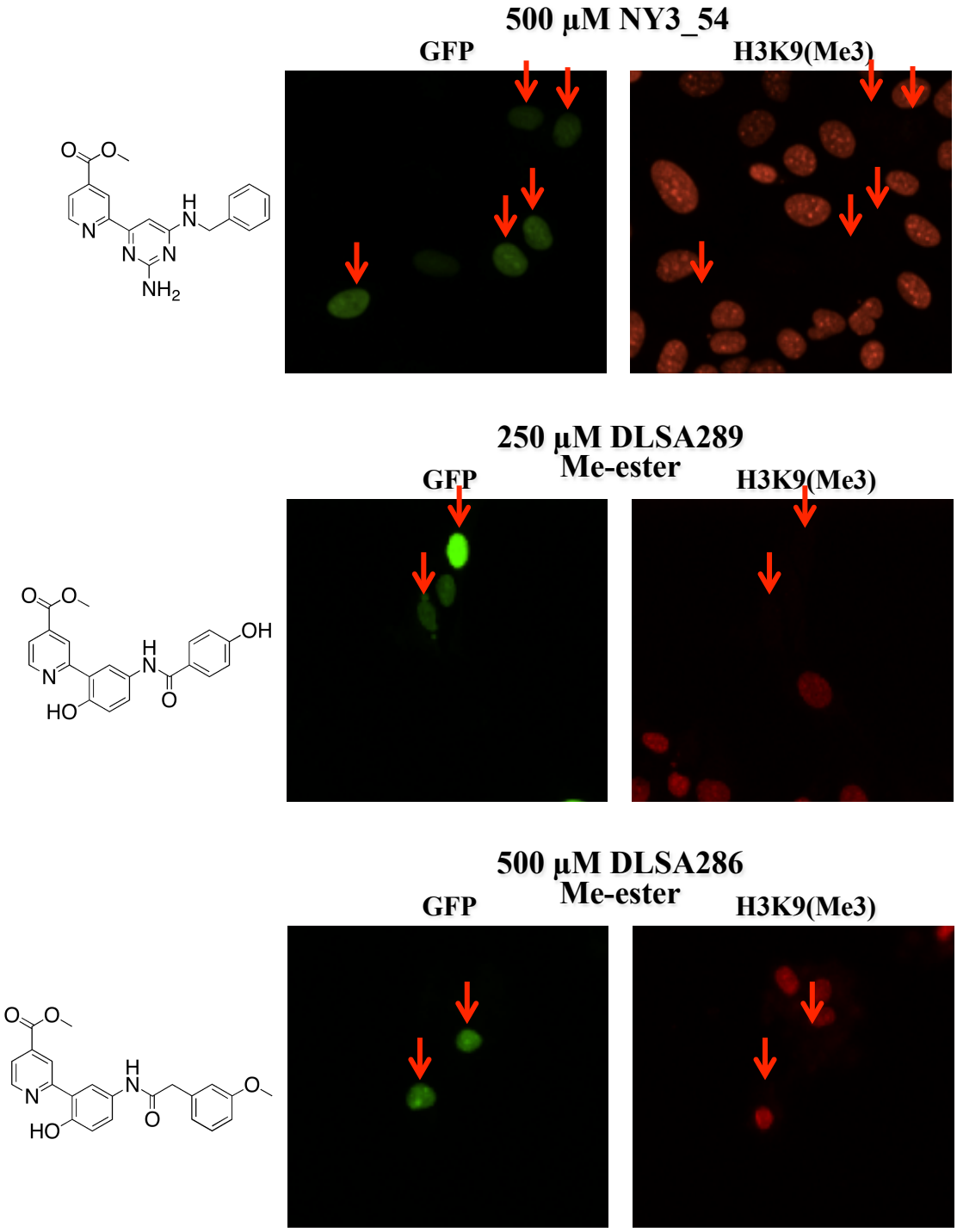

IV. Transient Transfection Assay in HEK293 Cells

One potential caveat to these cell activity results is that they may be affected by cell-type specific properties. For example, different types of cells express varying levels of drug resistance genes such as metabolic enzymes that can degrade small molecules, and transporters that can cause rapid efflux of small molecules from the cell. In addition, our pro-drug strategy requires the expression of cellular esterases, the levels of which may also be variable from cell type to cell type. In order to address these concerns we sought to establish a similar transient transfection assay using a different cell type, and selected HEK293 cells for this purpose. HEK293 cells, like U2OS cells, are easily handled and easily transfected, making them suitable for our purposes. However, compared to U2OS cells they do not adhere as well to cell culture surfaces and they adhere especially poorly to the glass-bottom plates that are used for high-throughput microscopy. For this reason the images obtained using HEK293 cells are of lower quality than those using U2OS cells, although this does not greatly affect the interpretability of the assay.

We first tested IOX and DMOG in HEK293 cells as positive controls (**Figure 6**). IOX1 inhibited KDM4C in HEK293 cells at a similar concentration found to inhibit KDM4C in U2OS cells, suggesting that cell type specific effects do not have a large impact on KDM4C inhibition by IOX1. Furthermore, we found that DMOG, a methyl ester pro-drug form of the αKG analog N-oxalylglycine (NOG), also inhibits KDM4C in HEK293 cells. This is significant because DMOG is inactive as a KDM4C inhibitor *in vitro*, and must therefore first be hydrolyzed to the active inhibitor NOG to show activity. That it is active in HEK293 cells implies that these cells are expressing esterases capable

of converting DMOG to NOG, and we reasoned that this esterase activity may also function to hydrolyze our pro-drugs to their active forms. This encouraging result prompted us to test a range of compounds including a variety of ester pro-drugs (**Figure 7** and data not shown). Tested compounds included EI540_2, NY4_55, SPSA014, NY4_98, NY4_118, NY4_120, DLSA289, and DLSA289 Me-ester. Unfortunately, none showed inhibition of KDM4C up to the highest concentrations tested.

Figure 6: Transient Transfection Assay of Control Compounds in HEK293 Cells

Transient transfection assay of HEK293 cells treated with control inhibitors IOX1 and DMOG. Red arrows identify individual GFP+ cells.

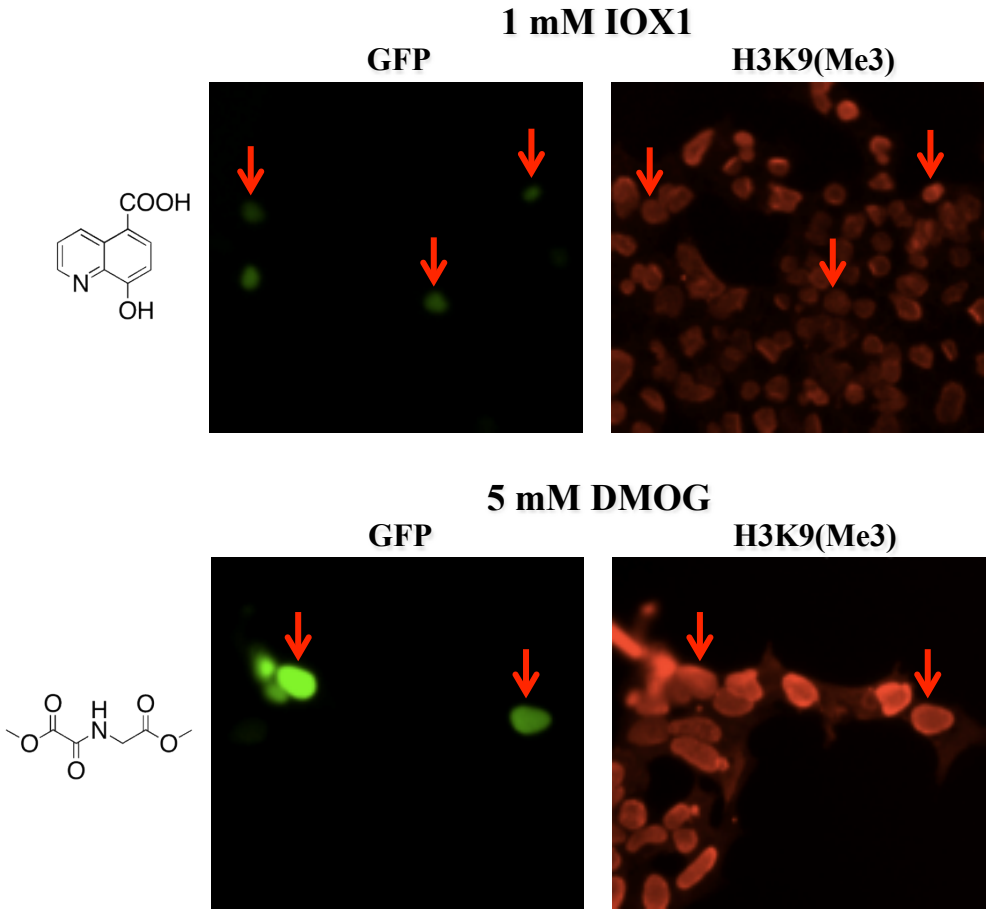

Figure 7: Transient Transfection Assay of Inhibitors in HEK293 Cells

Transient transfection assay of HEK293 cells treated with KDM4C inhibitors and ester pro-drugs thereof. Red arrows identify individual GFP+ cells.

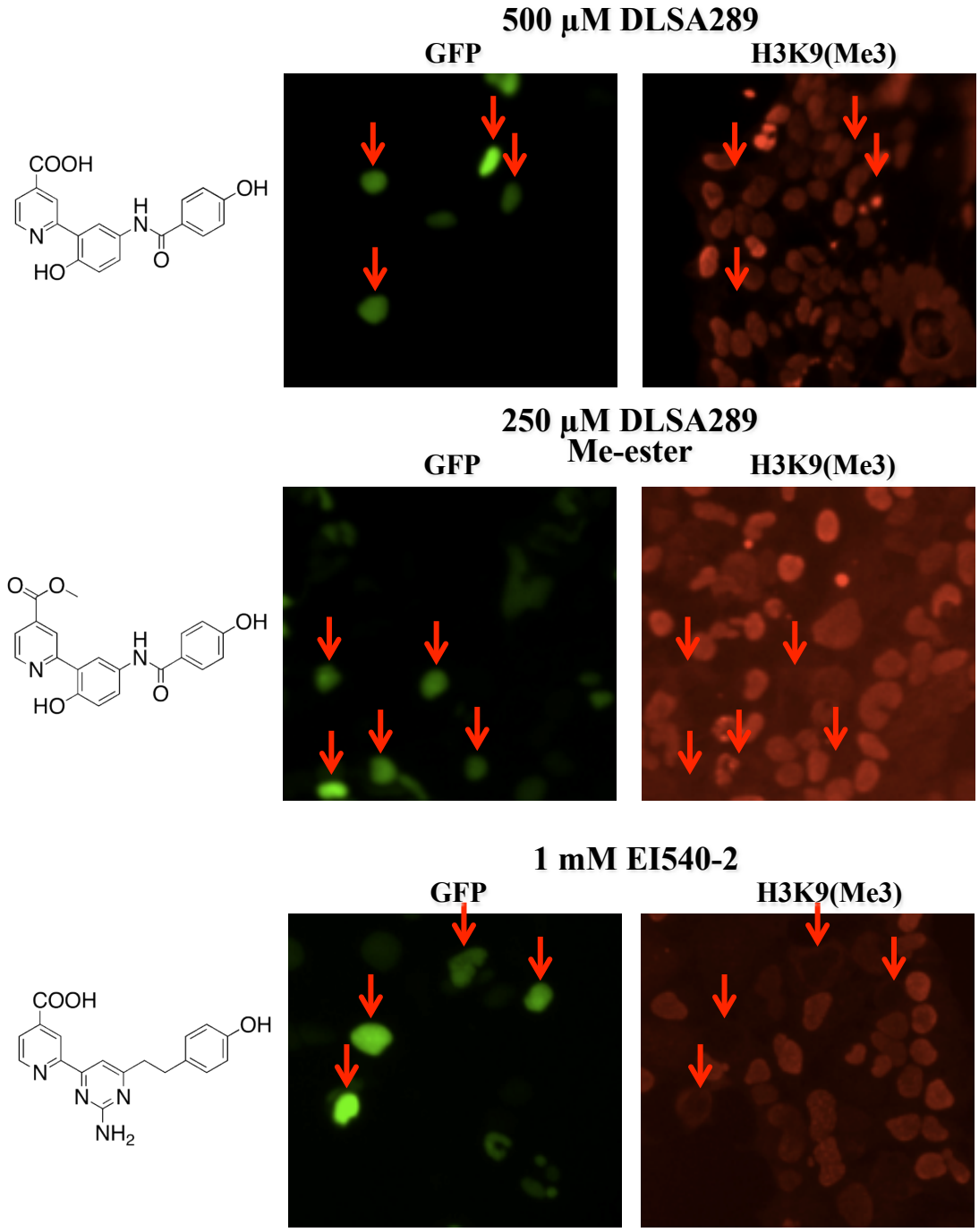

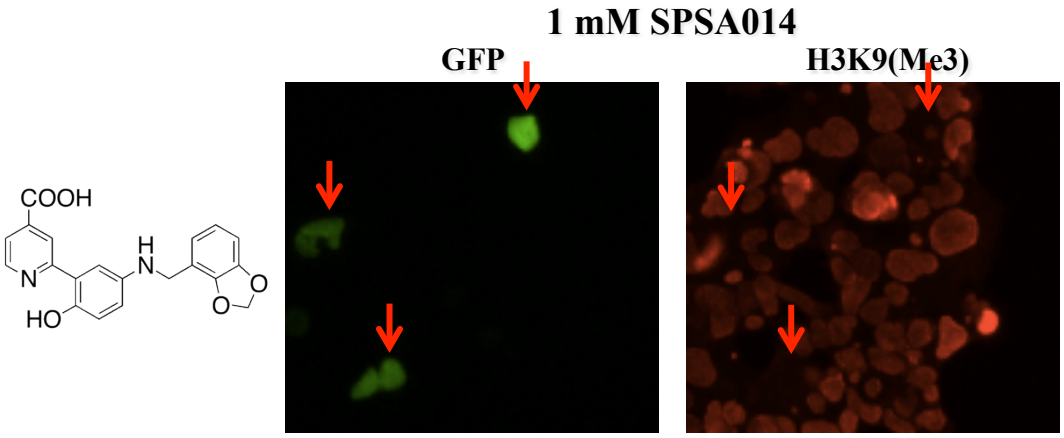
1 mM SPSA014
GFP
H3K9(Me3)
COOH
N
HO
H
N
O
O

V. Stable Expression Assay

Although testing of our inhibitors in both U2OS and HEK293 cells indicates a lack of cell activity, it is possible that this type of transient transfection assay may not be sensitive enough to detect weakly cell active compounds. There are two reasons why we might expect this assay to have low sensitivity: First, we find that only a small amount of KDM4C overexpression is required to almost completely remove the H3K9(Me3) mark. This conclusion is based on the observation that even weakly GFP+ cells have very low H3K9(Me3) signal. As a result, it is apparent that most of the transfected cells express a large excess of KDM4C over what is required to achieve H3K9(Me3) demethylation, and therefore to block this activity and restore basal levels of H3K9(Me3) will require treatment with enough compound to inhibit a large fraction of the active KDM4C. It may therefore be necessary to, for example, treat with sufficient compound to inhibit 90 % or more of KDM4C activity in order to see a 50 % change in H3K9(Me3) signal. The result of this requirement will be an increase in the apparent cellular IC_{50}, potentially masking inhibitor activity in cells. Second, large variability in KDM4C expression levels from cell to cell make quantification difficult, as each cell must be evaluated individually for both KDM4C expression and levels of H3K9(Me3). This requirement for visual analysis may make small changes in H3K9(Me3) levels difficult to detect, again potentially masking inhibitor activity in cells.

In order to address both concerns, we sought to develop an assay based on stable, inducible expression of KDM4C. Such a system would result in consistent expression levels across all cells, and by adjusting the induction strength the

expression level could be tuned to the minimal amount necessary for H3K9(Me3) demethylation, thereby increasing sensitivity. Such a system has already been developed for inducible expression of randomly integrated full-length KDM4A,B and C in U2OS cells, with robust demethylation of H3K9(Me3) and H3K36(Me3). [117] We decided to use a Flp-FRT based system that allows a gene of interest along with a Doxycycline inducible promoter and a hygromycin resistance cassette to be inserted into a cell line engineered with an FRT recombination site. [118] We used an FRT-containing HEK293 cells to make four different cell lines stably expressing KDM4C: One expressing the catalytic domain alone (aa 1-420), another expressing the catalytic domain fused to the N-terminal of GFP, a third expressing full-length KDM4C, and a final one expressing full-length KDM4C fused to the N-terminal of GFP. First, we analyzed these cells for KDM4C expression, both by fluorescence microscopy to look for the presence of GFP in the case of the GFP fusion constructs, and by anti-KDM4C antibody (**Figure 8**). Both by fluorescence microscopy (**Figure 8, A**) and by anti-KDM4C antibody (**Figure 8, B**), we see robust expression of KDM4C in response to Doxycycline treatment.

Figure 8: Analysis of Stable KDM4C Expression in HEK293 Cells

A) Fluorescence microscopy to assess KDM4C-GFP expression before and after induction with 1 µg/mL Doxycycline. B) Anti-KDM4C antibody to assess KDM4C expression before and after induction with 1 µg/mL Doxycycline.

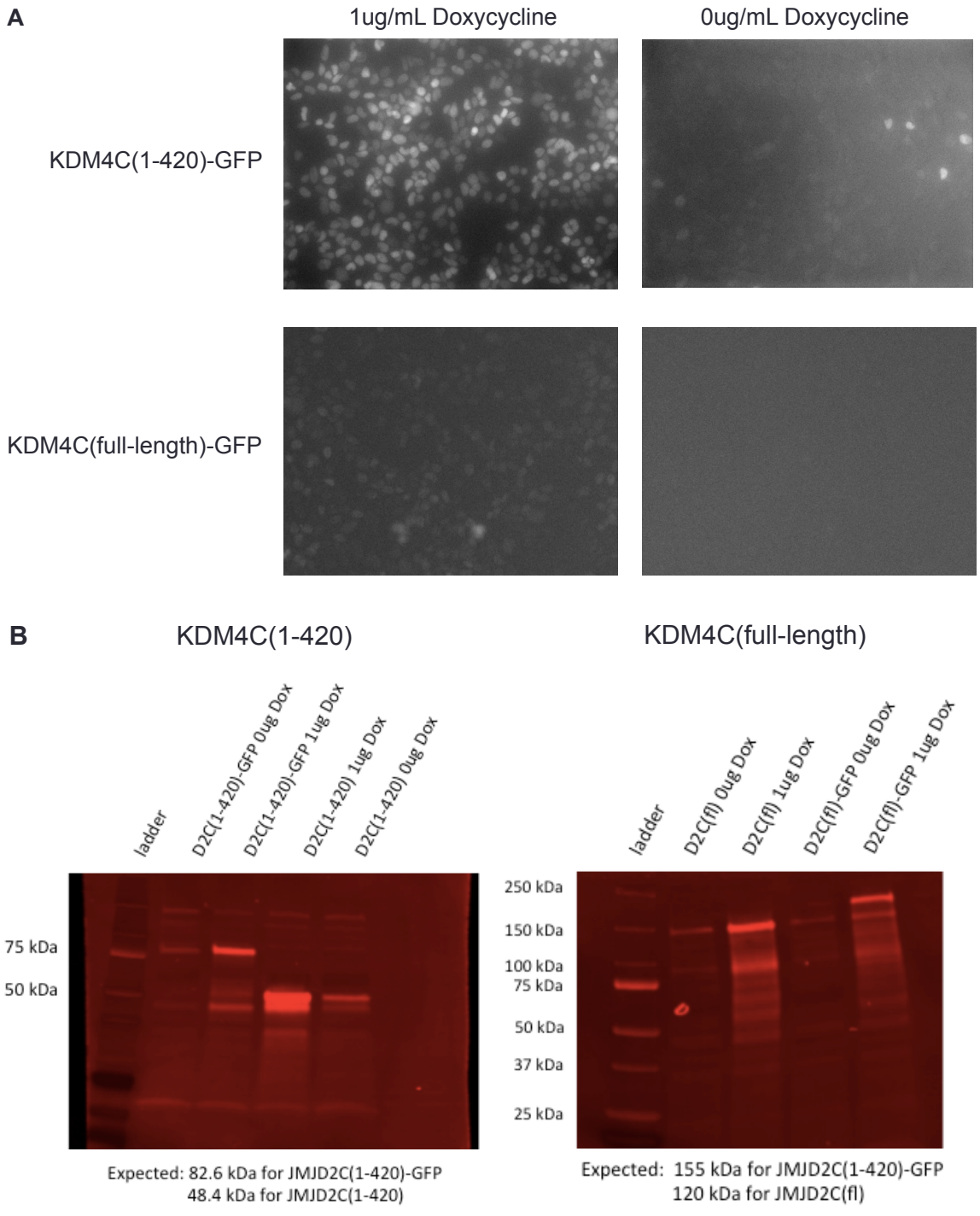

Next, we assessed changes in H3K9(Me3) levels upon KDM4C(1-420) and KDM4C(1-420)-GFP induction (**Figure 9**). We tried treating with a high concentration of Doxycycline for a variable amount of time, looking for the extent of H3K9(Me3) demethylation at each time point by western blot of cellular lysate. When we quantified the data, comparing the amount of H3K9(Me3) signal at different times post-induction normalized to histone H4 as a loading and processing control, we found essentially no change or trend in H3K9(Me3) signal (**Figure 9, B**). The results from a time course of induction using KDM4C(full-length) and KDM4C(full-length)-GFP were similar (data not shown).

Next, we tried both a range of induction strength and inhibition of KDM4C with a variable concentration of DMOG (**Figure 10**). By monitoring for KDM4C(1-420)-GFP and KDM4C(full-length)-GFP expression by fluorescence microscopy, we found that there is full induction of KDM4C expression above at least 1 ng/mL Doxycycline treatment. We therefore sought to probe the effect of lower concentrations of Doxycycline on KDM4C induction. Using a range of Doxycycline concentration from 1 ug/mL to 1 fg/mL, we saw no change in levels of H3K9(Me3) (**Figure 10**). We also attempted to modulate H3K9(Me3) levels by inhibiting KDM4C with DMOG, a molecule which we know to be active in HEK293 cells based on earlier experiments using the transient transfection protocol. Treatment with up to 10 mM DMOG did not change H3K9(Me3) levels (**Figure 10**).

Figure 9: Analysis of H3K9(Me3) Upon KDM4C Induction

HEK293 cells with stably integrated Doxycycline inducible KDM4C. Samples are probed with anti-H3K9(Me3) antibody (band ~ 17 kDa) and anti-H4 antibody as a loading control (band ~ 14 kDa). A) Timecourse from 7-93 hours of induction with 1 ug/mL Doxycycline or blank induction. B) Quantification of A, plotting the time versus the ratio of H3K9(Me3) signal in the induced to the uninduced sample, normalized to H4 loading control.

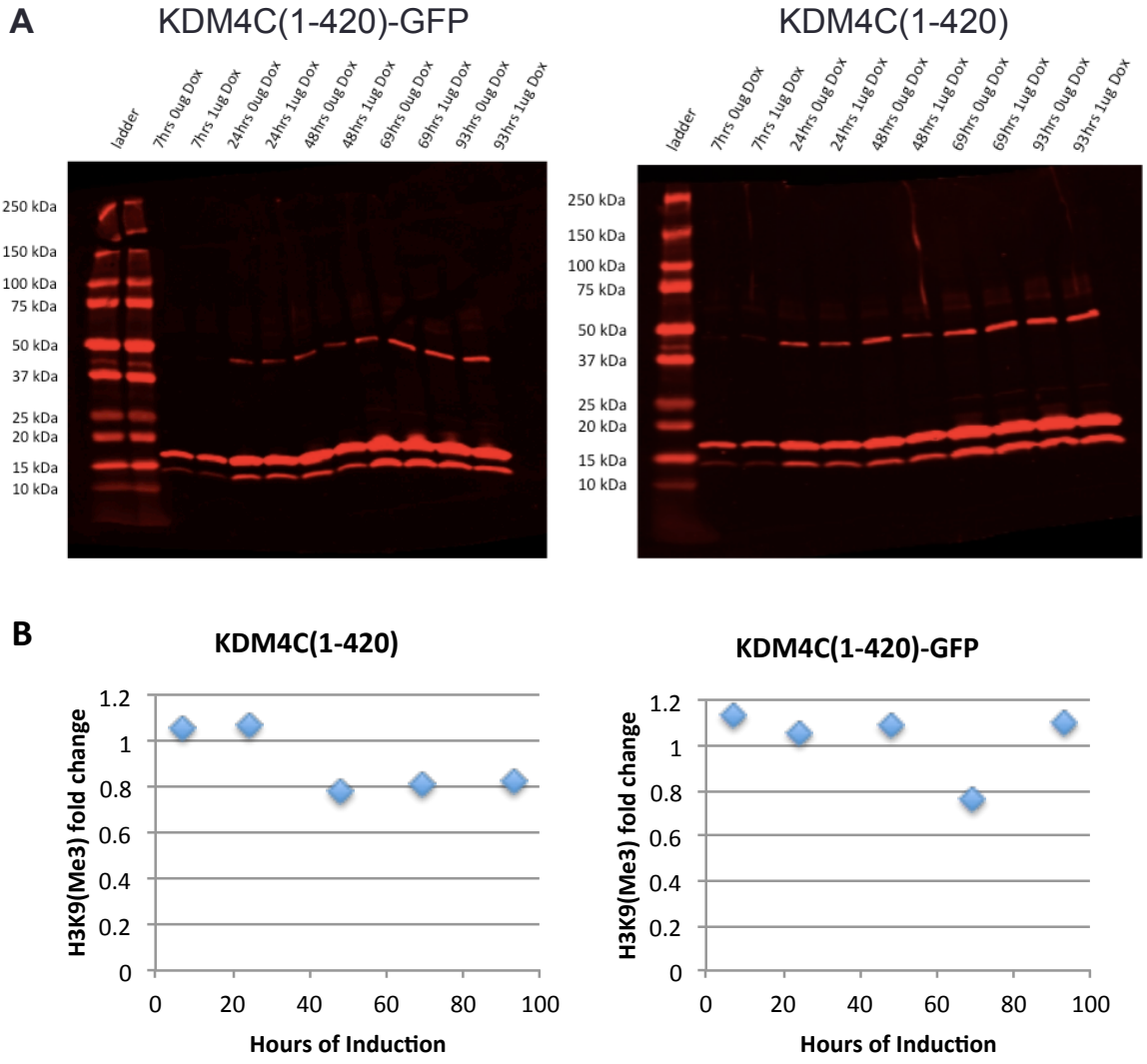

Figure 10: Analysis of H3K9(Me3) Upon KDM4C Induction and Inhibition

HEK293 cells with stably integrated Doxycycline inducible KDM4C. Samples are probed with anti-H3K9(Me3) antibody (band ~ 17 kDa) and anti-H4 antibody (band ~ 14 kDa). Induction is for 48 hours prior to analysis.

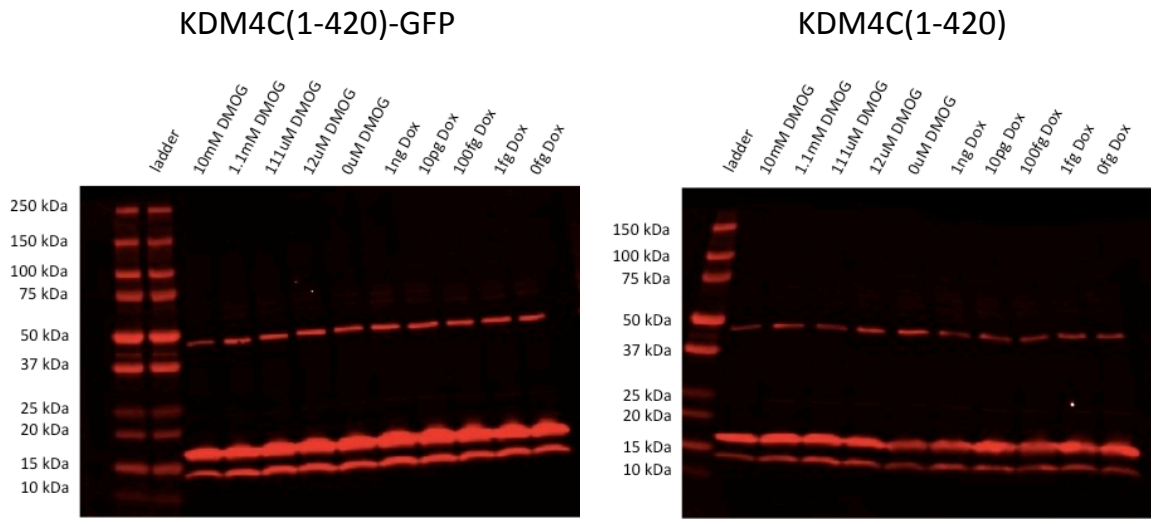

Altogether, these results show that stable, inducible expression of KDM4C in HEK293 cells using the Flp-FRT system is not amenable for use as a system to test KDM4C inhibition. The major requirement for such a system is robust demethylation of H3K9(Me3), which we do not see in this case. What might be the cause? Given the fact that a similar system has already been developed and used successfully, [117] it is useful to consider the differences between the published system and our system. There are two main differences: first, our system has been developed in HEK293 cells while the published system was developed in U2OS cells. It is possible that differences between the cell lines account for the lack of demethylation we observe, although transient transfection of KDM4C into HEK293 cells resulted in robust demethylation (**Figure 7**), making this perhaps less likely. Second, and more likely, is that the procedure used to generate the published cell lines, involving selection from cells with randomly integrated KDM4 for clones exhibiting demethylation, allowed for generation of cell lines with high levels of KDM4 expression capable of robust demethylation. Our cell lines likely did not express KDM4C at a high enough level to achieve measurable demethylation. If this is the case, it may be worthwhile to try other methods, such as the published procedure, to stably express KDM4C at higher levels.

Although this system does not work for the intended purpose, we believe that it may be applicable to ongoing efforts to identify KDM4C target loci. These efforts have been complicated by a lack of high-quality KDM4C antibodies, a problem that could potentially be addressed by using epitope tagged KDM4C. However, as we observe in the transient transfection assay, overexpression of KDM4C results in global H3K9(Me3) demethylation, implying mis-localization of KDMC. It is possible that the

low level overexpression that we find in our stable expression system combined with a lack of global demethylation indicates correct localization of KDM4C. We may therefore be able to use this system, if engineered with an epitope tag, to map KDM4C binding sites across the genome. Efforts to construct this system are ongoing.

VI. Bioisosteres of Carboxylic Acid

Another strategy to facilitate passage of charged small molecules across cell membranes is to replace the charged group with a less polar, but chemically similar moiety. These bioisosteres can sometimes retain key interactions mediated by the charged group while increasing hydrophobicity. Work by Dan Le suggested that out of a small panel of bioisosteres, a hydroxyl group seemed to retain significant potency against KDM4C when tested using the TR-FRET assay with 2 μM αKG. We therefore sought to extend these preliminary findings by synthesizing a small panel of hydroxyl bioisostere derivatives (**Scheme 2**). Unfortunately, neither derivative made with a hydroxyl bioisostere was active against KDM4C as assayed by TR-FRET using 50 μM αKG, up to the highest concentrations tested (**Table 1**).

Scheme 2: Hydroxyl Bioisostere Synthesis

A) Acylation of 4-amino-2-bromophenol with an acid chloride or acetic anhydride affords the desired amides. B) Miyaura borylation of the amide followed by Suzuki-Miyaura coupling of 2-bromopyridin-4-ol with the crude arylboronic acid pinacol ester affords the desired derivative.

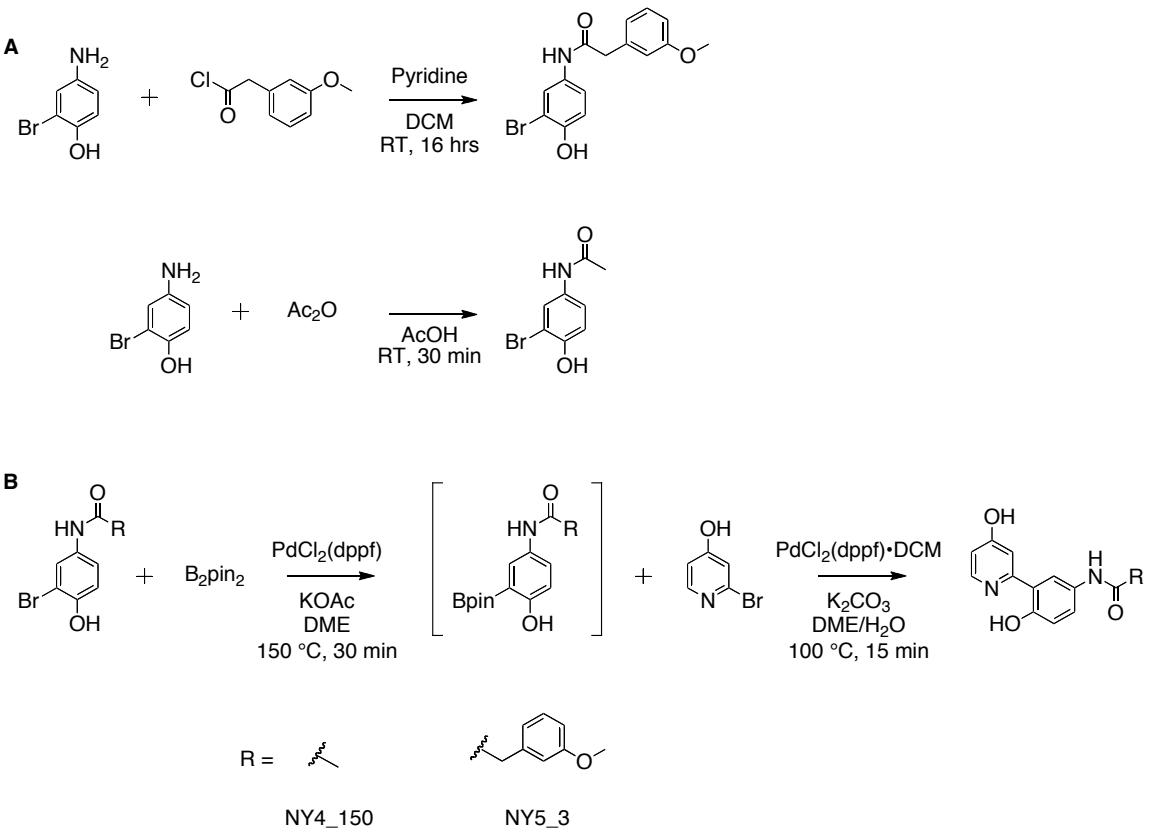

Table 1: *In Vitro* Inhibition of KDM4C by Hydroxyl Bioisosteres

TR-FRET inhibition assays showing IC_{50} values for hydroxyl isosteres of hybrid scaffold derivatives, investigating the effect of the hydroxyl isostere on inhibition of KDM4C. αKG concentration is 50 μM.

Compound	IC_{50}, μM
NY4_150 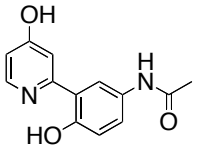	>200
NY5_3 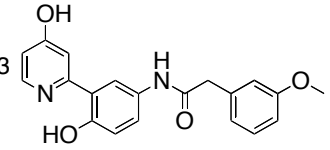	>200

VII. Exploring the Physiological Role of KDM4C-Mediated Demethylation

Although it is important to develop simplified cellular systems in which to test our inhibitors for cell activity, our ultimate goal is to use KDM4 inhibitors to explore the physiological role of KDM4-mediated demethylation. Doing so requires identifying cellular phenotype(s) driven by KDM4 activity. Specifically, as many reports suggest a role for the KDM4 subfamily of histone lysine demethylases in promoting transcriptional activation by removing the transcriptionally repressive H3K9(Me3) mark, [35,36,55] we have tried to identify a system in which this mechanism seems to be functional. Importantly, a direct catalytic role of KDM4 enzymes in transcriptional activation must be distinguished from two potentially confounding situations: First, it is possible that KDM4 enzymes may in some cases serve a scaffolding role to recruit or stabilize other proteins or complexes associated with chromatin. In this case, knockdown of KDM4 enzymes may affect gene transcription even though the KDM4 enzymes play no direct catalytic role. Secondly, changes in the transcription in any given gene upon knockdown of a KDM4 enzyme may be due to secondary effects. For example, a KDM4 enzyme may directly regulate the expression of a transcription factor that in turn regulates many other genes. Again, knockdown of KDM4 enzymes would affect transcription of these secondary genes despite a lack of direct transcriptional control. While knockdown of KDM4 enzymes would be expected to identify direct target genes as well as genes that fit both confounding situations, inhibition with a small molecule would theoretically only modulate transcription of direct target genes.

We therefore sought to identify examples in the literature of direct target genes transcriptionally controlled by KDM4 enzymes. These genes are identified by observing transcriptional changes upon knockdown in a KDM4 enzyme as well as changes in promoter H3K9(Me3). Several examples were found, and we decided to pursue one: a report of KDM4C as a coactivator of the androgen receptor (AR) in a prostate cancer cell line, with knockdown of KDM4C causing decreased proliferation, decreased expression of AR target genes, and concomitant increase in promoter H3K9(Me3) at two AR target genes. [36]

We first attempted to validate the reported results. We were able to achieve robust knockdown of KDM4C in LNCaP cells, the same prostate cancer cell line used in the reference publication, with transfected siRNA (**Figure 11, A**). Treatment of LNCaP cells with the AR agonist R1881 resulted in robust expression of the AR target gene *PSA* (**Figure 11, B**). However, knockdown of KDM4C did not abrogate AR-mediated *PSA* expression, contrary to what was reported (**Figure 11, B**). One possible explanation of this discrepancy is that while we used pooled siRNA to knockdown KDM4C expression, the authors of the reference report used a shRNA. Although we achieve good knockdown at the mRNA level (**Figure 11A**), we were unable to determine knockdown at the protein level due to the lack of an anti-KDM4C antibody at the time these experiments were performed. In the reference report, protein knockdown is shown. Now that such an antibody is available, it may be worthwhile to return to this experiment to confirm protein knockdown using our reagent, or use the published shRNA for knockdown.

Figure 11: Validation of Published Example of KDM4C Target Gene

Testing KDM4C coactivation of AR-mediated *PSA* expression. A) Relative *KDM4C* expression upon treatment with KDM4C-targeted siRNA (kd) or control siRNA (control). B) *PSA* expression upon treatment with KDM4C-targeted siRNA (kd) or control siRNA (control). Blue bar = treatment with 10 nM R1881; red bar = control treatment.

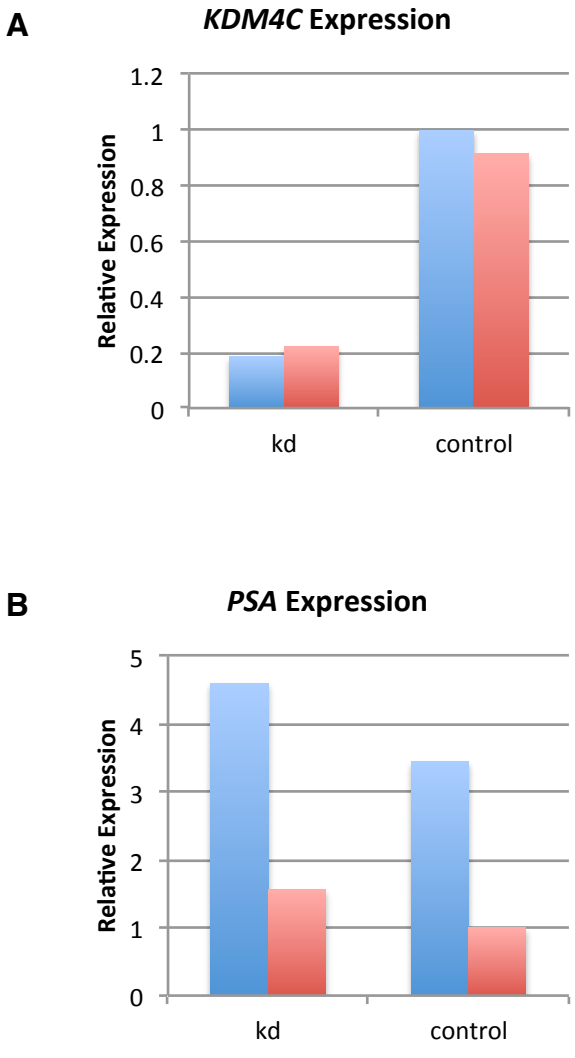

VIII. Conclusion

In conclusion, we have attempted by several methods to make our KDM4 inhibitors cell active, and to develop assays to measure cell activity. Transient transfection assays in two cell types indicate a lack of cell activity for the several scaffold variants, derivatives, and esters tested. However, there remains the possibility that one or more of these compounds may be weakly cell active below the level detectable by the available transient transfection assays. To address this concern we attempted to develop a stable expression assay, but unfortunately this effort was unsuccessful. It is likely that expression of KDM4C was insufficient to achieve robust global H3K9(Me3) demethylation. We do, however, hope that this assay may be useful in the future to study localization of KDM4C. Finally, we were unable to validate a published report of KDM4C-mediated transcriptional activation in a prostate cancer cell line, and this discrepancy may be due to a difference in the reagent used to achieve gene knockdown.

Overall, more work is needed to investigate the cellular activity of KDM4 inhibitors. This work may require the development of more sensitive assays, such as another type of stable expression assay, or additional optimization of the structure of our inhibitors for cell permeability or some other property negatively impacting cell activity, or the identification of entirely new scaffolds. Whatever direction this effort takes, we hope that the assays and expertise developed over the course of the work presented here will facilitate the process.

IX. Materials and Methods

General Methyl Esterification Procedure

To a 20 mL vial is added approximately 5 mg KDM4 inhibitor, 900 uL DMF, 100 uL MeOH, and 40 uL 2 M trimethylsilyldiazomethane (0.08 mmol). The vial is loosely capped and stirred at room temperature for 30 minutes, followed by addition of 5 uL glacial acetic acid (Fisher) (0.087 mmol) and stirring at room temperature for an additional 30 minutes. Solvent is then evaporated under a stream of air, and the crude reaction is purified by HPLC (20 – 80 % gradient of acetonitrile in H_2O + 0.1 % TFA).

DLSA289 Me-ester

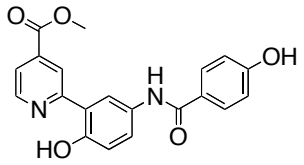

Molecular Weight: 364.35

General methyl esterification procedure was carried out with DLSA289 (~5 mg, ~0.014 mmol). HPLC purification yielded 2.3 mg product (0.006 mmol, 45 %). LCMS $[M-H]^-$ *m/z* = 363.61. 1H NMR (600 MHz, Methanol-d4) δ 8.76 (dd, J = 5.2, 0.9 Hz, 1H), 8.58 (s, 1H), 8.37 – 8.32 (m, 1H), 7.92 – 7.85 (m, 3H), 7.60 (dd, J = 8.8, 2.6 Hz, 1H), 6.97 (d, J = 8.9 Hz, 1H), 6.92 – 6.86 (m, 1H), 4.01 (s, 3H).

DLSA286 Me-ester

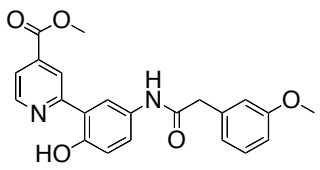

Molecular Weight: 392.40

General methyl esterification procedure was carried out with DLSA286 (~5 mg, 0.013 mmol). HPLC purification yielded 1.1 mg product (0.0028 mmol, 22 %). 1H NMR (600 MHz, Methanol-d4) δ 8.73 (dd, J = 5.2, 0.9 Hz, 1H), 8.52 (s, 1H), 8.23 (d, J = 2.5 Hz, 1H), 7.87 (dd, J = 5.2, 1.4 Hz, 1H), 7.46 (dd, J = 8.8, 2.5 Hz, 1H), 7.28 – 7.21 (m, 1H), 6.98 – 6.95 (m, 2H), 6.92 (d, J = 8.8 Hz, 1H), 6.85 – 6.81 (m, 1H), 3.81 (s, 3H).

NY3_54

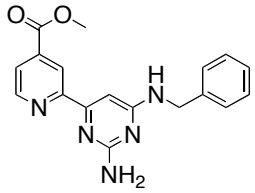

Molecular Weight: 335.36

General methyl esterification procedure was carried out with NY3_33 (~1.3 mg, 0.004 mmol). HPLC purification yielded 0.86 mg product (0.0026 mmol, 64 %). LCMS $[M+H]^+$ *m/z* = 336.27. 1H NMR (400 MHz, Methanol-d4) δ 8.96 (dd, J = 5.0, 0.9 Hz, 1H), 8.54 (t, J = 1.2 Hz, 1H), 8.11 (dd, J = 5.0, 1.4 Hz, 1H), 7.46 – 7.27 (m, 4H), 6.89 (s, 1H), 4.76 (s, 2H), 4.01 (s, 3H).

NY4_52

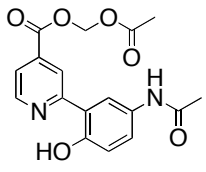

Molecular Weight: 344.32

To a 20 mL vial was added DLSA208 (9.7 mg, 0.036 mmol), DMF (1mL), triethylamine (24.8 uL, 0.178 mmol), and bromomethyl acetate (10.5 uL, 0.107 mmol), and stirred at room temperature for 45 minutes. The reaction was then diluted in 10 mL H_2O, and extracted three times with 10 mL ethyl acetate. The organic fractions were combined, washed with 20 mL 5 % citric acid, then with 20 mL saturated NaCl, then dried over $MgSO_4$, then filtered and concentrated under reduced pressure. The crude reaction was dissolved in 10 mL of 1:1:1 H_2O, DMSO, and methanol, then purified by HPLC (0.1 % TFA, acetonitrile/water gradient: 0-10 min, 40 % B; 10-35 min, 40-100 % B; 35-45 min, 100 % B), yielding 7.0 mg product (0.02 mmol, 57 %). 1H NMR (600 MHz, Acetonitrile-d3) δ 8.75 (dd, J = 5.2, 0.9 Hz, 1H), 8.40 (d, J = 1.3 Hz, 1H), 8.21 (d, J = 2.6 Hz, 1H), 7.84 (dd, J = 5.2, 1.5 Hz, 1H), 7.58 (s, 1H), 7.45 (dd, J = 8.8, 2.5 Hz, 1H), 6.92 (d, J = 8.8 Hz, 1H), 5.99 (s, 3H), 2.11 (s, 4H), 2.07 (d, J = 2.6 Hz, 4H).

General Alkyl Esterification Procedure

To a 20 mL vial is added approximately 5 mg KDM4 inhibitor, 1.4 equivalents 1-Ethyl-3-(3-dimethylaminopropyl)carbodiimide, 0.2 equivalents 4-Dimethylaminopyridine, 1.5-6 equivalents n-alkyl alcohol, and 2 mL THF. The reaction is stirred for 20 hours at room temperature, followed by partitioning between 10 mL H_2O and 10 mL ethyl acetate. The H_2O fraction is extracted three times with 10 mL ethyl acetate. The combined organic fractions are then washed with 20 mL 5 % citric acid, followed by 20 mL saturated sodium bicarbonate, followed by 20 mL saturated sodium chloride. The organic fraction is then dried over $MgSO_4$, filtered, and

concentrated under reduced pressure. The crude reaction is then purified by flash silica gel column chromatography or HPLC.

NY4_55

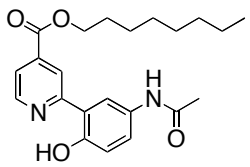

Molecular Weight: 384.47

General alkylesterification procedure was carried out with DLSA208 (8.4 mg, 0.031 mmol), and 1-octanol (Acros) (7.26 uL, 0.046 mmol). Flash silica gel column chromatography (1:2 ethyl acetate to hexanes) yielded 2.5 mg product (0.0065 mmol, 21 %). 1H NMR (600 MHz, Acetonitrile-d3) δ 13.53 (s, 1H), 8.72 (dd, J = 5.2, 0.9 Hz, 1H), 8.39 (ddd, J = 1.4, 1.0, 0.5 Hz, 1H), 8.24 (d, J = 2.6 Hz, 1H), 7.82 (dd, J = 5.2, 1.4 Hz, 1H), 7.43 (dd, J = 8.8, 2.5 Hz, 1H), 6.90 (d, J = 8.8 Hz, 1H), 4.38 (t, J = 6.6 Hz, 2H), 2.06 (s, 3H), 1.83 – 1.75 (m, 2H), 1.51 – 1.44 (m, 2H), 1.30 (s, 9H), 0.90 – 0.86 (m, 3H).

NY4_98

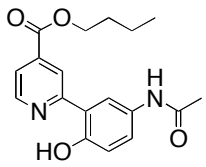

Molecular Weight: 328.36

General alkylesterification procedure was carried out with DLSA208 (13.7 mg, 0.05 mmol), and 1-butanol (27.4 uL, 0.3 mmol). HPLC purification (0.1 % TFA,

methanol/water gradient: 0-6 min, 10 % B; 6-36 min, 10-100 % B; 36-46 min, 100 % B), yields 5.0 mg product (0.015 mmol, 33 %). LCMS $[M+H]^+$ *m/z* = 329.70.

NY4_81

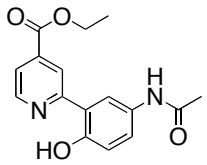

Molecular Weight: 300.31

General alkylesterification procedure was carried out with DLSA208 (4 mg, 0.015 mmol), and ethanol (8.76 uL, 0.15 mmol). Flash silica gel column chromatography (3:2 ethyl acetate to hexanes), followed by HPLC purification (0.1 % TFA, methanol/water gradient: 0-6 min, 20 % B; 6-36 min, 20-100 % B; 36-46 min, 100 % B), yields 1.3 mg product (0.0043 mmol, 29 %). LCMS $[M+H]^+$ *m/z* = 301.66. 1H NMR (600 MHz, Methanol-d4) δ 8.75 (dd, J = 9.0, 5.1 Hz, 1H), 8.51 (d, J = 8.0 Hz, 1H), 8.26 – 8.18 (m, 1H), 7.88 (t, J = 7.1 Hz, 1H), 7.49 – 7.41 (m, 1H), 6.93 (t, J = 8.8 Hz, 1H), 4.55 – 4.41 (m, 3H), 2.20 – 2.08 (m, 3H), 1.50 – 1.38 (m, 3H).

General Secondary Ester Synthesis Procedure

To a 20 mL vial add ~5 mg DLSA208 (0.018 mmol), carbonyldiimidazole (32 mg, 0.2 mmol), and 1 mL DMF. Stir at room temperature for one hour. Then add 2° alcohol (0.25 mmol), 1,8-Diazabicycloundec-7-ene (24.9 µL, 0.17 mmol), and 4-Dimethylaminopyridine (2 mg, 0.017 mmol), and stir at 40 °C for 18 hours. Evaporate DMF under a stream of air, and purify the crude reaction by HPLC (0.1 % TFA,

acetonitrile/water gradient: 0-6 min, 10 % B; 6-36 min, 10-100 % B; 36-46 min, 100 % B) to yield pure product.

NY4_118

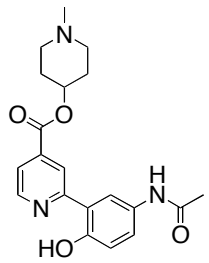

Molecular Weight: 369.41

General secondary ester synthesis procedure was carried out with DLSA208 (10 mg, 0.037 mmol) and *N*-methylpiperidine-4-ol (29.4 μL, 0.25 mmol). HPLC purification yields 7.6 mg (0.021 mmol, 51 %) pure product. LCMS $[M+H]^+$ *m/z* = 370.74.

NY4_120

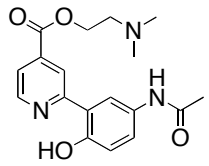

Molecular Weight: 343.38

General secondary ester synthesis procedure was carried out with DLSA208 (5.5 mg, 0.02 mmol) and *N,N*-dimethylamino ethanol (25.2 μL, 0.25 mmol). HPLC purification yields 4.7 mg (0.014 mmol, 68 %) pure product. LCMS $[M+H]^+$ *m/z* = 344.68. 1H NMR (600 MHz, Acetonitrile-d3) δ 8.73 (d, J = 5.2 Hz, 1H), 8.44 (s, 1H), 8.22 (d, J = 2.5 Hz, 1H), 7.93 (d, J = 4.9 Hz, 1H), 7.48 (d, J = 8.3 Hz, 1H), 6.91 (d, J = 8.8 Hz, 1H), 4.69 (d, J = 5.3 Hz, 2H), 3.51 (d, J = 4.9 Hz, 2H), 2.92 (s, 6H), 2.06 (s, 3H).

NY4_121

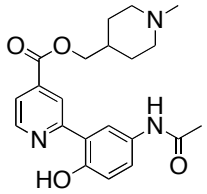

Molecular Weight: 383.44

General secondary ester synthesis procedure was carried out with DLSA208 (5.5 mg, 0.02 mmol) and *N*-methyl-4-piperidine methanol (34 µL, 0.25 mmol). Flash silica column chromatography (ethyl acetate + 10 % methanol + 2 % triethylamine) followed by HPLC purification yields 1.5 mg (0.004 mmol, 19 %) pure product. LCMS $[M+H]^+$ *m/z* = 384.77.

***N*-(3-bromo-4-hydroxyphenyl)-2-(3-methoxyphenyl)acetamide**

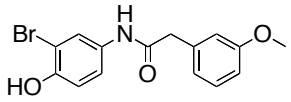

Molecular Weight: 336.18

To a 20 mL pressure-release vial add 4-amino-2-bromophenol (38.5 mg, 0.205 mmol), 3-methylphenyl acetyl chloride (32.3 uL, 0.207 mmol), pyridine (17 uL, 0.208 mmol), and DCM (3 mL). Stir at room temperature for 18 hours, then add additional 3-methylphenyl acetyl chloride (32.3 uL, 0.207 mmol) and pyridine (17 uL, 0.208 mmol), and stir at room temperature for an additional 90 minutes. Carefully dilute the reaction in 5 mL H_2O, then extract three times with 5 mL DCM. Combine the organic fractions and wash twice with 5 % citric acid, then with saturated sodium bicarbonate,

then with saturated sodium chloride, then concentrate under reduced pressure. Flash silica gel chromatography (1:2 ethyl acetate to hexanes) yields 55.5 mg product (0.165 mmol, 40 %). LCMS $[M-H]^-$ *m/z* = 334.61/336.52.

_N_-(3-bromo-4-hydroxyphenyl)acetamide

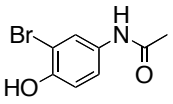

Molecular Weight: 230.06

To a 20 mL vial add 4-amino-2-bromophenol (380 mg, 2 mmol), acetic anhydride (217 uL, 2.3 mmol), and glacial acetic acid (2 mL). Stir at room temperature for 30 minutes, then quench by addition of 10 N NaOH until formation of a persistent grey/brown precipitate (~4 mL, 40 mmol). Extract three times with 5 mL ethyl acetate. Combine the organic fractions and wash with saturated sodium chloride, then dry over $MgSO_4$, then filter and concentrate under reduced pressure. Reaction yields 375 mg product (1.63 mmol, 82 %). LCMS $[M+H]^+$ *m/z* = 230.49/232.48.

NY4_150

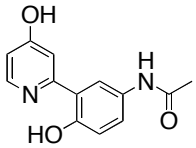

Molecular Weight: 244.25

To a 10 mL microwave vial add *N*-(3-bromo-4-hydroxyphenyl)acetamide (57.5 mg, 0.25 mmol), bispinacolato diboron (Oakwood) (76 mg, 0.3 mmol), potassium acetate (74 mg, 0.75 mmol), $PdCl_2$(dppf) (5.3 mg, 0.0075 mmol), and 5 mL DME. Microwave

for 15 minutes at 150 °C. Pass the crude reaction through a 0.22 μm filter and use in the next step without further purification.

To a 10 mL microwave vial add the crude reaction from the previous step, 4-hydroxy-2-bromopyridine (17.4 mg, 0.1 mmol), potassium carbonate (35 mg, 0.25 mmol), and 1 mL H_2O. Sparge the reaction with argon for 15 minutes, then add $PdCl_2$(dppf)•DCM (8.2 mg, 0.01 mmol). Microwave for 30 minutes at 100 °C, then dilute in 10 mL H_2O and wash three times with 10 mL ethyl acetate. Extract the combined organic fractions with 10 mL 5 % citric acid followed by 10 mL saturated sodium bicarbonate followed by 10 mL saturated sodium chloride. Combine the aqueous layers and concentrate under reduced pressure, then purify by HPLC (0.1 % TFA, acetonitrile/water gradient: 0-8 min, 10 % B; 8-33 min, 10-100 % B; 33-40 min, 100 % B), yields 3.8 mg product (0.016 mmol, 6 % over two steps). LCMS $[M-H]^-$ *m/z* = 243.56. 1H NMR (400 MHz, Methanol-d4) δ 8.38 (d, J = 6.9 Hz, 1H), 7.93 (d, J = 2.6 Hz, 1H), 7.44 (dd, J = 8.8, 2.6 Hz, 1H), 7.40 (d, J = 2.5 Hz, 1H), 7.12 (dd, J = 6.9, 2.6 Hz, 1H), 7.01 (d, J = 8.8 Hz, 1H), 2.13 (s, 4H).

NY5_3

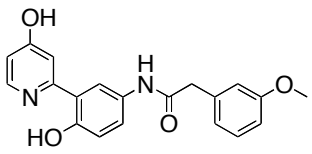

Molecular Weight: 350.37

To a 10 mL microwave vial add *N*-(3-bromo-4-hydroxyphenyl)-2-(3-methoxyphenyl)acetamide (55.5 mg, 0.165 mmol), bispinacolato diboron (Oakwood)

(127 mg, 0.495 mmol), potassium acetate (49 mg, 0.495 mmol), $PdCl_2$(dppf) (3.6 mg, 0.005 mmol), and 3 mL DME. Microwave for 15 minutes at 150 °C. Pass the crude reaction through a 0.22 μm filter and use in the next step without further purification.

To a 10 mL microwave vial add the crude reaction from the previous step, 4-hydroxy-2-bromopyridine (29 mg, 0.17 mmol), potassium carbonate (57 mg, 0.41 mmol), and 600 μL H_2O. Sparge the reaction with argon for 15 minutes, then add $PdCl_2$(dppf)•DCM (13.5 mg, 0.017 mmol). Microwave for 30 minutes at 100 °C, then dilute in 30 mL H_2O and extract three times with 10 mL ethyl acetate. Wash the combined organic fractions with 10 mL 5 % citric acid followed by 10 mL saturated sodium chloride. Combine the aqueous layers and concentrate under reduced pressure, then purify by flash silica gel chromatography (1:1 ethyl acetate to hexanes) followed by HPLC (0.1 % TFA, acetonitrile/water gradient: 0-8 min, 10 % B; 8-33 min, 10-100 % B; 33-40 min, 100 % B), yields 2.6 mg product (0.0074 mmol, 5 % over two steps). LCMS $[M+H]^+$ *m/z* = 351.67. 1H NMR (400 MHz, Methanol-d4) δ 8.38 – 8.33 (m, 1H), 7.94 (dd, J = 2.6, 0.4 Hz, 1H), 7.46 (dd, J = 8.8, 2.6 Hz, 1H), 7.38 (d, J = 2.5 Hz, 1H), 7.23 (d, J = 8.1 Hz, 1H), 7.09 (dd, J = 6.9, 2.6 Hz, 1H), 7.01 (dd, J = 8.9, 0.4 Hz, 1H), 6.96 – 6.91 (m, 2H), 6.87 – 6.81 (m, 1H), 3.79 (s, 3H), 3.65 (s, 2H).

Transient Transfection Assay

Grow U2OS Cells (UCSF Cell Culture Facility) in DMEM low glucose media supplemented with 10 % FBS to > 80 % confluence, then collect using 0.25 % trypsin. Alternatively, grow HEK293 Cells (UCSF Cell Culture Facility) in MEM with Earl's

BSS supplemented with 10 % FBS to > 80 % confluence, then collect using 0.05 % trypsin. Plate 15,000 cells per well on a 96-well glass bottom MatriPlate (GE Healthcare) and incubate 24 hours at 37 °C with 5 % CO_2. Transfect using 10 µL OptiMEM serum free media, 0.4 µL Lipofectamine LTX (Invitrogen), 0.05 µL plus reagent (Invitrogen), and 0.05 µg DNA per well. Incubate cells 4 hours post-transfection, then replace media with 2-fold compound dilution series (maximum 1 % DMSO), and incubate a further 48 hours. Wash cells with ice-cold PBS, fix for 20 minutes with 4 % formaldehyde (Thermo Scientific), then wash three times with ice-cold PBS. Permeabilize for 10 minutes at room temperature with 0.5 % Triton X-100 in PBS. Block 30 minutes at room temperature with 0.5 % Tween-20 and 2 % FBS in PBS. Stain with 1:1000 dilution of anti-H3K9(Me3) antibody (ab8898) in 0.5 % Tween-20 and 2 % FBS in PBS overnight at room temperature, then wash three times with PBS. Stain with 1:1000 dilution of alexafluor 568 goat anti-rabbit antibody and 2 µg/mL DAPI in 0.5 % Tween-20 and 2 % FBS in PBS for 1 hour at room temperature, then wash three times with PBS. Image using FITC and Cy3 filters.

Generation of Doxycycline Inducible KDM4C HEK293 Cells Lines

Grow HEK293 cells with integrated FRT recombination site (gift of Yazmin Carrasco) in DMEM-H21 supplemented with 10 % FBS at 37 °C with 5 % CO_2 to ~ 100 % confluence on a 75 cm^2 flask, then trypsinize with 0.05 % trypsin and plate half on a new 75 cm^2 flask and grow 24 hours. Exchange into 9 mL DMEM-H21 without FBS, then transfect with 2.4 µg KDM4C plasmid, 22 µg pOG44 (Flp recombinase expression plasmid, gift of Yazmin Carrasco), and 60 µL Lipofectamine 2000

(Invitrogen), made to 1.5 mL with OptiMEM serum free media. Incubate 24 hours, then replace media with DMEM-H21 supplemented with 5 % FBS, then incubate an additional 24 hours. Trypsinize cells and plate ½ on a new 75 cm^2 plate, growing in DMEM-21 supplemented with 10 % FBS and 150 µg/mL Hygromycin B. Grow until colonies are visible by eye (~10 days), then trypsinize and split as necessary, growing for one additional week in DMEM-H21 supplemented with 10 % FBS, 150 µg/mL Hygromycin B, and 15 µg/mL Blasticidin. Cells can then be grown and frozen as stocks as necessary.

Analysis of KDM4C Expression by Western Blot

Grow HEK293 cells in DMEM-H21 supplemented with 10 % FBS at 37 °C with 5 % CO_2 to ~ 100 % confluence, then trypsinize with 0.05 % trypsin and plate 200,000 cells per well in a 12-well plate and grow overnight. Remove media and replace with fresh media supplemented with 1 µg/mL Doxycycline or blank, then grow 48 hours. Aspirate media, add 250 µL SDS loading buffer, let sit one minute, then transfer by pipette into an eppendorf tube and keep on ice. Sonicate (Lim Lab) for 7.5 minutes alternating 30 seconds on/30 seconds off, then boil for 10 minutes. Dilute samples 1:10 into SDS loading buffer, then run 30 minutes at 200 V on a 4 – 20 % TGX pre-cast gel (Bio-Rad). Transfer to PVDF membrane using wet transfer technique for 1 hour at 400 mA. Block PVDF membrane with Licor blocking buffer for 1 hour at room temperature. Stain with 1:2000 anti-KDM4C (gift of Lindsey Pack) in Licor blocking buffer supplemented with 0.2 % Tween-20 overnight at 4 °C. Wash three times with TBS + 0.1 % Tween-20 (TBST), then stain with 1:20,000 goat anti-rabbit

IRDye 680LT (Licor 926-68021) in Licor blocking buffer supplemented with 0.2 % Tween-20 for 1 hour at room temperature. Wash five times with TBST, then twice with PBS. Image using Licor scanner (Taunton Lab).

Analysis of H3K9(Me3) Levels by Western Blot

Grow HEK293 cells in DMEM-H21 supplemented with 10 % FBS at 37 °C with 5 % CO_2 to ~ 100 % confluence, then trypsinize with 0.05 % trypsin and plate 200,000 cells per well in a 12-well plate and grow overnight. Remove media and replace with fresh media supplemented with Doxycycline or blank and/or compound dilution (maximum 1 % DMSO), then grow 48 hours. Aspirate media, add 250 µL SDS loading buffer, let sit one minute, then transfer by pipette into an eppendorf tube and keep on ice. Sonicate (Lim Lab) for 7.5 minutes alternating 30 seconds on/30 seconds off, then boil for 10 minutes. Dilute samples 1:10 into SDS loading buffer, then run 30 minutes at 200 V on a 4 – 20 % TGX pre-cast gel (Bio-Rad). Transfer to nitrocellulose using semi-dry technique: 1 hour transfer at 24 V, 300 mA. Block nitrocellulose membrane with Licor blocking buffer for 1 hour at room temperature. Stain with 1:1000 anti-H3K9(Me3) (ab8898) and 1:1000 anti-H4 (Active Motif #39269) in Licor blocking buffer supplemented with 0.2 % Tween-20 overnight at 4 °C. Wash three times with TBST, then stain with 1:20,000 goat anti-rabbit IRDye 680LT (Licor 926-68021) in Licor blocking buffer supplemented with 0.2 % Tween-20 for 1 hour at room temperature. Wash five times with TBST, then twice with PBS. Image using Licor scanner (Taunton Lab).

Growing and Treating LNCaP Cells

Grow LNCaP Cells (UCSF Cell Culture Facility) in RPMI-1640 (ATCC) supplemented with 10 % FBS at 37 °C with 5 % CO_2 on a CellBIND surface flask (Corning) until > 80 % confluent. Make transfection mix consisting of 1.5 µL of 20 µM KDM4C ON-TARGET*plus* siRNA SMART pool (Thermo Scientific) or control pool, 5 µL Lipofectamine LTX (Invitrogen), and 500 µL OptiMEM serum free media, and add this to each well of a 6-well plate and allow to incubate for 20 minutes at room temperature. Trypsinize LNCaP cells with 0.25 % trypsin and add 100,000 cells per well to the transfection mix, in a volume of 2.5 mL RPMI-1640 supplemented with 10 % charcoal-stripped FBS. Incubate 72 hours at 37 °C with 5 % CO_2. Add 10 nM R1881 or blank to each well, and incubate a further 4 hours. Harvest cells by scraping, and collect by centrifugation. Lyse cells by addition of 350 µL RLT buffer (Qiagen) supplemented with 1 % BME. Store at -20 °C.

RT-PCR Analysis of LNCaP Cells

Apply lysates to QIAShredder columns (Qiagen) and process according to instructions. Purify RNA using RNEasy Mini Kit (Qiagen) according to instructions. Synthesize 1 µg cDNA using iScript cDNA synthesis kit (Bio-Rad) according to instructions. Dilute cDNA with 175 µL nuclease free H_2O, and add 5.2 µL diluted cDNA per well of a 96-well pcr plate. Add 4.8 µL of 5.2 µM forward and reverse primer to the appropriate wells, then add 10 µL 2x SYBR Green RT-PCR Master Mix (Applied Biosystems). PCR with fluorescence detection is performed according to the

instructions for SYBR Green dye, using a CFX Connect Real-Time System (Bio-Rad, Yamamoto Lab). Analysis of data is by $\Delta\Delta C_t$ method.[119]

Works Cited

1. Bianconi E, Piovesan A, Facchin F, et al. An estimation of the number of cells in the human body. *Ann Hum Biol*. 2013;40(6):463-471.

2. Luger K, Mader AW, Richmond RK, Sargent DF, Richmond TJ. Crystal structure of the nucleosome core particle at 2.8 A resolution. *Nature*. 1997;389(6648):251-260.

3. Bernstein BE, Meissner A, Lander ES. The mammalian epigenome. *Cell*. 2007;128(4):669-681.

4. Li B, Carey M, Workman JL. The role of chromatin during transcription. *Cell*. 2007;128(4):707-719.

5. Song F, Chen P, Sun D, et al. Cryo-EM study of the chromatin fiber reveals a double helix twisted by tetranucleosomal units. *Science*. 2014;344(6182):376-380.

6. Shogren-Knaak M, Ishii H, Sun JM, Pazin MJ, Davie JR, Peterson CL. Histone H4-K16 acetylation controls chromatin structure and protein interactions. *Science*. 2006;311(5762):844-847.

7. Akhtar A, Becker PB. Activation of transcription through histone H4 acetylation by MOF, an acetyltransferase essential for dosage compensation in drosophila. *Mol Cell*. 2000;5(2):367-375.

8. Carrozza MJ, Li B, Florens L, et al. Histone H3 methylation by Set2 directs deacetylation of coding regions by Rpd3S to suppress spurious intragenic transcription. *Cell*. 2005;123(4):581-592.

9. Torres IO, Kuchenbecker KM, Nnadi CI, Fletterick RJ, Kelly MJ, Fujimori DG. Histone demethylase KDM5A is regulated by its reader domain through a positive-feedback mechanism. *Nat Commun*. 2015;6:6204.

10. Jenuwein T, Allis CD. Translating the histone code. *Science*. 2001;293(5532):1074-1080.

11. Bannister AJ, Zegerman P, Partridge JF, et al. Selective recognition of methylated lysine 9 on histone H3 by the HP1 chromo domain. *Nature*. 2001;410(6824):120-124.

12. Nielsen SJ, Schneider R, Bauer UM, et al. Rb targets histone H3 methylation and HP1 to promoters. *Nature*. 2001;412(6846):561-565.

13. Canzio D, Liao M, Naber N, et al. A conformational switch in HP1 releases auto-inhibition to drive heterochromatin assembly. *Nature*. 2013;496(7445):377-381.

14. Lehnertz B, Ueda Y, Derijck AA, et al. Suv39h-mediated histone H3 lysine 9 methylation directs DNA methylation to major satellite repeats at pericentric heterochromatin. *Curr Biol*. 2003;13(14):1192-1200.

15. Lachner M, O'Carroll D, Rea S, Mechtler K, Jenuwein T. Methylation of histone H3 lysine 9 creates a binding site for HP1 proteins. *Nature*. 2001;410(6824):116-120.

16. Tachibana M, Ueda J, Fukuda M, et al. Histone methyltransferases G9a and GLP form heteromeric complexes and are both crucial for methylation of euchromatin at H3-K9. *Genes Dev*. 2005;19(7):815-826.

17. Kooistra SM, Helin K. Molecular mechanisms and potential functions of histone demethylases. *Nat Rev Mol Cell Biol*. 2012;13(5):297-311.

18. Yang L, Lin C, Liu W, et al. ncRNA- and Pc2 methylation-dependent gene relocation between nuclear structures mediates gene activation programs. *Cell*. 2011;147(4):773-788.

19. Chen Z, Zang J, Whetstine J, et al. Structural insights into histone demethylation by JMJD2 family members. *Cell*. 2006;125(4):691-702.

20. Ng SS, Kavanagh KL, McDonough MA, et al. Crystal structures of histone demethylase JMJD2A reveal basis for substrate specificity. *Nature*. 2007;448(7149):87-91.

21. Khoury-Haddad H, Guttmann-Raviv N, Ipenberg I, Huggins D, Jeyasekharan AD, Ayoub N. PARP1-dependent recruitment of KDM4D histone demethylase to DNA damage sites promotes double-strand break repair. *Proc Natl Acad Sci U S A*. 2014;111(7):E728-37.

22. Young LC, McDonald DW, Hendzel MJ. Kdm4b histone demethylase is a DNA damage response protein and confers a survival advantage following gamma-irradiation. *J Biol Chem*. 2013;288(29):21376-21388.

23. Mallette FA, Mattiroli F, Cui G, et al. RNF8- and RNF168-dependent degradation of KDM4A/JMJD2A triggers 53BP1 recruitment to DNA damage sites. *EMBO J*. 2012;31(8):1865-1878.

24. Das PP, Shao Z, Beyaz S, et al. Distinct and combinatorial functions of Jmjd2b/Kdm4b and Jmjd2c/Kdm4c in mouse embryonic stem cell identity. *Mol Cell*. 2014;53(1):32-48.

25. Loh YH, Zhang W, Chen X, George J, Ng HH. Jmjd1a and Jmjd2c histone H3 lys 9 demethylases regulate self-renewal in embryonic stem cells. *Genes Dev*. 2007;21(20):2545-2557.

26. Pedersen MT, Agger K, Laugesen A, et al. The demethylase JMJD2C localizes to H3K4me3-positive transcription start sites and is dispensable for embryonic development. *Mol Cell Biol*. 2014;34(6):1031-1045.

27. Cascante A, Klum S, Biswas M, Antolin-Fontes B, Barnabe-Heider F, Hermanson O. Gene-specific methylation control of H3K9 and H3K36 on neurotrophic BDNF versus astroglial GFAP genes by KDM4A/C regulates neural stem cell differentiation. *J Mol Biol*. 2014;426(20):3467-3477.

28. Strobl-Mazzulla PH, Sauka-Spengler T, Bronner-Fraser M. Histone demethylase JmjD2A regulates neural crest specification. *Dev Cell*. 2010;19(3):460-468.

29. Ye L, Fan Z, Yu B, et al. Histone demethylases KDM4B and KDM6B promotes osteogenic differentiation of human MSCs. *Cell Stem Cell*. 2012;11(1):50-61.

30. Shi L, Sun L, Li Q, et al. Histone demethylase JMJD2B coordinates H3K4/H3K9 methylation and promotes hormonally responsive breast carcinogenesis. *Proc Natl Acad Sci U S A*. 2011;108(18):7541-7546.

31. Kawazu M, Saso K, Tong KI, et al. Histone demethylase JMJD2B functions as a co-factor of estrogen receptor in breast cancer proliferation and mammary gland development. *PLoS One*. 2011;6(3):e17830.

32. Berry WL, Shin S, Lightfoot SA, Janknecht R. Oncogenic features of the JMJD2A histone demethylase in breast cancer. *Int J Oncol*. 2012;41(5):1701-1706.

33. Yang J, Jubb AM, Pike L, et al. The histone demethylase JMJD2B is regulated by estrogen receptor alpha and hypoxia, and is a key mediator of estrogen induced growth. *Cancer Res*. 2010;70(16):6456-6466.

34. Gaughan L, Stockley J, Coffey K, et al. KDM4B is a master regulator of the estrogen receptor signalling cascade. *Nucleic Acids Res*. 2013;41(14):6892-6904.

35. Shin S, Janknecht R. Activation of androgen receptor by histone demethylases JMJD2A and JMJD2D. *Biochem Biophys Res Commun*. 2007;359(3):742-746.

36. Wissmann M, Yin N, Muller JM, et al. Cooperative demethylation by JMJD2C and LSD1 promotes androgen receptor-dependent gene expression. *Nat Cell Biol*. 2007;9(3):347-353.

37. Coffey K, Rogerson L, Ryan-Munden C, et al. The lysine demethylase, KDM4B, is a key molecule in androgen receptor signalling and turnover. *Nucleic Acids Res*. 2013;41(8):4433-4446.

38. Zhang QJ, Chen HZ, Wang L, Liu DP, Hill JA, Liu ZP. The histone trimethyllysine demethylase JMJD2A promotes cardiac hypertrophy in response to hypertrophic stimuli in mice. *J Clin Invest*. 2011;121(6):2447-2456.

39. Zhang D, Yoon HG, Wong J. JMJD2A is a novel N-CoR-interacting protein and is involved in repression of the human transcription factor achaete scute-like homologue 2 (ASCL2/Hash2). *Mol Cell Biol*. 2005;25(15):6404-6414.

40. Huang Y, Fang J, Bedford MT, Zhang Y, Xu RM. Recognition of histone H3 lysine-4 methylation by the double tudor domain of JMJD2A. *Science*. 2006;312(5774):748-751.

41. Black JC, Allen A, Van Rechem C, et al. Conserved antagonism between JMJD2A/KDM4A and HP1gamma during cell cycle progression. *Mol Cell*. 2010;40(5):736-748.

42. Black JC, Manning AL, Van Rechem C, et al. KDM4A lysine demethylase induces site-specific copy gain and rereplication of regions amplified in tumors. *Cell*. 2013;154(3):541-555.

43. Van Rechem C, Black JC, Boukhali M, et al. Lysine demethylase KDM4A associates with translation machinery and regulates protein synthesis. *Cancer Discov*. 2015;5(3):255-263.

44. Young LC, Hendzel MJ. The oncogenic potential of jumonji D2 (JMJD2/KDM4) histone demethylase overexpression. *Biochem Cell Biol*. 2013;91(6):369-377.

45. Berry WL, Janknecht R. KDM4/JMJD2 histone demethylases: Epigenetic regulators in cancer cells. *Cancer Res*. 2013;73(10):2936-2942.

46. Johansson C, Tumber A, Che K, et al. The roles of jumonji-type oxygenases in human disease. *Epigenomics*. 2014;6(1):89-120.

47. Crea F, Sun L, Mai A, et al. The emerging role of histone lysine demethylases in prostate cancer. *Mol Cancer*. 2012;11:52-4598-11-52.

48. Chu CH, Wang LY, Hsu KC, et al. KDM4B as a target for prostate cancer: Structural analysis and selective inhibition by a novel inhibitor. *J Med Chem*. 2014;57(14):5975-5985.

49. Liu Y, Zheng P, Liu Y, et al. An epigenetic role for PRL-3 as a regulator of H3K9 methylation in colorectal cancer. *Gut*. 2013;62(4):571-581.

50. Italiano A, Attias R, Aurias A, et al. Molecular cytogenetic characterization of a metastatic lung sarcomatoid carcinoma: 9p23 neocentromere and 9p23-p24 amplification including JAK2 and JMJD2C. *Cancer Genet Cytogenet*. 2006;167(2):122-130.

51. Yang ZQ, Imoto I, Fukuda Y, et al. Identification of a novel gene, GASC1, within an amplicon at 9p23-24 frequently detected in esophageal cancer cell lines. *Cancer Res*. 2000;60(17):4735-4739.

52. Rui L, Emre NC, Kruhlak MJ, et al. Cooperative epigenetic modulation by cancer amplicon genes. *Cancer Cell*. 2010;18(6):590-605.

53. Liu G, Bollig-Fischer A, Kreike B, et al. Genomic amplification and oncogenic properties of the GASC1 histone demethylase gene in breast cancer. *Oncogene*. 2009;28(50):4491-4500.

54. Li W, Zhao L, Zang W, et al. Histone demethylase JMJD2B is required for tumor cell proliferation and survival and is overexpressed in gastric cancer. *Biochem Biophys Res Commun*. 2011;416(3-4):372-378.

55. Luo W, Chang R, Zhong J, Pandey A, Semenza GL. Histone demethylase JMJD2C is a coactivator for hypoxia-inducible factor 1 that is required for breast cancer progression. *Proc Natl Acad Sci U S A*. 2012;109(49):E3367-76.

56. Black JC, Allen A, Van Rechem C, et al. Conserved antagonism between JMJD2A/KDM4A and HP1gamma during cell cycle progression. *Mol Cell*. 2010;40(5):736-748.

57. Yang J, Jubb AM, Pike L, et al. The histone demethylase JMJD2B is regulated by estrogen receptor alpha and hypoxia, and is a key mediator of estrogen induced growth. *Cancer Res*. 2010;70(16):6456-6466.

58. Cascella B, Mirica LM. Kinetic analysis of iron-dependent histone demethylases: Alpha-ketoglutarate substrate inhibition and potential relevance to the regulation of histone demethylation in cancer cells. *Biochemistry*. 2012;51(44):8699-8701.

59. Rose NR, Woon EC, Kingham GL, et al. Selective inhibitors of the JMJD2 histone demethylases: Combined nondenaturing mass spectrometric screening and crystallographic approaches. *J Med Chem*. 2010;53(4):1810-1818.

60. Thalhammer A, Mecinovic J, Loenarz C, et al. Inhibition of the histone demethylase JMJD2E by 3-substituted pyridine 2,4-dicarboxylates. *Org Biomol Chem*. 2011;9(1):127-135.

61. Chang KH, King ON, Tumber A, et al. Inhibition of histone demethylases by 4-carboxy-2,2'-bipyridyl compounds. *ChemMedChem*. 2011;6(5):759-764.

62. Hamada S, Suzuki T, Mino K, et al. Design, synthesis, enzyme-inhibitory activity, and effect on human cancer cells of a novel series of jumonji domain-containing protein 2 histone demethylase inhibitors. *J Med Chem*. 2010;53(15):5629-5638.

63. Suzuki T, Ozasa H, Itoh Y, et al. Identification of the KDM2/7 histone lysine demethylase subfamily inhibitor and its antiproliferative activity. *J Med Chem*. 2013;56(18):7222-7231.

64. King ON, Li XS, Sakurai M, et al. Quantitative high-throughput screening identifies 8-hydroxyquinolines as cell-active histone demethylase inhibitors. *PLoS One*. 2010;5(11):e15535.

65. Rai G, Kawamura A, Tumber A, et al. Discovery of ML324, a JMJD2 demethylase inhibitor with demonstrated antiviral activity. In: *Probe reports from the NIH molecular libraries program.* Bethesda (MD): ; 2010. NBK169450 [bookaccession].

66. Schiller R, Scozzafava G, Tumber A, et al. A cell-permeable ester derivative of the JmjC histone demethylase inhibitor IOX1. *ChemMedChem*. 2014;9(3):566-571.

67. Kruidenier L, Chung CW, Cheng Z, et al. A selective jumonji H3K27 demethylase inhibitor modulates the proinflammatory macrophage response. *Nature*. 2012;488(7411):404-408.

68. Heinemann B, Nielsen JM, Hudlebusch HR, et al. Inhibition of demethylases by GSK-J1/J4. *Nature*. 2014;514(7520):E1-2.

69. Wang L, Chang J, Varghese D, et al. A small molecule modulates jumonji histone demethylase activity and selectively inhibits cancer growth. *Nat Commun*. 2013;4:2035.

70. Leurs U, Lohse B, Rand KD, et al. Substrate- and cofactor-independent inhibition of histone demethylase KDM4C. *ACS Chem Biol*. 2014;9(9):2131-2138.

71. Woon EC, Tumber A, Kawamura A, et al. Linking of 2-oxoglutarate and substrate binding sites enables potent and highly selective inhibition of JmjC histone demethylases. *Angew Chem Int Ed Engl*. 2012;51(7):1631-1634.

72. Lohse B, Nielsen AL, Kristensen JB, et al. Targeting histone lysine demethylases by truncating the histone 3 tail to obtain selective substrate-based inhibitors. *Angew Chem Int Ed Engl*. 2011;50(39):9100-9103.

73. Luo X, Liu Y, Kubicek S, et al. A selective inhibitor and probe of the cellular functions of jumonji C domain-containing histone demethylases. *J Am Chem Soc*. 2011;133(24):9451-9456.

74. Upadhyay AK, Rotili D, Han JW, et al. An analog of BIX-01294 selectively inhibits a family of histone H3 lysine 9 jumonji demethylases. *J Mol Biol*. 2012;416(3):319-327.

75. Nie Z, Stafford J, Veal J, Wallace M, inventors; Quanticel Pharmaceuticals I, assignee. Histone Demethylase Inhibitors. 2015.

76. Labelle M, Boesen T, Mechtler K, et al, inventors; EpiTherapeutics A, assignee. Inhibitors of Histone Lysine Demethylases. 2014.

77. Labbe RM, Holowatyj A, Yang ZQ. Histone lysine demethylase (KDM) subfamily 4: Structures, functions and therapeutic potential. *Am J Transl Res*. 2013;6(1):1-15.

78. Young LC, Hendzel MJ. The oncogenic potential of jumonji D2 (JMJD2/KDM4) histone demethylase overexpression. *Biochem Cell Biol*. 2013;91(6):369-377.

79. Cloos PA, Christensen J, Agger K, et al. The putative oncogene GASC1 demethylates tri- and dimethylated lysine 9 on histone H3. *Nature*. 2006;442(7100):307-311.

80. Walport LJ, Hopkinson RJ, Schofield CJ. Mechanisms of human histone and nucleic acid demethylases. *Curr Opin Chem Biol*. 2012;16(5-6):525-534.

81. McDonough MA, Loenarz C, Chowdhury R, Clifton IJ, Schofield CJ. Structural studies on human 2-oxoglutarate dependent oxygenases. *Curr Opin Struct Biol*. 2010;20(6):659-672.

82. Rose NR, McDonough MA, King ON, Kawamura A, Schofield CJ. Inhibition of 2-oxoglutarate dependent oxygenases. *Chem Soc Rev*. 2011;40(8):4364-4397.

83. Thinnes CC, England KS, Kawamura A, Chowdhury R, Schofield CJ, Hopkinson RJ. Targeting histone lysine demethylases - progress, challenges, and the future. *Biochim Biophys Acta*. 2014;1839(12):1416-1432.

84. Majamaa K, Hanauske-Abel HM, Gunzler V, Kivirikko KI. The 2-oxoglutarate binding site of prolyl 4-hydroxylase. identification of distinct subsites and evidence for 2-oxoglutarate decarboxylation in a ligand reaction at the enzyme-bound ferrous ion. *Eur J Biochem*. 1984;138(2):239-245.

85. Rose NR, Ng SS, Mecinovic J, et al. Inhibitor scaffolds for 2-oxoglutarate-dependent histone lysine demethylases. *J Med Chem*. 2008;51(22):7053-7056.

86. Murray CW, Blundell TL. Structural biology in fragment-based drug design. *Curr Opin Struct Biol*. 2010;20(4):497-507.

87. Hamada S, Kim TD, Suzuki T, et al. Synthesis and activity of N-oxalylglycine and its derivatives as jumonji C-domain-containing histone lysine demethylase inhibitors. *Bioorg Med Chem Lett*. 2009;19(10):2852-2855.

88. Hann MM, Leach AR, Harper G. Molecular complexity and its impact on the probability of finding leads for drug discovery. *J Chem Inf Comput Sci*. 2001;41(3):856-864.

89. Hann MM, Keseru GM. Finding the sweet spot: The role of nature and nurture in medicinal chemistry. *Nat Rev Drug Discov*. 2012;11(5):355-365.

90. Murray CW, Carr MG, Callaghan O, et al. Fragment-based drug discovery applied to Hsp90. discovery of two lead series with high ligand efficiency. *J Med Chem*. 2010;53(16):5942-5955.

91. Bembenek SD, Tounge BA, Reynolds CH. Ligand efficiency and fragment-based drug discovery. *Drug Discov Today*. 2009;14(5-6):278-283.

92. Lipinski C, Hopkins A. Navigating chemical space for biology and medicine. *Nature*. 2004;432(7019):855-861.

93. Irwin JJ, Sterling T, Mysinger MM, Bolstad ES, Coleman RG. ZINC: A free tool to discover chemistry for biology. *J Chem Inf Model*. 2012;52(7):1757-1768.

94. Meng EC, Shoichet BK, Kuntz ID. Automated docking with grid-based energy evaluation. *Journal of Computational Chemistry*. 1992;13(4):505-524.

95. Gilson MK, Honig B. The inclusion of electrostatic hydration energies in molecular mechanics calculations. *J Comput Aided Mol Des*. 1991;5(1):5-20.

96. Mysinger MM, Shoichet BK. Rapid context-dependent ligand desolvation in molecular docking. *J Chem Inf Model*. 2010;50(9):1561-1573.

97. Irwin JJ, Raushel FM, Shoichet BK. Virtual screening against metalloenzymes for inhibitors and substrates. *Biochemistry*. 2005;44(37):12316-12328.

98. Babaoglu K, Simeonov A, Irwin JJ, et al. Comprehensive mechanistic analysis of hits from high-throughput and docking screens against beta-lactamase. *J Med Chem*. 2008;51(8):2502-2511.

99. Mysinger MM, Weiss DR, Ziarek JJ, et al. Structure-based ligand discovery for the protein-protein interface of chemokine receptor CXCR4. *Proc Natl Acad Sci U S A*. 2012;109(14):5517-5522.

100. Peng Z, Gillespie P, Weisel M, et al. A crowd-based process and tool for HTS hit triage. *Molecular Informatics*. 2013;32(4):337-345.

101. Hubbard RE, Murray JB. Experiences in fragment-based lead discovery. *Methods Enzymol*. 2011;493:509-531.

102. - Hopkinson RJ, - Tumber A, - Yapp C, et al. 5-carboxy-8-hydroxyquinoline is a broad spectrum 2-oxoglutarate oxygenase inhibitor which causes iron translocation. - *Chem Sci*. (- 8):- 3110.

103. Teotico DG, Babaoglu K, Rocklin GJ, Ferreira RS, Giannetti AM, Shoichet BK. Docking for fragment inhibitors of AmpC beta-lactamase. *Proc Natl Acad Sci U S A*. 2009;106(18):7455-7460.

104. Barelier S, Eidam O, Fish I, et al. Increasing chemical space coverage by combining empirical and computational fragment screens. *ACS Chem Biol*. 2014;9(7):1528-1535.

105. Shuker SB, Hajduk PJ, Meadows RP, Fesik SW. Discovering high-affinity ligands for proteins: SAR by NMR. *Science*. 1996;274(5292):1531-1534.

106. Friberg A, Vigil D, Zhao B, et al. Discovery of potent myeloid cell leukemia 1 (mcl-1) inhibitors using fragment-based methods and structure-based design. *J Med Chem*. 2013;56(1):15-30.

107. Villemagne B, Flipo M, Blondiaux N, et al. Ligand efficiency driven design of new inhibitors of mycobacterium tuberculosis transcriptional repressor EthR using fragment growing, merging, and linking approaches. *J Med Chem*. 2014;57(11):4876-4888.

108. Chen Y, Shoichet BK. Molecular docking and ligand specificity in fragment-based inhibitor discovery. *Nat Chem Biol*. 2009;5(5):358-364.

109. Tiefenbrunn T, Forli S, Baksh MM, et al. Small molecule regulation of protein conformation by binding in the flap of HIV protease. *ACS Chem Biol*. 2013;8(6):1223-1231.

110. Nichols DA, Renslo AR, Chen Y. Fragment-based inhibitor discovery against beta-lactamase. *Future Med Chem*. 2014;6(4):413-427.

111. England K, Tumber A, Krojer T, et al. Optimisation of a triazolopyridine based histone demethylase inhibitor yields a potent and selective KDM2A (FBXL11) inhibitor. *MedChemComm*. 2014;5:1879.

112. Duan D, Doak AK, Nedyalkova L, Shoichet BK. Colloidal aggregation and the in vitro activity of traditional chinese medicines. *ACS Chem Biol*. 2015;10(4):978-988.

113. Copeland R. *Enzymes: A practical introduction to structure, mechanism and data analysis.* 2nd ed. New York: Wiley; 2000.

114. Nakayama J, Rice JC, Strahl BD, Allis CD, Grewal SI. Role of histone H3 lysine 9 methylation in epigenetic control of heterochromatin assembly. *Science*. 2001;292(5514):110-113.

115. Lennox AJ, Lloyd-Jones GC. Selection of boron reagents for suzuki-miyaura coupling. *Chem Soc Rev*. 2014;43(1):412-443.

116. Dick GR, Woerly EM, Burke MD. A general solution for the 2-pyridyl problem. *Angew Chem Int Ed Engl*. 2012;51(11):2667-2672.

117. Kupershmit I, Khoury-Haddad H, Awwad SW, Guttmann-Raviv N, Ayoub N. KDM4C (GASC1) lysine demethylase is associated with mitotic chromatin and regulates chromosome segregation during mitosis. *Nucleic Acids Res*. 2014;42(10):6168-6182.

118. O'Gorman S, Fox DT, Wahl GM. Recombinase-mediated gene activation and site-specific integration in mammalian cells. *Science*. 1991;251(4999):1351-1355.

119. Livak KJ, Schmittgen TD. Analysis of relative gene expression data using real-time quantitative PCR and the 2−ΔΔCT method. *Methods*. 2001;25(4):402-408.

Publishing Agreement

It is the policy of the University to encourage the distribution of all theses, dissertations, and manuscripts. Copies of all UCSF theses, dissertations, and manuscripts will be routed to the library via the Graduate Division. The library will make all theses, dissertations, and manuscripts accessible to the public and will preserve these to the best of their abilities, in perpetuity.

Please sign the following statement:

I hereby grant permission to the Graduate Division of the University of California, San Francisco to release copies of my thesis, dissertation, or manuscript to the Campus Library to provide access and preservation, in whole or in part, in perpetuity.

Author Signature

6/16/15

Date